Characterization and modeling of the dynamic electrochemical-thermal mechanics of Li-ion batteries

by
Ki Yong Oh

A dissertation submitted in partial fulfillment
of the requirements for the degree of
Doctor of Philosophy
(Mechanical Engineering)
in the University of Michigan
2016

Doctoral Committee:
Professor Bogdan I. Epureanu, Chair
Professor Krishnakumar R. Garikipati
Professor Nickolas Vlahopoulos
Professor Kon-Well Wang

To my family

ACKNOWLEDGEMENTS

First, I wish to express my utmost gratitude to my advisors and chair of my doctoral committee, Professor Bogdan I. Epureanu, for his inspiring and encouraging guidance during the past years. I also want to thank Professor Krishna Garikipati, Professor Nickolas Vlahopoulos, and Professor Kon-Well Wang for their valuable comments and suggestions, and serving on my doctoral committee. I sincerely admit that it may not be possible to attain without their supervision and supports.

I am also grateful to my colleagues of Applied Nonlinear Dynamics of Multi-Scale Systems Laboratory, including Kiran D'Souza, Andrew Sloboda, Sungkwon Hong, Olguta Marinescu, Woochul Nam, Seunghoon Baek, Eleni Gourgou, Ehsan Mizakhalili, Amin Ghadami, Jauching Lu, Mainak Mitra, and Weihan Tang, for their insights and suggestions. It has been a very nice time and a good memory for me.

I would like to express my appreciation for my entire family, in particular my parents and in-laws for their love and supports. I am also thankful to my sons Jitae and Jihoo for being so adorable and healthy. Finally, I appreciate my lovely wife, Kyoungsun, for marrying me and for her unwavering support. Her encouragement enabled me to complete this work. I would like to give my thanks and apologies to all those who helped me but not mentioned here.

I am thankful for the financial support over the course of my PhD studies. My study was funded in part by the Advanced Research Projects Agency-Energy (ARPA-E), U.S. Department of Energy, under Award Number DEeAR0000269.

TABLE OF CONTENTS

LIST OF FIGURES

LIST OF TABLES

ABSTRACT

Characterization and modeling of the dynamic electrochemical-thermal mechanics of Li-ion batteries

by

Ki-Yong Oh

Chair: Bogdan I. Epureanu

The reliability and lifetime of Li-ion cells can be improved by understanding their operational wear. In this work, an experimental characterization of Li-ion cells is carried out, and novel phenomenological models are developed to elucidate the dynamic electrochemical-thermal mechanics of Li-ion cells.

Two sources of swelling and reaction force, namely Li-ion intercalation and temperature variations, are identified through experiments. The swelling and force from temperature variation and the state of charge (SOC) shows nonlinear characteristics. To account for these behaviors, the model must include a coefficient of thermal expansion and stiffness at the cell-level, which depend on temperature and the SOC.

Based on the experimental characterization, a 1-D phenomenological multi-physics model is proposed to predict the complex dynamic behavior of Li-ion cells. The model consists of an electro-thermal model, a swelling model, and a force model. The electro-thermal model estimates the SOC and the surface/core temperature with current and ambient temperature profiles. The swelling model predicts the volume change of a cell due to Li-ion intercalation and temperature variation as a function of the SOC and surface/core/ambient temperature. The force model incorporates nonlinear elastic stiffness and separates the overall SOC region into three regions to account for Li-ion intercalation and phase transitions. The force model

estimates the reaction force caused by the battery swelling and the preload as a function of the estimated SOC and total swelling. Experimental validation demonstrates that the proposed multi-physics model accurately predicts complex physics behind cells at the wide range of preload and ambient temperature.

A 3-D numerical and phenomenological cell model is developed also to predict strain and stress distribution on the surface of cells. To model the inherently different microphysical swelling processes from Li-ion intercalation and thermal expansion, the model incorporates the nonlinear equivalent modulus of elasticity and the equivalent coefficient of thermal expansion, which are functions of the SOC. Comparison between experiments and model predictions clearly demonstrates that this 3-D model accurately reproduce the swelling shape, suggesting that the model can be useful for cell design, developing new strain/pressure sensors, and optimizing sensor locations.

CHAPTER I
Introduction

Recent concerns regarding carbon dioxide emissions and rising energy demands determined automobile industries to concentrate on developing eco-friendly, high-efficiency vehicles. Electrified vehicles address these challenges. However, they require energy storage systems featuring a high gravimetric/volumetric energy and power density for reversible power sources. Moreover, the drive toward renewable energy has enhanced the development and construction of wind and solar farms worldwide. Such renewable energy outputs depend on weather conditions, which make their availability stochastic. Energy storage systems are one of the promising solutions for mitigating the effects of intermittent renewable resources on networks, allowing increased renewable energy utilization, and providing flexibility and ancillary services. In summary, the market demands for developing rechargeable batteries with high power and energy density as well as long cycle life have significantly increased in many application fields.

Li-ion batteries (LIBs) are free from several deficiencies of other batteries, such as high self-discharge rate and memory effects [26-28]. This enables LIBs to occupy a dominant position in the portable electronics and energy storage system markets. Moreover, these innate advantages not only make LIBs promising power sources for current and next generation electric powered vehicles but also make LIBs applicable to back-up applications in the military, healthcare, and telecommunications industries. Indeed, LIBs are highly versatile energy storage devices for a variety of applications from small-scale portable electronics to large-scale energy storage systems and electrified vehicles.

One of the major concerns that limit the application of LIBs is the safety and reliability of battery cells. Failures of LIBs not only result in serious inconvenience and enormous replacement/repair costs, but also risk catastrophic consequences such as explosions due to overheating and short circuiting. To prevent severe failures and optimize proactive

maintenance/replacement of LIBs, breakthroughs in diagnosis, prognosis, and health monitoring of LIBs should be achieved with an accurate model and novel battery management strategies.

Multiple phenomena occur concurrently in LIBs during charge/discharge process. The flow of electrons is proportional to current and driven by difference in electrochemical potential between the electrodes. This charge process also transfers Li-ions between electrodes, meaning that the amount of Li-ion in each electrode varied upon the charge state. This phenomenon is called Li-ion intercalation/deintercalation. Interestingly, Li-ion intercalation/deintercalation changes the volume of positive and negative electrodes due to microstructure transformation and thereby creates internal stress. The high-rate charge and discharge generate a large amount of heat due to mainly the resistivity of the materials consisting of electrodes, separator, and current collectors. This heat increases the temperature of battery cells and thereby creates thermal stress and strain. In other words, the variations of temperature and the microstructure transformation of electrodes during electrochemical reaction generate the electrochemical- and thermal-induced stress and strain.

Significant efforts have been devoted to understanding the volume change (swelling) of electrode materials [6-8] and cells [4,5] from Li-in intercalation. These studied suggested that the swelling of graphite anode materials is significant over 10% of their thickness [17], whereas that of nickel/manganese/cobalt-oxide positive electrodes is small less than 1% of their thickness [19], which are main materials of LIBs nowadays. The large swelling in the anodes creates large periodic stresses of cells, suggesting that this periodic stresses accumulated during cycling lead to performance degradation, capacity loss, and eventual failure. Because of the importance of this periodic stresses, research into the stresses generated within active materials and the porous electrodes that support them has been carried out [9-11]. The dependency of capacity fade on initial stack pressure has also been examined [12].

Numerical simulations with computational fluid dynamics (CFD) methods and finite element methods (FEM) have also been conducted to predict thermodynamics of Li-ion battery cells and packs [2,31,85,100]. A variety of heat transfer models have been created and validated through experiments [32]-[35]. Several lumped parametric thermal models have also been proposed for the control purposes with the advanced power management schemes in next-generation battery management systems (BMS) [43,44,62]. In addition, several studies have

been carried out to characterize the thermal expansion of the host materials in micro-scale [39-41].

These studies promote theoretical and experimental understanding of the structural response of the LIBS associated with the electrochemical- and thermal-induced stress and strain. However, there are several limitations in previous studies.

First, modeling efforts for Li-ion intercalation-induced stress and strain on the cell-level is still few, whereas the micro swelling of electrode materials in LIBs under charge process has been intensively investigated [4-11]. Moreover, no attempt has been conducted to use this phenomenon to enhance the state of charge (SOC) and the state of health (SOH) estimation with other information including measured current and voltage.

Second, quantifying thermal swelling and related properties on the cell-level is still few. Therefore, it is hard to estimate thermal stress and strain and their effects on the lifetime and fatigue of cells. Note that previous research has been focused on the estimation of temperature distribution over battery cells including the estimation of core temperature. Especially, the most important property which comes from both the material and its structure inside the cell, i.e. the equivalent coefficient of thermal expansion on the cell-level, was never reported before, even though this property is crucial not only to predict the dynamic thermal mechanics of battery cells but also to estimate periodic thermal stress/strain on packs.

Third, the modeling of the thermal expansion on the cell-level with the measured material properties has not been investigated in great detail, although this model might be beneficial to prolong the life of LIBs. The limited information about thermal stress and strain on the cell-level stimulates the quantification of thermal stress and strain on the battery cells and packs, which affect the battery performance in packs.

Forth, the swelling shape on the surface of battery cells due to two different origins has not been investigated before. Therefore, the effects of swelling from Li-ion intercalation and temperature variation on cells and packs are still unclear. Note that the swelling on the cell-level is more complicated because of the hundreds of contact surfaces between electrodes and mechanical constraints such as wounding shape of the jellyroll and clamping current collectors with bus bars in the edge sides. The effect of mechanical constraints and reaction force created in pack conditions are also hard to estimate without modeling efforts.

Fifth and finally, there is no fully coupled multi-physics model of the LIBs. The multi-physics models proposed in previous studies couple the model between electrochemistry and

heat transfer and thereby predict electric and temperature responses [85,116-118]. These models are difficult to predict the dynamic electrochemical-thermal mechanics and these effects on cells and packs. Therefore, the available information from existed multi-physics models limits the use of these models on the SOC and SOH estimation in pack conditions.

To address these challenges, the experimental characterization of LIBs and the development of accurate phenomenological models should concurrently be carried out. The importance of the dynamic electrochemical-thermal mechanics of LIBs leads to the research herein focusing on not only the characterization of swelling and force induced from electrochemical reaction and temperature variations, but also the development of novel models for advanced battery health monitoring and management.

Two kinds of experiments are mainly carried out to elucidate the electrochemical-thermal mechanics of LIBs. The swelling and force of a commercial 5Ah Li-ion cell with a nickel/manganese/cobalt-oxide cathode are investigated at a variety of operational conditions. In combination with sensitive displacement and force measurements, knowledge of the electrode configuration within this prismatic cell's interior allows macroscopic deformations of the casing to be correlated to electrochemical and mechanical transformations in individual anode/separator/cathode layers. The quantitative swelling and force from two different sources, i.e. Li-ion intercalation and temperature variations, is characterized. Thermal expansion and interior charge state are both found to cause significant swelling and force, which feature nonlinear characteristics. Moreover, important material properties, which are essential to model LIBs, such as the equivalent coefficient of thermal expansion and the equivalent stiffness over SOC are identified.

Based on the characterization of LIBs, a novel phenomenological multi-physics model is developed for control and SOC/SOH estimation purposes. The model accounts for electrical, thermal, and mechanical behaviors of LIBs under a constrained condition, e.g., a battery pack condition. Specifically, the proposed model predicts the core and surface temperatures and reaction force induced from the volume change of battery cells because of electrochemically- and thermally-induced swelling. Moreover, the model includes the influences of changes in preload and ambient temperature on the force. Intensive experimental validation demonstrates that the proposed multi-physics model accurately predicts the surface temperature and reaction force at the wide operational range of preload and ambient temperature.

A 3-D numerical and phenomenological cell model is also developed to predict strain and stress distribution on the surface of cells at free condition and pack conditions. The thermal swelling shape is different to that of Li-ion intercalation. Whereas the swelling shape due to Li-ion intercalation looks like rectangular shape similar to the case and the center region is almost flat, the swelling due to elevated temperature looks like convex and circular shape, motivating to develop the 3-D model capable of these features. The 3-D model incorporates the equivalent modulus of elasticity and the equivalent coefficient of thermal expansion, which are functions of the SOC, and also includes the proper boundary conditions to replicate conditions experienced in battery cells and packs. Moreover, internal heat generation of the jellyroll is calculated from an electro-thermal model and use as input for the prediction of thermal swelling. Experimental validation confirms that this 3-D model accurately reproduce the swelling shape at overall SOC regions and a variety of C-rates.

The remaining chapters of this dissertation are compiled from a collection of five manuscripts submitted to archival journals. Because of this, some of the background material is repeated in several chapters.

CHAPTER II

Rate Dependence of Swelling in Lithium-ion Cells

2.1 Motivation and background

Automobile manufactures have recently accelerated battery development efforts to meet stringent fuel economy and emission standards for future hybrid electric vehicles (HEVs) and electric vehicles (EVs), with most research focused on the design of lithium-ion (Li-ion) battery packs [1,2]. Cycle life is a particular concern because of the high cost of the battery pack relative to that of the total vehicle. The mechanical response of battery cells during cycling impacts cycle life since fatigue may lead to capacity loss and eventual failure [3]. To date little is understood about the effects of stress and strain on cell-level performance, because data evaluating coupled electrochemical and mechanical phenomena is sparse. However, it becomes more and more significant to understand the stress and strain characteristics of Li-ion battery cells. This understanding would help develop strategies to reduce cell-level volume changes, which could ideally prolong cycle life by reducing the tendencies of cell materials to mechanically degrade.

Many efforts have been devoted to measuring periodic swelling of electrode materials in Li-ion batteries under charge and discharge conditions [4-8]. As a consequence of swelling, large periodic stresses – potential internal fatigue loads – can be experienced by cells stacked and constrained in a battery pack. The data presented here shows that the volume change of Li-ion battery cells is far from insignificant. Large periodic loads and dynamic expansion should be taken into consideration during battery pack modeling and design.

Information is available about mechanical effects from a microscopic perspective. Research into the stresses generated within active materials and the porous electrodes that support them has been carried out [9-11]. The dependency of capacity fade on initial stack pressure has also been examined [12]. These studies provide a useful foundation for understanding the physical phenomena within active materials associated with Li-ion intercalation and deintercalation. But the relationships among mechanical forces remain poorly understood, making it difficult to predict how overall expansion or contraction of the electrode sandwich arises from stresses and strains within its constituent elements. Moreover, the behavior of active materials during high-rate operation, where local joule heating and changes in charge state may both cause deformation, has not been investigated in great detail.

A high-precision displacement sensor was used to quantify the volume changes arising from Li-ion intercalation in an unconstrained graphite/nickel-manganese-cobalt-oxide (NMC) battery cell, whose temperature was regulated in a thermal chamber. Swelling of the cell was studied as a function of the state-of-charge (SOC) and the charge/discharge rate (C-rate). The extent of swelling was found to vary significantly with both experimental control parameters. When the rate was sufficiently low to main a relatively constant cell temperature, swelling in the fully charged state was generally as high as 1.5% relative to a cell equilibrated at 0% SOC. By examining the derivative of swelling with respect to capacity, different phase transitions within the electrode materials can be identified. These correlate to the sudden changes in open-circuit potential that occur with the phase changes in electrode materials [13].

The extent of swelling was also found to exhibit strong rate dependence, despite the fact that cell potential vs SOC did not change significantly over the range of C-rates investigated. Thus information about swelling may provide a more sensitive gauge of a battery cell's dynamic state than its voltage.

2.2 Experimental

A flat-wound type prismatic (120mm×85mm×13.5mm width×height×depth) 5Ah Li-ion battery cell was obtained from a Ford Fusion HEV battery pack. Dissection of a similar cell from the same pack showed that the cell interior contains a single flat-wound electrode

jellyroll that fits snugly within the battery casing; thus, through the depth dimension *z*, the cell interior comprises 52 stacked, essentially planar sandwich layers, each of which lies predominantly in the *x*-*y* plane labeled in Figure 1.

The cell casing, the thickness of the positive electrode plate, the negative electrode plate were measured with calipers (650µm, 80µm, 80µm respectively). The separator is 25µm in general [14]. Thus, each anode/separator/cathode layer (consisting of 1 positive/negative electrode plate and 2 separators) has a thickness of 210µm and the estimated total thickness of the jellyroll is 11.0mm considering the number of stacks (52). The estimated total thickness of the jellyroll corresponds well with the measured depth of the casing (12.2mm) considering additional insulation materials, which is formed on the outer circumference of a jellyroll to secure electrical insulation between the jellyroll and the cell casing.

When unrolled, the sandwich consists of an aluminum positive current collector coated on both sides with the lithium nickel/manganese/cobalt oxide (NMC) material, a microporous polyethylene separator material, and a copper negative current collector coated on both sides with a graphite intercalation material (Li_xC_6) [16].

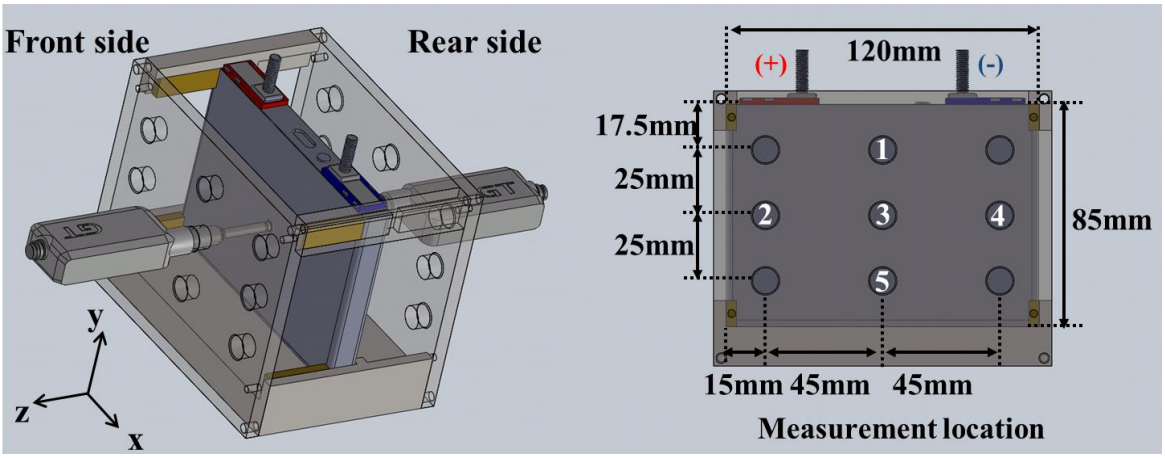

Figure 1. Schematic diagram of the experimental setup showing the fixture, the cell, and the sensor locations 1-5

High-precision contact-type displacement sensors with 1µm accuracy and 0.1µm resolution (Keyence GT2-H12KL, Japan) were used for displacement measurements. A low-stress type head with contact force of under 0.3N was used to minimize the contact force exerted on the battery's surface by the sensor head.

A fixture was made from ABS plastic using a rapid-prototyping machine (Dimension Elite FDM, USA). In the fixture, the prismatic battery cell was constrained at its eight corners with

ABS plastic set-screws, but was otherwise unconstrained for free swelling condition. The fixture was designed to minimize the contact area between the set-screws and the battery, which was less than 0.4cm^2 total. Note also that the modulus of elasticity for the fixture material (ABS plastic) is 2.2GPa, which is more than 30 times smaller than that for aluminum (68GPa). Thus, the limitations that the fixture placed on the free swelling of the cell were determined to be negligible.

The fixture was placed inside a thermal chamber (ESPEC BTZ-133, Japan) that maintained a constant ambient temperature of 25.5℃ for all tests. Three thermocouples were also placed on the cell exterior to measure surface temperatures in two locations, as well as the near-surface air temperature. One thermocouple was installed on the center of the battery cell (in a location that avoided interference with a displacement sensor). Another thermocouple was installed on the top of the battery between the positive and the negative terminals. The third thermocouple was installed between the fixture and the battery cell to measure near-surface ambient temperature.

The Li-ion intercalation/deintercalation into the electrode occurs mainly in a direction perpendicular to the electrodes during charge and discharge. Therefore, swelling in the z direction, which is perpendicular to the electrodes (as reported in reference [16], and also verified by dissection of a cell in an Ar glovebox). The configuration of sensors within the fixture is shown in Figure 1. Note that it was observed that no gap existed between the flat-wound jellyroll and the casing in the z direction. In contrast, there were observed to be gaps between the casing and the jellyroll on the sides and the top of the cell. Hence, swelling in the transverse directions was determined to be negligible and was not measured.

In a first experiment the relative expansion in the z direction was measured at five locations labeled 1–5 in Figure 1, to assess the uniformity of the swelling distribution in the plane of the multi-layer electrode sandwich. For each experiment the battery was charged using a standard constant-current, constant-voltage charging profile at 2A; the voltage was clamped after reaching 4.1V, at which it was held until the current tapered to C/100 (50mA). The battery then was allowed to rest at open circuit for 3 hours to ensure thermal equilibrium prior to discharging. This experiment was performed using a 0.4C discharge rate to mitigate the effects of swelling due to thermal expansion.

In a second experiment, opposing displacement sensors were placed at the geometric centers on both faces of the cell normal to *z* (location 3 shown in Figure 1). The net displacement

was measured with respect to the charge state during discharge at a variety of C-rates using a standard constant-current, constant-voltage charging/discharging profile. All discharges were performed at fixed C-rate down to 0% SOC. Measurements with exterior thermocouples showed that the lowest current used, 0.4C (2A), did not cause significant heating; this was confirmed by the observation that the battery-cell surface remained within 0.5℃ of the 25.5℃ ambient temperature throughout the discharge process. Data at 0.4C therefore allow direct correlations to be made between swelling and Li-ion intercalation in a cell sandwich, without significant convolution with thermal expansion. In contrast, the cell surface temperature deviated more significantly from the ambient at higher rates – as much as 3℃ higher in the 5.0C case.

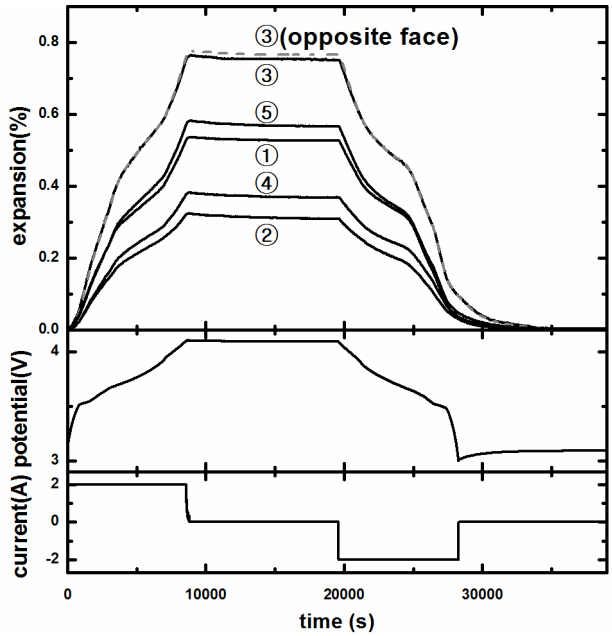

Figure 2.Expansion (swelling) trends over time; encircled digits indicate measurement points shown in Figure 1; the current and measured potential over time are shown in the bottom plots.

2.3 Results and discussion

Figure 2 illustrates the expansion measured at five locations on the front surface, and at the center location on the rear surface, during a 0.4C charge/discharge. The geometric centers on the *xy* surfaces of the battery travel outward by 99.8μm and 103.2μm, respectively after charge; both return to their original positions at the end of discharge. Given that the thickness of the discharged battery is 13.5mm, the total normal strain in the *z* direction in the center of

the cell amounts to 1.5%. It can be inferred that swelling of active materials is translated into swelling of the case. On an average basis, the dilation of each anode/separator/cathode layer would also be expected to match this 1.5%. Because the amount of swelling is not small, expansion should be considered in the design of the battery pack to improve the reliability and predict the lifespan as periodic stress is generated, not only within the electrode sandwich or a single cell, but also within the battery pack.

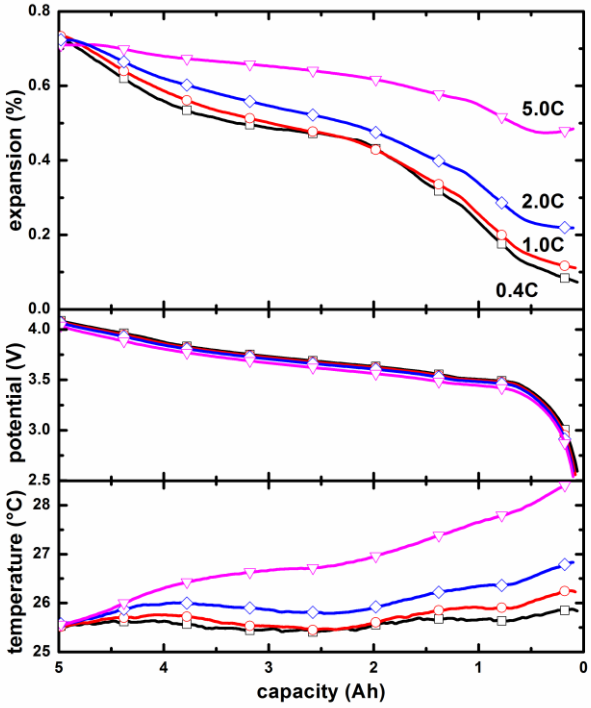

Figure 3.Expansion, potential, and surface temperature versus capacity for discharge at a variety of C-rates on the center of the surface of the battery (location 3 in Figure 1)

In general, graphite anode materials exhibit 10% volume expansion under charge [17], and irrecoverable volume increase at a graphite intercalation material due to solid-electrolyte interphase formation is at least 4% of initial thickness [18]. Therefore 6% of reversible swelling from a graphite intercalation material is able to be translated into 2% expansion of total thickness, in that the negative-electrode volume occupies about 29% of the jellyroll volume (taking the thickness of Cu foil to be 10μm [16]). In contrast, the volume contraction from a nickel/manganese/cobalt-oxide positive electrode is less than 1% [19]. So 1% of contraction from the cathode material can be translated into ~0.5% contraction of the total thickness, as the cathode volume also occupies about 29% of the jellyroll. In consideration of the volume expansion of the negative electrode and the volume contraction of the positive electrode, total variation of the volume is 1.5%, which is well matched with experimental

result. It is also found that the overall shape of the measured swelling is similar to the average interlayer spacing of graphite within the negative electrode [20]. These results corroborate the hypothesis that the SOC-dependent exterior volume change can be mainly attributed to changes within the negative electrode.

As expected, displacements in the geometric centers of the battery faces are the largest; displacements reduce near the edges of the cell because of mechanical constraints imposed by the battery casing. The smallest expansion was measured at locations 2 and 4. Note also that dissection of the cell showed that the current collectors flank the flat-wound jellyroll on its left and right edges (approximately beneath the positive and negative exterior terminals) [16]; since they undergo no chemical transformation they would not be expected to dilate with changing SOC at fixed temperature. Hence, the empty space along the left and right edges of the current collectors (where no internal force due to the lithium-ion intercalation is exerted on the casing) leads to the smallest expansion observed at locations 2 and 4. Moreover, the relatively large thickness of the casing and the higher modulus of elasticity of the aluminum casing (much larger than that of the electrode and the separator) might result in location dependency of the swelling [15,21].

Most significantly, the cell was found to expand asymmetrically, with a statistically significant difference upon completion of charging. The bottom (location 5) swells more than the top (location 1); the swelling of the top and the bottom side are 72.4μm and 78.8μm respectively. This is due to the different thickness of the top and the bottom of the casing; the thicknesses of the top and the bottom are 1,500μm and 650μm respectively. Thus, the stiffness of the top of the casing is much higher than that of the bottom, and hence the bottom side of the casing is easier to deform than the top. It might also result in the empty space between the top of the case and the jellyroll because no internal force due to the lithium-ion intercalation is exerted on the empty space of the casing. The asymmetry between left/right sides can be due to differing material properties and complex shapes of both current collectors and clamps, which fix different positions of the jellyroll at each current collector.

The surface temperature of the battery remains within a range smaller than 0.5℃ during charge and discharge at the rate of 0.4C. Thus, the effects of thermal gradients on the swelling shape of the battery in the *x-y* plane are likely negligible at 0.4C. In contrast, these thermal gradients may affect the shape of the swelling of the cell in the *x-y* plane at high C-rates because the internal heating of the electrodes creates a thermal gradient.

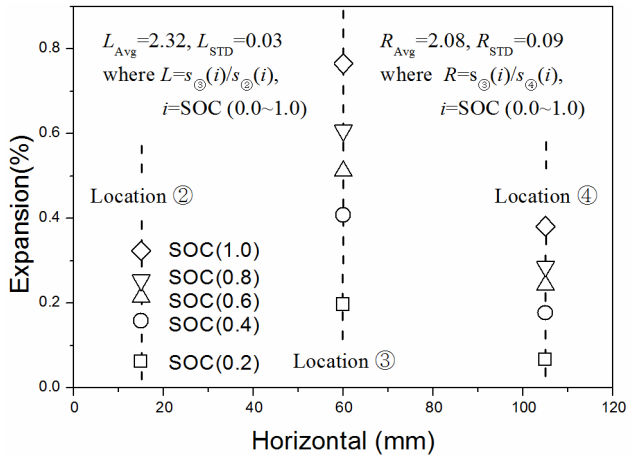

(a) Horizontal expansion (swelling) shape at various SOC; the horizontal axis is the coordinate along axis *x* shown in Figure 1

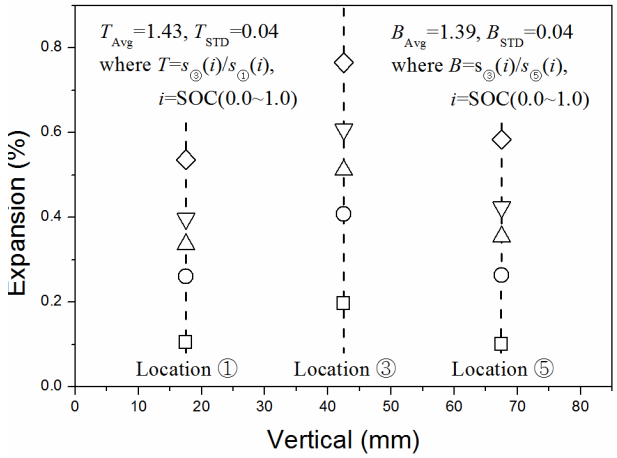

(b) Vertical expansion (swelling) shape at various SOC; the horizontal axis is the coordinate along axis *y* shown in Figure 1

Figure 4.The spatial distribution of swelling; subscripts Avg and Std indicate average values and standard deviation levels; each dashed line indicates a measurement location

The overall strain distribution appears to remain the same during charging and discharging. Figure 4 (a) and (b) illustrate the variation of expansion with respect to SOC. The ratio of expansion between center and other locations (L_{Avg} , R_{Avg} , T_{Avg} , B_{Avg}) is constant throughout the range of SOC. This could suggest that the reaction distribution throughout the jellyroll is relatively constant. Regardless, the constant shape of the surface-strain distribution suggests that a single point measurement can be used to accurately quantify the entire cell swelling at the C-rates studied.

Figure 5 shows the swelling, cell potential, and measured surface temperature at the center of the battery case surface during discharges at a variety of C-rates.

The residual swelling at end-of-discharge was found to depend strongly on discharge rate, despite the fact that cell potentials did not change significantly. Although the amount of

charge processed at all C-rates was nearly identical, at higher rates the battery had not returned to its initial thickness when the voltage reached 2.5V. The higher C-rate operation leads to the larger temperature increase, as shown at the bottom of Figure 5. The total thermal swelling of the cell results from thermal swelling of each cell component. However, it is hard to estimate the thermal swelling of each cell component based on measured cell-level thermal swelling. When a jellyroll is fabricated, positive/negative electrodes are wound and the resulting jellyroll is clamped and welded to the buss bars at each side [16]. This manufacturing process results in pre-stress and possibly plastic deformation of layers inside the jellyroll. Thus, to estimate the impact of each component on the thermal swelling, the pre-stress and the modulus of elasticity of each component should be characterized also. However, the estimation of the pre-stress in the jellyroll is difficult without exact information regarding the manufacturing process. Moreover, the modulus of elasticity of each component was not available. Hence, the contribution of each cell component is hard to estimate given only cell-level thermal expansion data. However, equivalent mechanical properties of the cell (such as equivalent modulus of elasticity and equivalent coefficient of thermal expansion) can be used to create accurate battery swelling models for efficient control and health management.

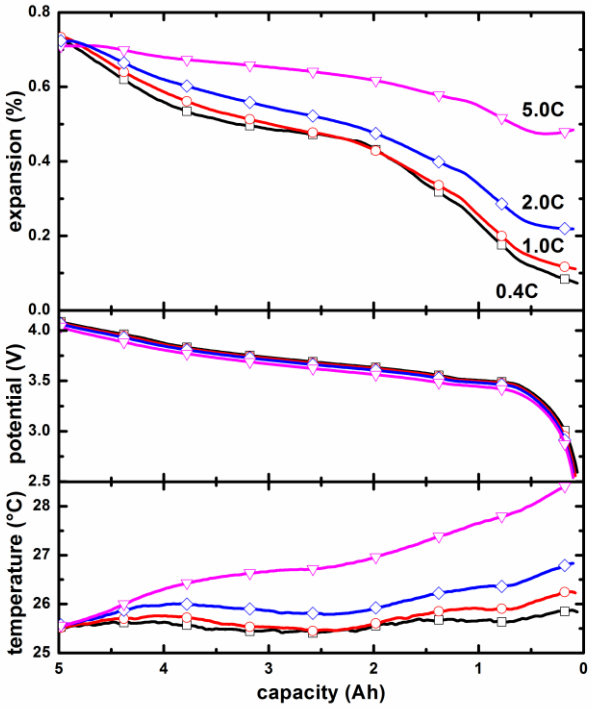

Figure 5.Expansion, potential, and surface temperature versus capacity for discharge at a variety of C-rates on the center of the surface of the battery (location 3 in Figure 1)

Figure 6 illustrates the response during the open-circuit rest period after discharge, during which the swelling continued to decrease and finally returned its initial value. The measured data reveal a relaxation with two time constants in the swelling, namely

$$s = a_0 + a_1 e^{-t/\tau_1} + a_2 e^{-t/\tau_2}, \quad (1)$$

where s is the swelling measured at location 3 (Figure 1). The coefficients a_0, a_1, and a_2, and the time constants τ_1 and τ_2 are obtained by curve fitting the measured relaxation data. The faster response can be attributed to thermal relaxation, because its time constant is consistent with the one extracted from measured surface temperature, shown in the lower subplot of Figure 5. The slower response may be caused by visco-elastic mechanical relaxation. A small increase of swelling is observed at the beginning of the relaxation period for 5C discharge, which correlates with the continued rise in surface temperature following the cessation of the current.

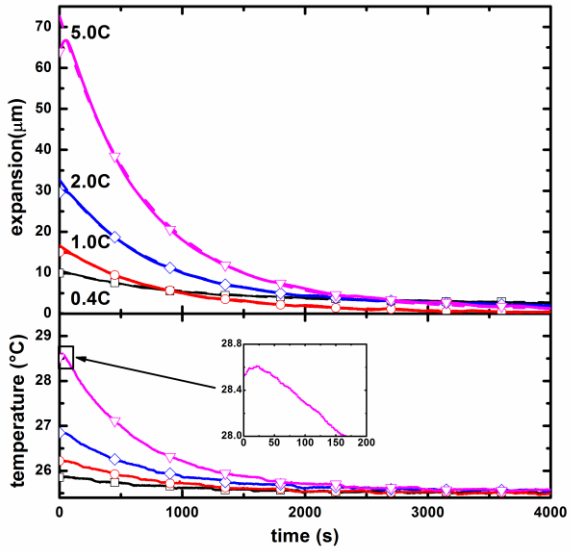

Figure 6.Relaxation and surface temperature at the end of the discharge at a variety of C-rates on the center of the surface of the battery (location 3 in Figure 1)

These experiments were carried out in the thermal chamber, which regulates ambient temperature to 25.5℃. The temperature of the cell converges to ambient temperature, as shown in the bottom of Figure 6. The temperature was continuously controlled during charge and discharge. Thus, the internal heat (e.g., produced from joule heat and entropy heat) is removed from the chamber during operation, and so the ambient temperature does not increase. Hence, the thermal swelling (at constant ambient temperature) is smaller than the

thermal swelling in an insulated/adiabatic environment (where the temperature increases). In conclusion, the thermal swelling depends on the C-rate and the heat dissipation rate. Also, the heat dissipation from the cells is important for the design of battery packs (to mitigate the thermal swelling and thermal stress).

The role of individual electrodes in the overall swelling process can be understood by analyzing the derivative of swelling s with respect to capacity Q, namely $\mathrm{d}s/\mathrm{d}Q$. The swelling derivative is compared with the derivative of potential with respect to capacity, $\mathrm{d}V/\mathrm{d}Q$, in Figure 7. The lines denote $\mathrm{d}s/\mathrm{d}Q$ curves and the dot lines denote $\mathrm{d}V/\mathrm{d}Q$ curves in Figure 7. Most of the local maxima of $\mathrm{d}V/\mathrm{d}Q$ correspond to phase transitions known to occur in graphite negative electrodes; the voltages at which these maxima occur are similar to previously reported results [13,22]. Phase transitions of the positive NMC electrode do not appear to have strong signatures, because the NMC structure does not fill in stages the way the graphite lattice does, and undergoes smaller volume changes [8,23]. Therefore the macroscopic swelling at low rates appears to be dominated by the negative electrode, which corresponds well with calculated volume change of the positive and negative electrode.

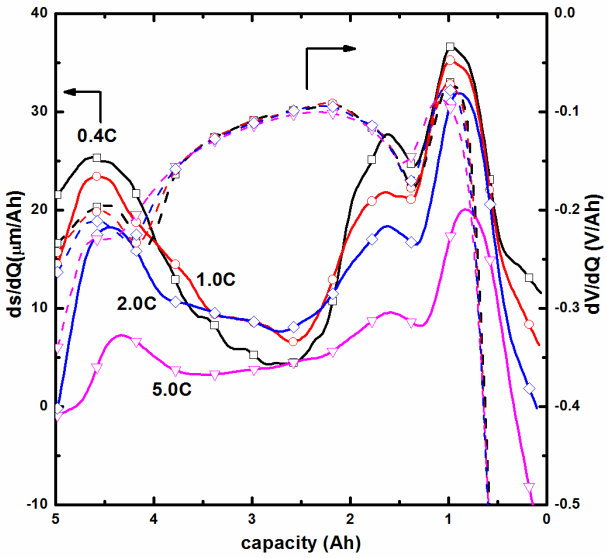

Figure 7. $\mathrm{d}s/\mathrm{d}Q$ and $\mathrm{d}V/\mathrm{d}Q$ at a variety of C-rates on the center of the surface of the battery for discharge (location 3 in Figure 1).

The peak locations for $\mathrm{d}s/\mathrm{d}Q$ and $\mathrm{d}V/\mathrm{d}Q$ differ slightly at different C-rates, suggesting that higher discharge rates correlate with later signatures of phase transition. This could owe to the fact that multiple co-existing phases exist in the negative electrode, which may be present to different extents when the surface overpotential in the electrode is higher [24]. The peak

shift may also owe to lagging thermal expansion, as shown during the relaxations at 5C in Figure 7. It is also possible that the lag owes to delay of structural change due to slow diffusion of Li-ion [25] or a viscoelastic effect, whereby the stresses induced by lithium intercalation/deintercalation take some time to manifest as macroscopic strain. The ds/dQ might be applicable for fault diagnosis, prognosis and estimation of aging of the battery cell in that the swelling of the battery cell is sensitive factors affecting cell performance.

2.4 Conclusions

The surface swelling of a 5Ah Li-ion battery cell with a NMC cathode was studied at various C-rates. Significant strain was measured at the geometric center of the battery case: the anode/separator/cathode layers appear to dilate in thickness by 1.5% as the cell is taken from 0% to 100% SOC. The contraction observed on discharge was found to depend strongly on the C-rate, although the potential varied minimally. Thermal and mechanical relaxations appeared to contribute to the strain response at high discharge rates. Signatures of phase transitions in the negative electrode could be identified by analyzing strain as a function of capacity; this response was also found to depend strongly on the C-rate. The overall distribution of strain across the battery surface retained the same shape regardless of SOC, suggesting that the current distribution within the electrode jellyroll is relatively uniform.

CHAPTER III

A Novel Thermal Swelling Model for a Rechargeable Lithium-ion Battery Cell

3.1. Motivation and background

Concerns for energy security, instability in world oil markets, and limitations of carbon emissions have accelerated the development of eco-friendly, high-efficiency automobiles. This drives automobile industries toward the development of vehicle electrification technology. Electrified vehicles currently use lithium-ion (Li-ion) batteries as the reversible power source. Li-ion batteries have advantages such as high power/energy density, high potential, and low self-discharge rate. They are also environmentally friendly and have a long life cycle [26-28].

While vehicle electrification with the advent of the Li-ion batteries [29] enhances fuel efficiency and reduces CO_2 emissions, many challenges still exist when using Li-ion batteries such as their limited performance at low temperatures [30] and their thermal runaway [1]. Especially, extensive research on vehicle electrification has been driven by stringent safety standards for air and ground applications. Therefore, recent research focuses on the thermal distribution and the heat dissipation of Li-ion battery packs [2,31] as elevated temperatures not only can cause thermal runaway but can also degrade battery life. A variety of heat transfer models have been created for the Li-ion batteries and validated through experiments [32-35]. Many methods and strategies for use in battery management systems (BMS) have been developed to mitigate the safety concerns while enhancing efficiency and capabilities [36,37,43].

Heat is generated in a Li-ion battery cell from two sources: entropy change and Joule heat.

Entropy compensates the residual energy in the energy conversion process between the enthalpy and the Gibbs free energy [21]. Entropy heat is therefore reversible; it is generally endothermic during charge and exothermic during discharge. Joule heat is due to the internal resistance of the cell components such as the positive/negative electrodes and the separator. Joule heat is irreversible and exothermic regardless of the charge process. These sources of heat not only change the temperature but also change the volume of the Li-ion battery. This volume change causes additional periodic thermal stress during operation and affects the lifespan of the cells and packs. Therefore, many efforts have been devoted to characterize the thermal expansion of the host materials in micro-scale [39-41]. These studies provide a useful foundation for understanding the thermal characteristics of the active materials. However, the dynamic thermal mechanics at the cell-level are more complicated because of the hundreds of contact surfaces between electrodes and mechanical constraints such as wounding shape of the jellyroll and clamping current collectors with bus bars in the edge sides. Our previous study showed for the first time that thermal swelling is similar in order of magnitude with Li-ion intercalation swelling and thereby far from insignificant [42]. However, studies of thermal expansion on the cell-level are still few, making it difficult to estimate the thermal stress due to thermal expansion, while the swelling due to electrochemical reaction, i.e. Li-ion intercalation, has intensively been investigated from micro-scale to macro-scale [5,18,19,25]. Especially, the most important property which comes from both the material and its structure inside the cell, i.e. the equivalent coefficient of thermal expansion on the cell-level, was never reported before, even though this property is crucial not only to predict the dynamic thermal mechanics of battery cells but also to estimate periodic thermal stress/strain on packs. Moreover, the modeling of the thermal expansion on the cell-level with the measured material property has not been investigated in great detail, although characterizing the thermal expansion has become important to prolong the life of Li-ion batteries. The limited information about thermal stress and strain on the cell-level stimulates the quantification of thermal stress and strain on the battery cells and packs, which affect the battery performance in packs.

In this paper, we report results and models obtained by measuring the expansion of a cell. High-precision displacement sensors were used to measure the cell-level swelling arising from charge/discharge of an unconstrained graphite/nickel-manganese-cobalt-oxide (NMC) cell whose temperature was regulated in a thermal chamber. The measured thermal expansion was observed to vary significantly with experimental control parameters and also was

observed to exhibit nonlinear characteristics with respect to temperature. An equivalent coefficient of the thermal expansion was calculated as a function of the state-of-charge (SOC) at a variety of locations. A novel thermal swelling model is proposed based on the experimental results. The proposed model uses the measured equivalent coefficient of thermal expansion to estimate the thermal swelling. Moreover, a 1-D heat conduction model is introduced to account for the temperature distribution through the cell for a more accurate estimation of thermal swelling. The proposed model was verified by comparisons with experimental data consisting of thermal expansion at various C-rates, both during operation and relaxation periods. The experimental validations confirm that the proposed model accurately predicts experimental observations in a variety of operational conditions. Such an accurately model, able to estimate cell thermal behavior, may be beneficial to the design and management of not only single cells but also battery packs.

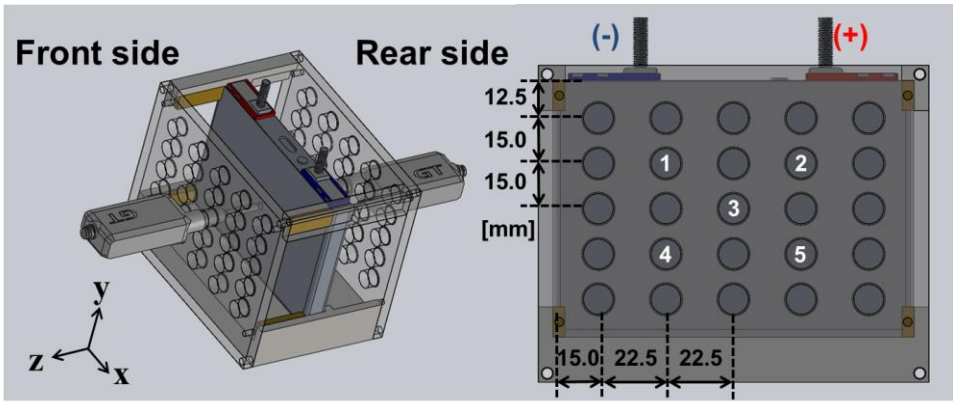

Figure 8.Schematic diagram of the experimental setup showing the fixture, the cell, and the sensor locations 1-5.

3.2. Experiments

This study used a flat-wound type prismatic 5Ah Li-ion cell obtained from a Ford Fusion HEV battery pack. Detailed information of the Li-ion cell is available in Ref. [42].

The free swelling of the cell was measured with high-precision contact-type displacement sensors with 1µm accuracy and 0.1µm resolution (Keyence GT2-H12KL, Japan). The sensor head creates a contact force on the battery surface of less than 0.3N. The sensor was installed in a fixture as shown in Figure 8. The fixture was made from ABS plastic using a rapid-prototyping machine (Dimension Elite FDM, USA). The prismatic cell was constrained at its

eight corners with ABS plastic set-screws in the fixture, but was otherwise unconstrained. The fixture was placed inside a thermal chamber (ESPEC BTZ-133, Japan) with controlled desired temperature. Two thermocouples were also used. One thermocouple was installed on the center of the cell to measure cell surface temperature (in a location that avoided interference with the displacement sensors). The other thermocouple was installed between the fixture and the cell to measure near-surface ambient temperature. The battery cell was operated by using a battery & cell test equipment (MACCOR Series 4000).

A first experiment was carried out to assess the thermal expansion characteristics of the cell over the SOC. In this experiment, relative thermal expansion in the z direction, which is perpendicular to the multi-layer electrode sandwich, was measured with a variety of SOCs at five locations labeled 1–5 in Figure 8. Prior to discharge, the battery was fully charged using a standard constant current, constant voltage charging profile at 2A (0.4C) at 25℃; the voltage was clamped after reaching 4.1V, at which it was held until the current tapered to C/100 (50mA). To obtain the desired SOC, the battery was discharged with a 0.4C current for an appropriate time. For example, 1.25 hour discharge time was used to obtain a 50% SOC. The battery was allowed to rest at open circuit for 1 hour to ensure full relaxation at the end of discharge. Then, the temperature of the thermal chamber was incrementally changed from 5℃ to 45℃ with 5℃ increments. Each temperature variation was followed by 5 hours of rest time to ensure thermal equilibrium. This procedure was repeated from 0% to 100% SOC with 25% SOC increments.

The second experiment repeated the same temperature profile (from 5℃ to 45℃ with a 5℃ increment) of the first experiment with an aluminum block instead of the cell. That was done to characterize the thermal expansion of the fixture and the sensors because they also expand or shrink when the ambient temperature varies. Five sensors were installed on one side of the cell at the same locations as in the first experiment. One other sensor was installed in the center of the opposite face of the cell (without contacting the cell) to observe the thermal behavior of the sensor itself.

In a third experiment, swelling at several C-rates was measured for the validation of the thermal swelling model. The net displacement at the center of the battery was measured with respect to the charge state during discharge using a standard constant current discharging profile. All discharges were performed down to 3.0V. Measurements with exterior thermocouples showed that the lowest current used, 0.2C (1A), did not cause significant

heating. The battery-cell surface remained within 0.1℃ of the 25℃ ambient temperature during discharge. Data at 0.2C therefore allows direct correlations to be made between swelling and Li-ion intercalation in a cell sandwich without significant convolution by thermal expansion. In contrast, the cell surface temperature deviated more significantly from the ambient at high C-rate tests where temperature variations produced considerable thermal swelling.

In a fourth and last experiment, pulse excitation experiment was carried out to assess the viability of the proposed model in HEVs. The displacement sensors were placed at the geometric centers on both faces of the cell normal to the cell surface (location 3 shown in Figure 8). The battery was fully charged using standard CCCV protocol prior to discharge. Then, the battery was discharged with a 2A (0.4C) current for 1.25 hour to obtain a 50% SOC. The battery was allowed to rest at open circuit for 3 hours at the end of charge and discharge respectively. Then, pulse current was induced to the battery cell at 7.8 C (39A) with twenty-second (10 second charge and 10 second discharge) period for 720 seconds to obtain pure thermal expansion. The induced current was the maximum current in the current setup. The maximum capability of the battery test equipment is 40A. The SOC is minimally changed during pulse excitation, suggesting that the swelling in this experiment originates from the resistive heating, and thereby the swelling measured can be considered as pure thermal swelling.

3.3. Thermal swelling model

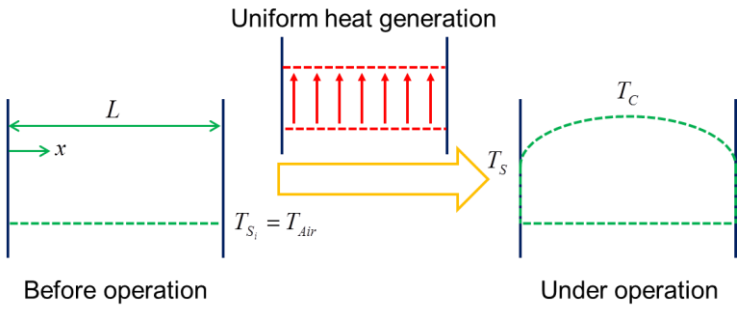

Figure 9.Temperature distribution through the cell before and under operation.

When a jellyroll is fabricated, positive/separator/negative electrodes are wound. The individual layered sheets are thin. The thickness of each component is of the order of dozens of micrometers. Hence, lumped parameters – which represent equivalent material properties of stacks of thin individual anode/separator/cathode layers – are frequently used to describe the thermal behavior of the cell [43,44]. Moreover, it is reasonable to assume uniform heat generation through the cell [21,45,46].

Prior to operation (charge or discharge), the temperature is constant through the cell and the same as the ambient temperature because the cell is at thermal equilibrium. However, temperature variations occur during operation through the cell. Assuming uniform heat generation and lumped parameters, the temperature distribution across the cell thickness is parabolic, as shown in Figure 9 [21]. This temperature distribution is due to the assumed uniform heating caused by Joule heat and entropy heat. The non-uniform temperature distribution is important when estimating the thermal swelling of the cell. The thermal swelling normal to z direction (shown in Figure 8) can be expressed as

$$s_h = \alpha \int_0^L (T(x) - T_{S_i}) dx, \tag{2}$$

where s_h, L, α, T represent the thermal swelling (due to cell heating/cooling), the original thickness of the cell, the (lumped) coefficient of thermal expansion, and the temperature, while subscript S_i denotes the initial state of the surface.

Similar to the modulus of elasticity and the interlayer spacing of the graphite lattice [20,47], the equivalent coefficient of thermal expansion α can be affected by the phase transition of the electrodes. Thus, α is a function of SOC, which varies in time. Hence, α varies in time.

A linear temperature distribution across the cell is obtained for a uniform heat generation. The corresponding thermal swelling can be computed by integrating Eq. (2) to obtain

$$s_h(t) = \alpha(t) L \left[\frac{2}{3} (T_C(t) - T_S(t)) - (T_S(t) - T_{Ref}) \right], \tag{3}$$

where t is time, T_{Ref} is a reference (ambient) temperature, while T_C and T_S are the core and surface temperatures which vary in time. The reference temperature T_{Ref} is equal to the surface temperature T_{S_i} at the initial state because the cell is initially at thermal equilibrium. The first term, $\frac{2}{3}\alpha(t) L \left(T_C(t) - T_S(t)\right)$, is a component of the thermal swelling due to

temperature variation across the cell. The second term, $\alpha(t)L(T_S(t)-T_{Ref})$, is the component of the thermal swelling due to the difference between the current surface temperature and the reference temperature.

The core, surface, and ambient temperatures, and the equivalent coefficient of thermal expansion are needed to estimate the thermal swelling in Eq. (3). The ambient and surface temperatures, and the equivalent coefficient of thermal expansion of the cell, are measureable and thereby available. However, it is hard to measure the core temperature of the cell. Thus, to predict the core temperature during operation, a 1-D heat conduction model is used. This model can be expressed as

$$C_{cell}\frac{dT_C(t)}{dt}=i^2(t)R+i(t)T_C(t)\frac{dU}{dT}(t)+2K_{cross}\frac{A_{cross}}{L/2}(T_S(t)-T_C(t)), \tag{4}$$

where C_{cell}, i, R, U, K_{cross} denote the cell heat capacity, the current, the electric resistivity, the potential, and the thermal conductivity for the through-plane direction (Figure 8) of the cell, while A_{cross} denotes the cell surface area. This model includes two heat sources: Joule heat, $i^2(t)R$, and entropy heat, $i(t)T_C(t)\frac{dU}{dT}(t)$.

During operation, the SOC is variable and hence the coefficient of thermal expansion is variable. In contrast, the SOC is constant during the relaxation period after a discharge, and no phase transitions occur. Hence, the coefficient of thermal expansion is constant during the relaxation period. The swelling and the core temperature during the relaxation period can be expressed as

$$s_h(t)=\alpha_{rel}L\left[\frac{2}{3}\left(T_C(t)-T_S(t)\right)-\left(T_S(t)-T_{Ref}\right)\right], \tag{5}$$

$$C_{cell}\frac{dT_C(t)}{dt}=2K_{cross}\frac{A_{cross}}{L/2}\left(T_S(t)-T_C(t)\right), \tag{6}$$

Therefore, the equivalent coefficient of thermal expansion for the relaxation period α_{rel} can be obtained from Eq. (3) applied at the end of discharge. Also, Eq. (4) in the relaxation period can be written as Eq. (6). This shows that the core temperature during the relaxation period has a first order response similar to the surface temperature [48] as there is no heat source in the cell.

3.4. Results and Discussion

3.4.1 Thermal behavior of the cell

In a first experiment, a quasi-equilibrium thermal swelling of the cell was measured, ranging from 5℃ to 45℃ with 5℃ increments. The measured thermal swelling has to be calibrated because the measured value is the total thermal expansion, which includes the expansion of the sensor and that of the fixture, as shown in Eq. (7).

$$s_{measured} = -s_{fixture} + s_{sensor} + s_h , \tag{7}$$

where $s_{measured}$ is the measured swelling, $s_{fixture}$ is the fixture swelling, and s_{sensor} is the sensor swelling. The negative sign of $s_{fixture}$ captures the fact that the fixture holds the sensor used to measure swelling, and hence the sensor indicates a lower value when the fixture expands.

In the second experiment, the cell was replaced by an aluminum block of the same dimensions. Measuring the swelling in this experiment, and knowing the actual swelling of the aluminum block (by knowing the dimensions and the thermal expansion coefficient of aluminum) allowed us to identify the swelling of the sensor and the fixture $\left(-s_{fixture} + s_{sensor}\right)$. Also, the thermal swelling of the sensor s_{sensor} was characterized by using the sensor installed on the opposite face of the cell without contacting the cell. Note that the exact thermal behavior of the sensor is not needed for the calibration. The combined swelling of the sensor and the fixture $\left(-s_{fixture} + s_{sensor}\right)$ was measured in the second experiment and that is enough to estimate the pure thermal swelling of the cell in Eq. (7). However, the thermal behavior of the sensors was evaluated to clearly quantify the root cause of the thermal expansion in the measured data.

Figure 10 (a) and (b) shows the thermal swelling of the sensor and the fixture. The symbols show measured values and the solid lines represent least-square fitted lines from the measured values. The thickness at 5℃ is taken as reference. Also, the sensor output at 5℃ is set to zero (the sensor measures relative displacements). The fitted lines are in excellent agreement with measured thermal expansion in that the coefficient of determination (R^2) is over 0.998 for all fitted data.

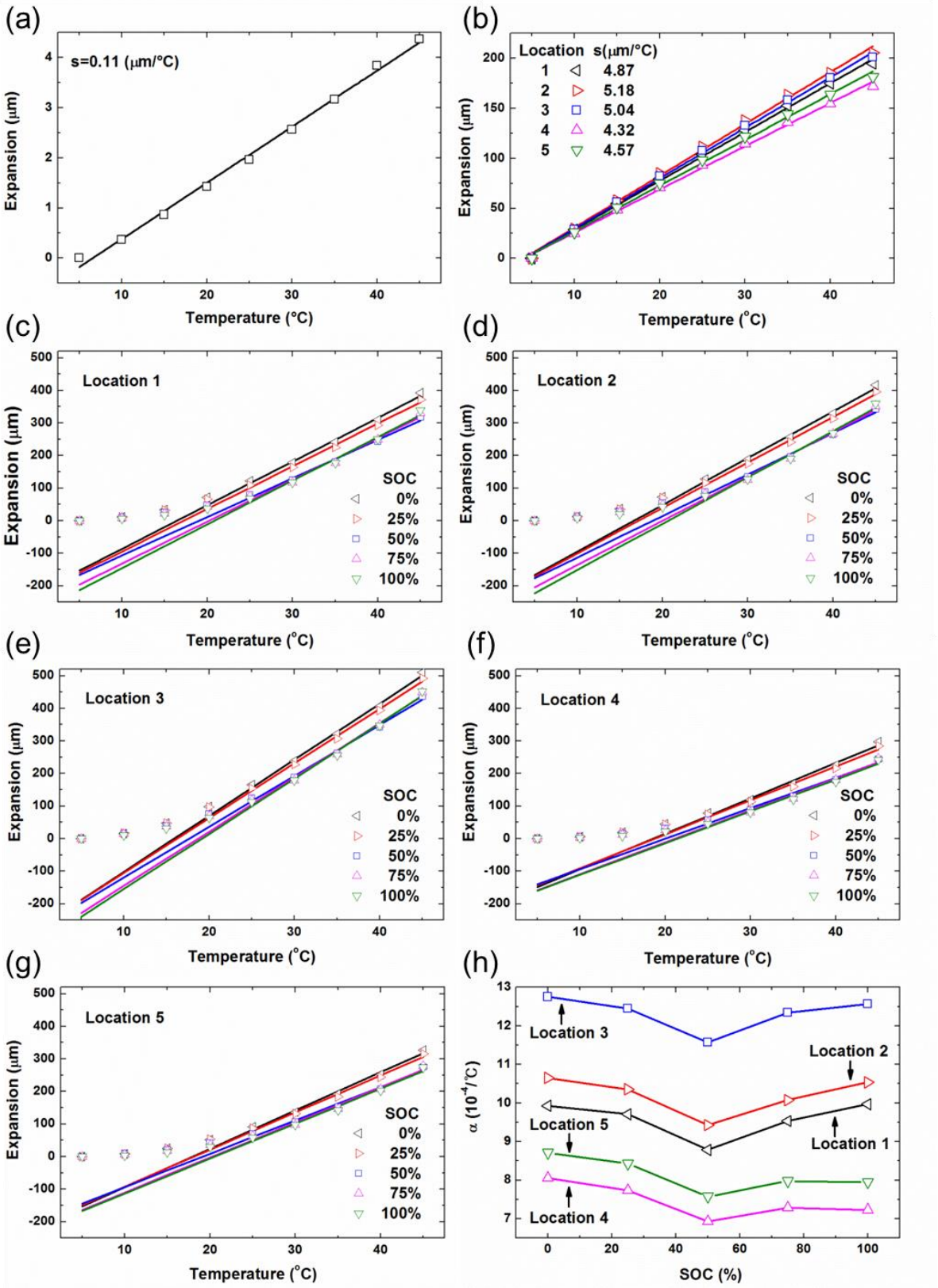

Figure 10.Thermal expansion of (a) the sensor, (b) the fixture, (c) - (g) the cell at location 1 - 5, and (h) the equivalent coefficient of thermal expansion of the cell as a function of SOC at a variety of locations; the symbols and the solid lines represent measured values and least-square fitted lines from the measured values in (a) and (b); the symbols and the solid lines indicate calibrated thermal swelling of the cell and least-square fitted lines from measured

data ranging from 25℃ to 45℃ in (c)-(g).

The swelling of the sensor and the fixture is linear with the temperature (in the measured range). However, the thermal expansion of the fixture is slightly different at each measurement location. This difference might be due to the manufacturing process and the geometric complexity of the fixture. The fixture consists of five components (Figure 8) manufactured using a rapid prototyping machine. This manufacturing process is known to create significant internal residual stresses. Moreover, the fixture components are stressed also during assembling. This internal and assembly stresses are small. However, the measured swelling is of the order of tens of microns. Therefore, the effects of the internal stresses in the fixture may not be negligible. Moreover, steel bolts were used to assemble the fixture. They have a different coefficient of thermal expansion than the rest of the fixture which is made of ABS plastic. Steel has much smaller value for the coefficient of thermal expansion than ABS plastic. Thus, the fixture likely exhibits a non-isotropic thermal expansion. In conclusion, the measured thermal expansion should be calibrated point by point to estimate reliable, pure thermal expansion of the cell.

Figure 10 (c)-(g) illustrate the thermal swelling of the cell ranging from 5℃ to 45℃ at five locations on the cell. These thermal swelling values were calibrated by using Eq.(7). The symbols indicate calibrated thermal swelling of the cell, and the solid lines represent least-square fitted lines from measured data ranging from 25℃ to 45℃ in Figure 10 (c)-(g). The thermal swelling increases in a nonlinear fashion below 25℃, and in a linear fashion above 25℃ at all locations, regardless of SOC. This result suggests that the jellyroll initially has small gaps inside (e.g., between electrode layers [6]). When the jellyroll starts to swell in the low temperature range below 25℃, these gaps are eliminated/filled first. Once the gaps are filled in the high temperature range above 25℃, the thermal expansion increases linearly with the temperature because the gaps are already filled, and the thermal expansion of the jellyroll fully contributes the expansion of the cell casing.

The thermal swelling at point 3 in Figure 8 (i.e., the center of the battery) is the largest. The swelling decreases near the edges because of the mechanical constraints imposed by the battery casing. The stiffness of the casing near the edges is larger than in the center. Therefore, the center region is mechanically easier to dilate.

We also note a slight asymmetry in the shape of the thermal swelling, which translates in the asymmetry in the equivalent coefficient of thermal expansion shown in Figure 10 (h). That is

similar to Li-ion intercalation swelling, and is due to the non-symmetric geometry of the position of the jellyroll inside the casing [16,42]. Note again that the measured thermal swelling is not the pure thermal swelling but the equivalent thermal swelling of the battery cell, which reflects mechanical constraints and the hundreds of contact surfaces between folds of the electrodes. Hence, mechanical constraints play a critical role in the thermal swelling of this system together with the thermal expansion of the jellyroll. Nonetheless, the shape (spatial distribution) of the thermal swelling is approximately parabolic based on measurements at five locations. The shape of the thermal swelling appears to be different from that of Li-ion intercalation swelling. That is not surprising as the thermal swelling has a different physical origin compared Li-ion intercalation swelling.

The values of the equivalent coefficient of thermal expansion can be calculated for the measured locations from the data collected from 25℃ to 45℃. The basic premise is that the thermal swelling varies linearly with the temperature in the range of operational temperatures of the cell, but it contributes to fill the empty space in the low temperature regions.

The measured equivalent coefficient of thermal expansion shows a dependency also on SOC (Figure 10 (h)). This dependency originates from the phase transition of both the graphite and nickel-manganese-cobalt-oxide electrodes under charge or discharge [17,51] because the phase transition also accompanies the changes of material properties [52,53]. However, the maximum difference is within 10%. This is not significant considering that a large amount of Li-ions move from a cathode to an anode during discharge.

Interestingly, the order of magnitude for the equivalent coefficient of thermal expansion of the cell is similar to that of a polyethylene and a polypropylene [50] (main materials for a separator [49]), while the coefficient of thermal expansion of host materials and electrodes is much smaller than that for the cell [39-41]. The coefficient of thermal expansion for a polyethylene is between 10^{-4} and $3 \cdot 10^{-3}$ K^{-1}, and the coefficient of thermal expansion for polypropylene is $6.5 \cdot 10^{-5}$ to $0.9 \cdot 10^{-3}$ K^{-1} [54]. Thus, the separator might play an important role in the thermal expansion. Note that the material properties of polymer materials significantly depend on many things such as the atomic structure, the density of materials, and the manufacturing process. Therefore, there is typically a wide range of variation in polymers, and that is a reason why much research has been carried out to measure the material properties of individual polymer materials [55].

$$\alpha_{total} L_{total} = \sum \alpha_i L_i \,, \tag{8}$$

Specifically, a separator, current collector, cathode, and anode take 28%, 24%, 24%, and 24% of the total thickness of the cell [42]. Therefore, the estimated coefficient of thermal expansion for a separator by using Eq. (7) varies from $2.5 \cdot 10^{-3}$ K^{-1} to $4.2 \cdot 10^{-3}$ K^{-1} upon location considering the stacked materials; the detail configuration of the jellyroll used is described in Ref. [16] where the cross-section view of the jellyroll and the geometry inside of the cell is available from X-ray tomography in Ref. [56] (not shown here for the sake of brevity). The coefficients of thermal expansion for the current collectors and the graphite anode are assumed to be $2.3 \cdot 10^{-5}$ K^{-1} and $5.5 \cdot 10^{-5}$ K^{-1} [39]. The coefficient of thermal expansion for the NMC cathode is assumed to be the same as that for graphite (because the coefficient of thermal expansion for the NMC cathode is not available). Moreover, the coefficient of thermal expansion for an insulation sheet between the case and the jellyroll [16] is estimated to be $1.0 \cdot 10^{-3}$ K^{-1}. Indeed there is a lack of information for this material; the only information available is that this insulation sheet is made from a polymer material. Note that the estimated coefficient of thermal expansion for a separator is a rough estimation because of the limited information available. The manufacturer did not provide detailed information due to confidentiality and intellectual property rights. Moreover, the thermal expansion of the cell also could be affected by the constraints from the casing and the mechanical magnification of ruffling [6,57]. In particular, the ruffling phenomenon is more severe in the wound cell than the stacked cell because of constrained conditions. Specifically, two winding edges of the jellyroll (top and bottom sides for this prismatic cell) are fixed by the packing foil and two current collectors (left and right sides for this prismatic cell) are clamped by bus bars. At these edges, the interface among cathode, separator, and anode films cannot move, while the rest of the jellyroll (away from the constrained edges) easily expands and bends with a periodic wavy-like profile when temperature is elevated. This bucking behavior is the most severe and thereby results in the formation of several gaps/voids between electrode films in the center region [57], especially for free-swelling conditions. This phenomenon is not unlike the behavior of a soft beam fixed at both sides and exposed to temperature variations. The beam can bend and buckle due to thermal expansion and constrained boundary conditions. The most significant bending occurs in the middle of the beam. Similar to that, the thermal expansion of a cell is the largest in the center of the cell and the shape of the thermal swelling is convex.

The thermal expansion of electrolytes may not affect the expansion of the case on the cell level due to several reasons. First, the thermal expansion of electrolyte is of a similar order of magnitude with that of current collectors or active materials [58,59]. That suggests that the increase of the porous inside the separator may be larger than that of electrolytes and thereby the expansion of electrolytes do not contribute to the expansion on the cell level. Second, the modulus of elasticity for an electrolyte is at least hundreds of times smaller than that for other materials - the estimate for the electrolyte is 1MPa [60] - suggesting that the thermal expansion of electrolytes minimally generate a reaction force on the contact surfaces, which affects the volume of the overall battery cell. Finally, the battery cell contains a lot of empty space [56]. Therefore, the increased volume of electrolytes due to the temperature elevation just fills the empty space inside of the cell considering its soft modulus of elasticity.

In summary, both separators and mechanical constraints might contribute to the thermal expansion of the cell, even though it is hard to estimate the exact amount of contribution caused by each.

3.4.2 Estimation of core temperature and thermal swelling

The proposed thermal swelling model needs the core temperature of the cell. Therefore, a 1-D heat conduction model is introduced to predict the core temperature. The 1-D heat conduction model needs the equivalent thermal properties of the cell. The other side of this relationship is that the equivalent thermal properties of the cell can be characterized with the core and surface temperatures. Moreover, the core temperature can be calculated from the thermal swelling model, Eq. (3), if the (pure) thermal swelling of the cell is available and measured. In this paper, the equivalent thermal properties of the cell were parameterized with the predicted core temperature, which is estimated from the 5.0C thermal swelling data during discharge. Then, for validation, the 1-D heat conduction model with these thermal properties is applied to predict the thermal swelling at a variety of C-rates during operation as well as during relaxation periods. Details of the validation are described in the next subsection.

When the coefficient of thermal expansion is known, the core temperature can be calculated using measured quantities, namely: thermal swelling of the cell, surface temperature, and ambient/reference temperature. Eq. (3) can be rearranged to obtain the core temperature as

$$T_C = \frac{3}{2}\left[\frac{s_h}{\alpha L} - \frac{T_S}{3} + T_{Ref}\right], \tag{9}$$

However, this equation applies to pure thermal swelling s_h (i.e. no Li-ion intercalation swelling). That is hard to obtain experimentally during charge or discharge directly because Li-ion intercalation swelling and thermal swelling occur simultaneously during operation. Instead of attempting to measure pure thermal swelling, we subtract the Li-ion swelling from the total swelling. This calculation has two premises. First, the total swelling is a sum of the Li-ion intercalation swelling and the thermal swelling. Second, the dependency of the Li-ion intercalation swelling on the C-rate is negligible. For such cases one obtains

$$s_h = s_T - s_{Li}, \tag{10}$$

where s_h, s_T, s_{Li} denote the thermal swelling, total swelling, and Li-ion intercalation swelling. The measured swelling at 0.2C (a dotted line in the top of Figure 11) is assumed to be pure Li-ion intercalation swelling s_{Li} because the temperature variations during discharge at 0.2C are below 0.1℃. Therefore, the pure thermal swelling at 5.0C was obtained by using Eq. (10) and is shown by the dashed line in the top of Figure 11.

Note that the thermal swelling shown in Figure 11 increases due to the raise in temperature, while Li-ion intercalation swelling decreases over the SOC because Li-ion is deintercalated from graphite during discharge.

The core temperature over SOC at 5.0C can then be calculated by using Eq. (9) with the estimated thermal swelling s_h, the equivalent coefficient of thermal expansion as a function of SOC, the measured surface temperature, and the ambient/reference temperature. The equivalent coefficient of thermal expansion measured at the center of the cell surface (location 3 in Figure 8) was used in the model. We used this calculation because the cell expansion is the largest there and of interest. The core temperature estimated is shown by a dashed-dot line in the middle of Figure 11.

Finally, thermal properties such as the equivalent electric resistivity and the equivalent thermal conductivity for the through-plane direction of the cell were parameterized with the estimated core temperature over SOC. The entropy change of this battery is available [61]. The resistivity, the heat capacity, and the thermal conductivity for the through-plane direction estimated were 1.9 mΩ, 97 JK^{-1}, and 0.73 $Wm^{-1}K^{-1}$ respectively. The estimate values are reasonable in that the values have similar order of magnitude with values found in the

literature. For example, the thermal conductivity for the through-plane direction is 0.61 $Wm^{-1}K^{-1}$ in Ref. [62], 0.69 $Wm^{-1}K^{-1}$ in Ref. [63], and 0.75 $Wm^{-1}K^{-1}$ in Ref. [64], which are estimated based on the thickness of each electrode. The heat capacity of battery cells used in HEVs is also 88 JK^{-1} in Ref. [65]. Note that measuring all thermal properties from experiments is very time and cost intensive. The purpose of this study is to create a thermal swelling model, not to identify thermal properties of the cell experimentally.

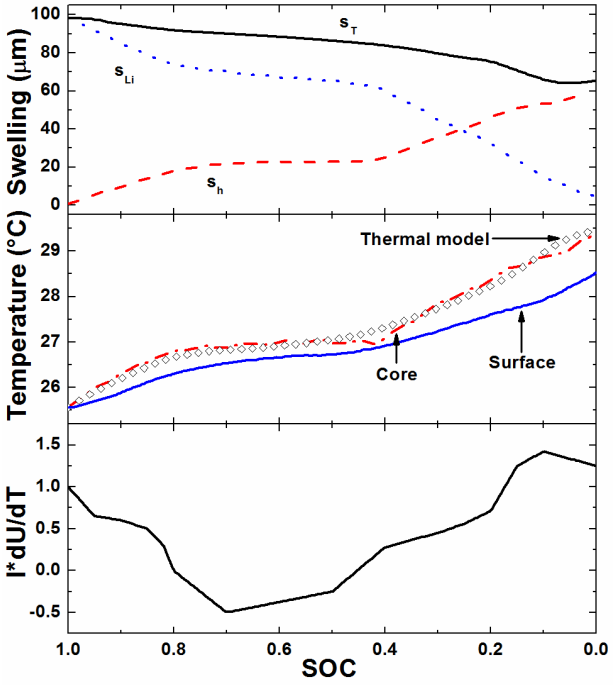

Figure 11.(Top) Swelling, (middle) temperature, and (bottom) entropy change versus SOC at the center of the cell during a 5.0C discharge; the solid line, the dotted line, and the dashed line represent the total swelling, the Li-ion intercalation swelling, and the thermal swelling in the top of the figure; the solid line, the dashed-dot line, and the diamond symbol indicate the surface temperature measured, the core temperature calculated by using Eq. (9), and the core temperature estimated by the 1-D heat conduction model (Eq. (4)) in the middle of the figure.

The core temperature was also estimated using the 1-D heat conduction model in Eq. (4). The measured surface temperature was used to obtain the results shown as diamond symbols in the middle of Figure 11. The model results are in good agreement with the estimated core temperature from Eq. (9). The interesting behavior of the core temperature is between 0.4 and 0.8 SOC. The temperature difference between the core and the surface decreases in this region, even though the Joule heating still exists. To elucidate the reason for this phenomenon, another heat source, namely the entropy change, should be considered as shown in the bottom of Figure 11 [61]. The entropy change is negative in the 0.45 to 0.8 SOC region. This means that the entropy is not a heat source but a heat sink in this region. Moreover, the heat the entropy absorbed is larger than the heat created by the internal

resistance. As a result, the temperature difference between the core and the surface decreases in the 0.4 to 0.8 SOC region. In contrast, the core temperature increases drastically in the 0 to 0.2 SOC region due to the synergy of the Joule heat and the entropy heat. Both of them are positive, i.e. exothermic, in this region. In summary, the entropy heat plays a critical role and should be considered in the cell to predict the exact core temperature during operation.

Figure 12 compares measured thermal swelling with estimated thermal swelling by using Eq. (3) during discharge at 5.0C. Two conditions were simulated in the estimation of thermal swelling to elucidate the effect of the temperature distribution through the cell. The first set of results assumed that the temperature through the cell (in the z direction) was the same, i.e., the temperature distribution is uniform in the direction perpendicular to the cell surface. Under this assumption, the first term, $\frac{2}{3}\alpha(t)L\left(T_C(t)-T_S(t)\right)$, of Eq. (3) is zero. The results in this first set are shown in Figure 12 as circles. The second set of results assumed that the temperature distribution though the battery can be obtained using the 1-D heat conduction equation. In this case, Eq. (4) was used to predict the core temperature. The results are shown by triangles in Figure 12. Finally, the third set of results is shown as diamond symbols. They are the estimated thermal swelling at 5.0C by using Eq. (10), which is perhaps the most direct and accurate measurement possible.

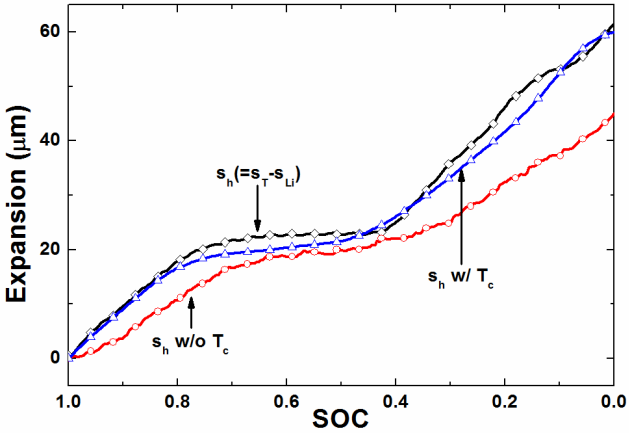

Figure 12.Comparison between experimental and simulated thermal swelling s_h during discharge at 5.0C; the diamond, the triangle, and the circle symbols represent the calculated thermal swelling from experiment by using Eq. (10), the thermal swelling estimated assuming the nonuniform temperature distribution through the battery cell, and the thermal swelling estimated assuming the uniform temperature distribution through the battery cell.

A large difference exists between the measured values and the simulation results when the core and the surface temperatures were assumed to be the same. On the contrary, the simulation results which consider the temperature distribution (and hence consider the

difference between the surface and the core temperatures) correspond well to the measured values. This demonstrates that the temperature distribution through the cell is not negligible from the thermal swelling perspective (because the equivalent coefficient of thermal expansion is large). Therefore, the temperature distribution through the cell should be accounted for in the thermal swelling model (the first term of Eq. (3)) to accurately predict the thermal swelling.

3.4.3 Model validation

The top of Figure 13 illustrates the total swelling over SOC at a variety of C-rates. The symbols show experimental data, while the solid lines show the sum of the thermal swelling simulated by using Eq. (3) and the Li-ion intercalation swelling (i.e., measured swelling at 0.2C) at various C-rates. The thermal swelling in the simulation was estimated by using the surface/ambient temperature measured, the core temperature predicted by the 1-D conduction model (Eq. (4)), and the equivalent coefficient of thermal expansion measured at the center of the cell surface (location 3 in Figure 8).

The higher is the C-rate of the battery when discharged, the larger is the residual (thermal) swelling at the end of discharge. This is because the thermal swelling increases as the discharge progress and the temperature increases, while the Li-ion intercalation swelling decreases during discharge as shown in the top of Figure 6. Therefore, large thermal stress is induced not only in the cell but also in the battery pack during high C-rate operation. This thermal stress might be a major reason for the degradation of cycle life during high C-rate operation [66]. Hence, an accurate model to predict the thermal swelling is useful for the efficient control and management of the cells and packs.

The proposed thermal swelling model was shown to accurately predict the thermal swelling at 1.0C, 2.0C and 5.0C rates, indicating that our approach is reasonable and the estimated thermal properties are accurate. The root-mean-square errors (RMSE) in predicted swelling are 1.13μm, 1.23μm, and 1.25μm at 1.0C, 2.0C, and 5.0C respectively. The accuracy of the displacement sensor and the thermocouple is 1μm and 0.5℃ respectively. The accuracy of the thermocouple alone can result in an error over 1μm (base on the measured equivalent coefficient of thermal expansion). Considering the accuracy of sensors, the proposed thermal model accurately predicts the thermal swelling at various C-rates. Moreover, these results

justify two hypotheses: (1) the total swelling is a sum of the Li-ion intercalation swelling and the thermal swelling: and (2) the rate dependence of the Li-ion intercalation swelling is negligible.

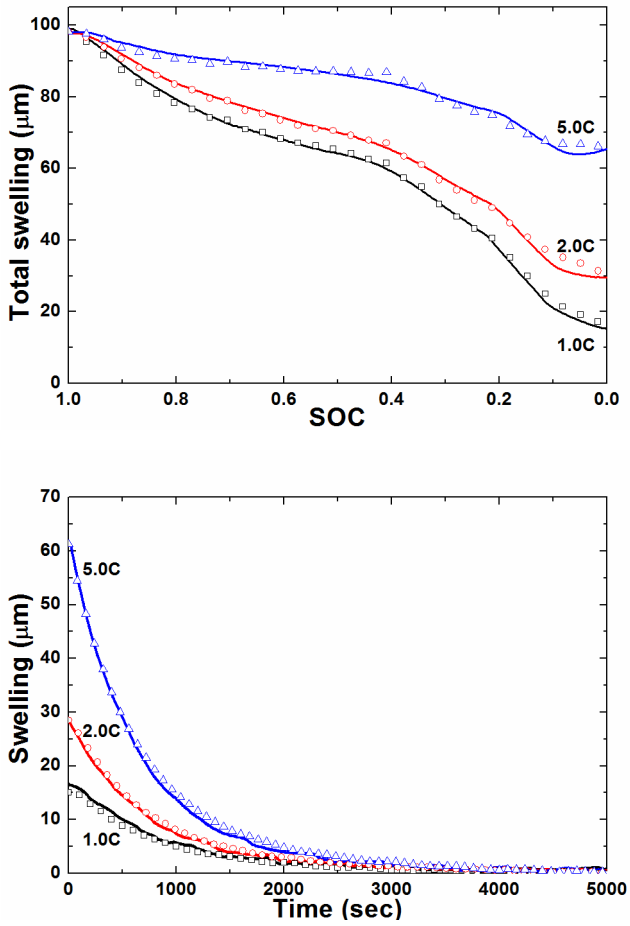

Figure 13.(Top) Total swelling versus SOC at a variety of C-rates during operation and (bottom) total swelling right after discharges at a variety of C-rates during the open-circuit relaxation period on the center of the surface of the cell (location 3 in Figure 1); the symbols show experimental results, whereas the solid lines show model predictions.

For a reliable verification, the total swelling measured is also compared with the total swelling estimated during relaxation period at a variety of C-rates (the bottom of Figure 13). The total swelling estimated is the sum of the thermal swelling calculated by using Eq. (5) and the Li-ion intercalation swelling measured at 0.2C rate. The solid lines show model predictions, while the symbols represent experimental results. The estimated swelling matches well with the measured swelling at various C-rates. These results show that the proposed model predicts the thermal swelling accurately during the operation and relaxation periods at a variety of C-rates.

The trend of temperature and swelling during the relaxation period at 5.0C are shown to elucidate the dynamic thermal mechanics of the battery cell in Figure 14. The core temperature estimated and the surface temperature measured are shown as a solid line and a dashed line in the top of Figure 14. The initial value of the core temperature, which is essential to solving Eq. (6), was obtained from the simulation result for discharge. The initial value of the core temperature for the relaxation period is the last value of the core temperature estimated using Eq. (4) during the discharge. The initial difference between the core and the surface temperatures is over 1℃. As the relaxation progresses, the surface and the core temperatures decrease, and the difference between them also decreases to reach the final thermal equilibrium. The surface temperature converges to the ambient/reference temperature. The core temperature converges to the surface temperature. Eventually, both temperatures converge to the ambient/reference temperature after enough relaxation.

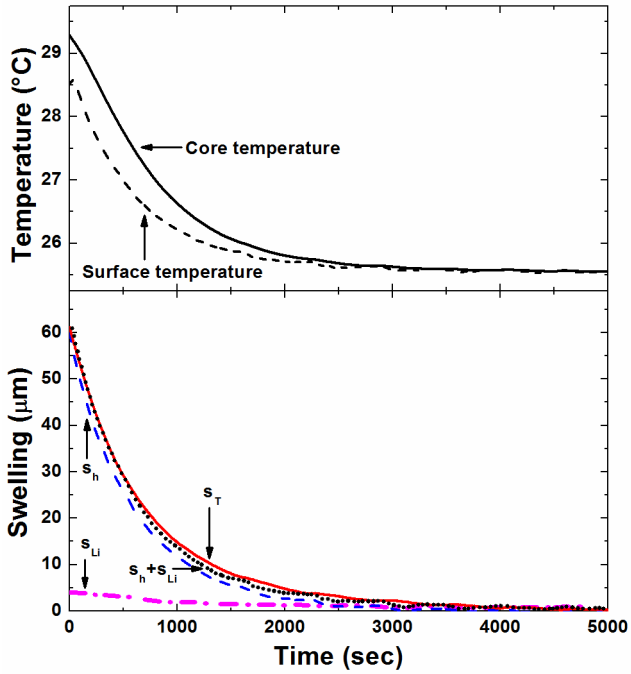

Figure 14.(Top) Temperature and (bottom) swelling over time right after a 5.0C discharge during the open-circuit rest period on the center of the surface of the battery (location 3 in Figure 8); the solid line and the dashed line denote the core temperature estimated and the surface temperature measured in the top of figure; the solid line, the dashed line, the dashed-dot line, and the dotted line represent the total swelling measured, the thermal swelling s_h estimated by using Eq. (5), the Li-ion intercalation swelling s_{Li}, and the sum of the estimated thermal swelling and Li-ion intercalation swelling ($s_h + s_{Li}$) in the bottom of figure.

The swelling during the relaxation period is shown in the bottom of Figure 14. The dashed line shows the thermal swelling s_h estimated by using Eq. (5). The dashed-dot line shows

the Li-ion intercalation swelling s_{Li}. The dotted line represents the sum of the estimated thermal swelling and Li-ion intercalation swelling ($s_h + s_{Li}$). The solid line is the total swelling measured at 5.0C. The sum of the thermal swelling and the Li-ion intercalation swelling corresponds well with the total measured swelling. These results also corroborate the two hypotheses, namely: (1) the total swelling is a sum of the Li-ion intercalation swelling and the thermal swelling: and (2) the rate dependence of the Li-ion intercalation swelling is negligible.

The model should be validated at higher C-rate to assess model viability for battery health management in HEVs. The result of the pulse excitation experiment at a high charge rate (39A) was compared to the model prediction (Figure 15). The maximum capability (40A) of the battery test equipment was used. The dashed line in the top figure shows the surface temperature measured, whereas the solid line in the top figure represents the core temperature estimated. The dashed line in the bottom figure shows the thermal swelling measured, whereas the solid line in the bottom figure represents the thermal swelling estimated from the model. The measured values were calibrated. The entropic heat is negligible in the pulse experiment. The positive and negative current pulse is repeatedly induced to the battery cell and thereby the total amount of heat from the entropy change is zero. Moreover, the SOC is minimally changed during pulse excitation. Therefore, the swelling in this experiment is pure thermal swelling.

The surface temperature measured converged to 29.4℃ during the pulse excitation because the battery reached the thermally equilibrium state (as seen in the top of Figure 15). The core temperature estimated also converged to 30.7℃ when the battery reached the thermal equilibrium state. Note that this difference between the core temperature and surface temperature is important to estimate thermally induced swelling considering the large coefficient of thermal expansion on the cell level. This again suggests that the temperature difference through the battery cell should be considered to accurately predict the swelling induced from the temperature elevation. The bottom of Figure 8 shows the swelling measured and predicted by the proposed model. The model prediction is in excellent agreement with the measurement. The RMSE between the model and experiment is 1.33μm. This experimental validation confirms that the model has high accuracy even at high C-rate. In summary, the model proposed not only accurately predicts the thermal swelling but also is computationally effective.

The proposed model can be used for battery health management or a supervisory controller of electrified vehicles such as HEVs, EVs, and PHEVs. For example, the coupled electrochemical-thermal model predicts the SOC and the surface/core temperature, which are input variables for the proposed thermal swelling model. The proposed model predicts well the amount of thermal swelling due to temperature elevation. Finally, this information can be used for battery health management. This fully coupled model not only increases the operational window but also reduces the overall price of battery cells and packs. However, several temperature sensors should be installed in the hotspot of a battery pack when there are concerns regarding risk due to uncertainties in the prediction of temperature and swelling. In fact, this risk has stimulated the development of an ultrathin sensor array capable of measuring cell expansion and temperature across multiple cells within a battery pack [67]. The state estimates with closed-loop feedback also improve the accuracy of the model prediction [62]. In summary, installing the minimal number of temperature sensors with an accurate model is the best way not only to improve safety and reliability but also to enhance the commercial viability of battery cells and packs considering the stringent safety standards for vehicles.

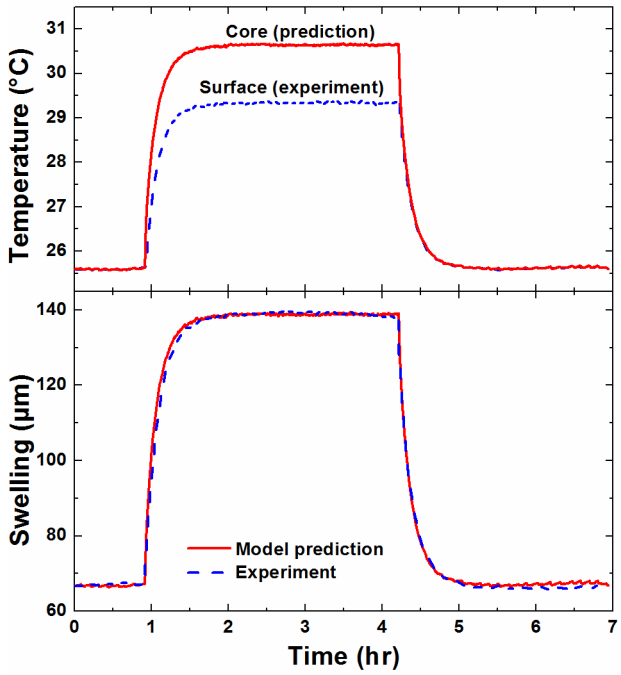

Figure 15.(Top) Temperature and (bottom) swelling over time for 7.8C (39A) pulse excitation experiment; swelling is measured at the center of the surface of the battery (location 3 in Figure 8); the dashed line in the top figure shows the surface temperature measured, whereas the solid line in the top figure represents the core temperature estimated; the dashed line in the bottom figure shows the thermal swelling measured, whereas the solid

line in the bottom figure represents the thermal swelling estimated from the model.

Note that this study only considers the dependency of the equivalent coefficient of thermal expansion on the SOC because the swelling at various C-rates was measured at a constant temperature (25℃). However, the nonlinear characteristics of the equivalent coefficient of thermal expansion at low temperature should be considered if the battery is operated at low temperatures. Moreover, the thermal swelling at a constrained condition might be different due to different mechanical constraints, suggesting that the coefficient of thermal expansion at a constrained condition also different from that at an unconstrained condition. The Li-ion intercalation swelling also should be modeled to predict total swelling of the cell.

3.5. Conclusions

The thermal characteristics of a battery cell were identified. The observed thermal swelling shows a quadratic behavior in low temperatures, while exhibiting a linear behavior in high temperatures at an unconstrained condition. This nonlinear behavior might be caused by contact surfaces between the electrodes because many gaps can be present among electrode layers. Moreover, the thermal swelling depends on the measured location and the SOC because of the complex shape of the cell components, constraints, and the phase transition of each electrode. Therefore, a variety of perspectives should be considered to accurately predict the thermal swelling of the cell and estimate the equivalent coefficient of thermal expansion because Li-ion battery consists of many materials, and their internal shape and connection inside of the cell is complex.

Based on experimental characterization, a novel thermal swelling model was proposed. The proposed model addresses the dependence of the equivalent coefficient of thermal expansion on the SOC and reflects the temperature distribution through the cell. Simulation results show a large difference with the experiment unless considering the temperature distribution through the cell. Through comparison between simulations and experiments, it was verified that the proposed model accurately predicts the thermal swelling at a variety of C-rates during the operation and relaxation periods.

CHAPTER IV

Phenomenological Force and Swelling Models for Rechargeable Lithium-ion Battery Cells

4.1. Motivation and background

Volatility of oil prices, diminishing natural resources, and climate change are triggering many countries to investigate ways to reduce energy consumption. These trends motivate automobile industries to concentrate on the development of eco-friendly, high-efficiency vehicles. Consequentially, electrified vehicles have been successfully deployed on the automobile market, and their market share is increasing. With the growing market for electrified vehicles, attention for Lithium-ion (Li-ion) batteries has increased remarkably because Li-ion batteries are reversible power sources used in electrified vehicles. This trend can be attributed mainly to their ability to combine a high gravimetric/volumetric energy and power density, which leads to compact and low-weight batteries [26-28]. Moreover, low self-discharge rate and long cycle-life with the variety of advantages aforementioned make Li-ion batteries widely popular in portable electronics as well. Indeed, Li-ion batteries are highly versatile energy storage devices for a variety of applications from small-scale portable electronics to large-scale electrified vehicles.

Recent market demands for advanced Li-ion batteries emphasize not only high-energy/power density but also improved reliability and safety for the application of electric vehicles (EVs), and hybrid electric vehicles (HEVs) due to the stringent safety standards for air and ground applications [68]. The safety and reliability of Li-ion batteries, both of which are critical for the development of EVs and HEVs, can be improved with accurate battery models combined with novel battery management strategies. Thus, there have been considerable efforts to

develop battery models to depict the dynamics of Li-ion batteries. These include electrical equivalent circuit models [69,70], electro-chemical models [71], and the heat transfer models [32-35]. Moreover, the exploitation of various control methods and strategies for battery management system (BMS) has been increasing [36,37].

To date, the effects of stresses created in a battery by Li-ion intercalation/deintercalation and the effects of mechanical loads on the cell performance are under intense investigation ranging from micro-scale to macro-scale. That is because cycling and associated mechanical fatigue may lead to performance degradation, capacity loss, and eventual failure [72-75]. Moreover, the effects of prestress and stress evolution on the fading of the battery capacity over time/cycling have been studied [12,76]. This suggests that mechanical damage in electrodes is driven by the stress and strain fields that are induced from repeated cycling. These studies have provided a useful foundation for developing fracture criteria and characterizing the relationship between mechanical forces and Li-ion intercalation during charge and discharge cycles. Moreover, in contrast to micro-scale [33-35] the macro-scale stress and strain responses are directly observable and measurable with high accuracy. This suggests that the development of phenomenological battery models can improve the safety and reliability of batteries, and eventually enhance the lifespan and capability of battery cells and packs.

This paper proposes three phenomenological force and swelling models for Li-ion batteries. The 1-D force model includes a nonlinear elastic stiffness to capture the inherent mechanical consequences of Li-ion intercalation; the measured force not only varies with the state of charge significantly but also shows significant nonlinear characteristics with respect to the amplitude of Li-ion intercalation swelling. Moreover, this model recognizes three separate SOC regions differentiated by phase transitions. The 1st order relaxation model predicts dynamic (transient) swelling during relaxation periods by using a visco-elastic mechanical relaxation approach. The 3-D swelling model uses a higher fidelity finite element model of the battery. This 3-D swelling model accounts for the dependence of an equivalent modulus of elasticity on the state of charge (SOC). Also, the model captures the orthotropic expansion in a direction perpendicular to the electrode surfaces, which is a known physical characteristic of Li-ion intercalation swelling in a jellyroll. Therefore, this model can predict the swelling shape on the battery surface over SOC. Validation was accomplished by comparing predicted overall free swelling shapes with measurements at a variety of SOCs. This model is useful to predict the overall swelling shape and the magnitude of swelling at a

certain location during actual operational conditions, i.e. constrained conditions. The three models proposed herein can be used to improve existing battery management systems by enabling novel power management schemes.

4.2. Experimental

This study used a flat-wound type prismatic 5Ah Li-ion battery cell. Detailed information of the Li-ion battery cell and experimental set-up is available in the literature [42,78].

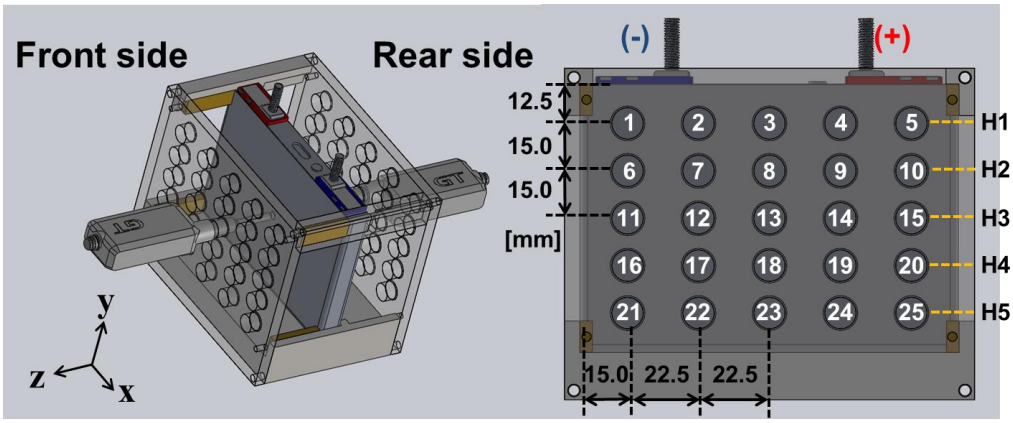

Figure 16. Schematic diagram of the experimental setup showing the fixture, the cell, and the 25 sensor locations labeled 1…25.

In a first experiment, dynamic (transient) swelling was measured over SOC. The net displacement at the center of the battery (location 13 in Figure 16) was measured with respect to SOC during discharge using a standard constant current discharging profile. Prior to discharge, the battery was fully charged using a CCCV protocol at 2A (0.4C) and rested 3 hours at a fixed temperature of 25℃ regulated by a thermal chamber. The voltage was clamped after reaching 4.1V, at which time it was held until the current tapered to C/100 (50mA). Discharge was performed down to 3.0V at 1.0A (0.2C). Measurements with exterior thermocouples showed that the applied current did not cause significant heating. Also, the battery cell surface remained within 0.1℃ from the regulated 25℃ ambient temperature during discharge. The swelling at 0.2C therefore allows direct correlations to be made between swelling and Li-ion intercalation in a cell sandwich without significant convolution by thermal expansion. Note that discharge at a low C-rate is essential to obtain pure Li-ion intercalation swelling because discharge at a high C-rate is accompanied by thermal swelling [42].

In a second experiment, the quasi-static swelling was measured over SOC. In this experiment, the relative expansion in the z direction (perpendicular to the electrodes), was measured at 5 locations labeled as 7, 9, 13, 17, and 19 in Figure 16. Prior to discharge, the battery was fully charged using a CCCV protocol. To obtain the desired SOC ranging from 0% to 100% with 5% increments, the battery was incrementally discharged at a 0.4C rate (0.4C current of actual capacity) with an appropriate time (7.5 minutes). Each incremental discharge was followed by 3 hours of rest time to ensure that the system reached equilibrium after each incremental discharge.

In a third experiment, swelling at the fully charged state was measured with sensors sequentially placed at locations 1 to 25 in Figure 16. This experiment used the same protocol as the first experiment except for the C-rate which was 0.4C. The swelling at the fully charged state was measured after 3 hours of rest time to ensure that thermal swelling due to the increased C-rate does not affect the measurements.

In a fourth experiment, the quasi-static force was measured over SOC with another experimental set-up. Details of the experimental set-up can be found in [79]. Specifically, forces created in a pack of 3 cells were measured during quasi-static charge and discharge with 3 different initial preloads. The battery pack of interest consists of dozens of batteries connected in series, and plastic spacers are placed between cells [79]. To mimic these conditions, the experimental set-up consists of 3 nominally identical cells connected in series and mechanically sandwiched between two 1-inch thick garolite plates assembled with 4 bolts at their corners. Each bolt was instrumented with a load sensor (LC8150-250-100, USA). The entire set-up was placed inside a thermal chamber (Cincinnati Sub-Zero ZPHS16-3.5-SCT/AC, USA) that controls the desired temperature (25°C). The plastic spacers between cells allow air to flow between batteries while also constraining the batteries from expanding. Hence, the force measured in this set-up can represent the force induced from the volume change of batteries in an actual battery pack.

4.3. Phenomenological 1-D force model

4.3.1 Model description

Two different experiments were carried out to characterize the quasi-static response of the battery cell in section 2, namely the swelling versus SOC and the force versus SOC at steady state thermal equilibrium. The relationship between force and swelling can be determined when such two experiments are used together (and the curve of force versus swelling is parameterized by the SOC). However, experimental conditions were different; the swelling was measured at free conditions without the plastic spacer and with no preload, while the reaction force was measured at constrained conditions with the plastic spacer and with preload. Hence, governing equations have to be obtained to couple these two experiments. These equations are derived in this section. Based on governing equations, equivalent stiffness values are obtained for the case, jellyroll, and spacer. Next, the force is predicted at actual operational/pack conditions.

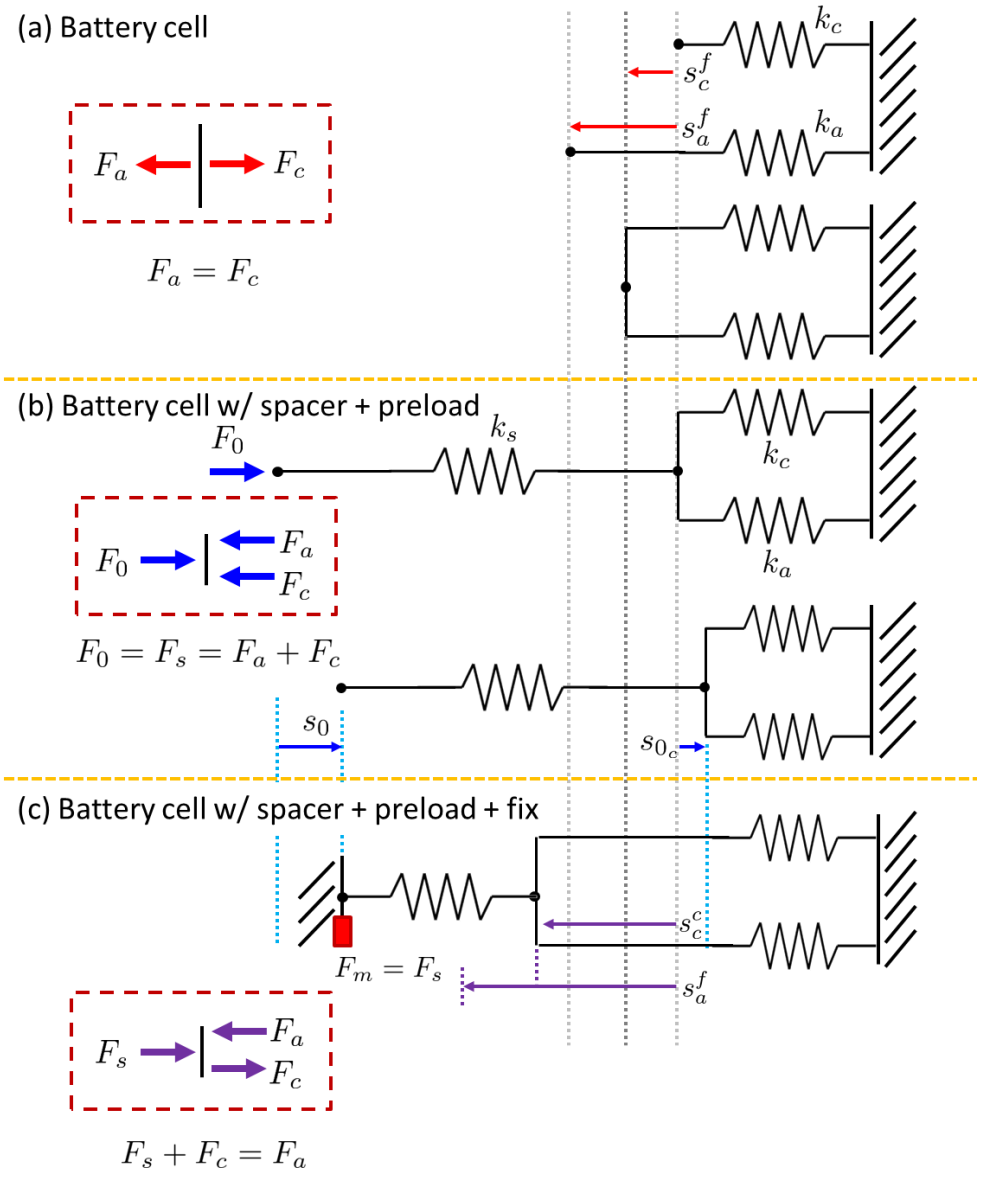

Figure 17. Forces for three cases: (a) free swelling of the battery cell due to Li-ion intercalation; (b) swelling of the battery cell and spacer due to a preload; (c) constrained swelling of the battery cell and spacer due to Li-ion intercalation.

Three different conditions are considered to describe the experiments. These conditions represent the quasi-static behavior of: (a) the battery cell at free conditions during Li-ion intercalation; (b) the battery cell and spacer with a constant preload; and (c) the battery cell and spacer with a constant preload during Li-ion intercalation. It is assumed that the equivalent stiffness at free and constrained conditions is approximately the same.

Figure 17 (a) depicts the quasi-static behavior of the battery cell at free conditions, i.e. the measurement of free swelling without any constraint during Li-ion intercalation. This experiment is conducted with a battery cell which consists of the case and the jellyroll. Thus, two equivalent stiffness elements are modeled: the equivalent stiffness k_{a_1} of the active material (jellyroll), and the equivalent stiffness k_c of the case. Both these equivalent stiffness values refer to the relationship between the total force applied on the cell and the deflection of the cell in a direction perpendicular to the electrodes. Note that these two stiffness elements are connected in parallel (and not in series) because the case disturbs the expansion of the jellyroll. A nonlinear model is used for the jellyroll [82] to capture the dependence of force on swelling as

$$F_a = k_{a_1} s_a^f + k_{a_2} \left(s_a^f \right)^3, \tag{11}$$

where F_a is the force in the jellyroll created by Li-ion intercalation, while k_{a_1} and k_{a_2} are the linear and nonlinear equivalent stiffness values. s_a^f is the swelling of the jellyroll when the jellyroll is not constrained by the case, i.e. the expansion of the jellyroll without any constraints. Superscript f denotes free swelling conditions.

Consider as initial state the fully delithiated state when no force is exerted in the battery cell. When the battery is charged, Li-ions move from cathode to anode. This process leads to a volume expansion of the jellyroll (which leads to the swelling s_a^f). During Li-ion intercalation, the case disturbs the expansion of the jellyroll when the jellyroll is placed inside of the case due to the stiffness of the case. Thus, the equivalent swelling of the battery cell (denoted as s_c^f in Figure 17 (a)) might be smaller than the swelling of the jellyroll without the case.

At the equilibrium state, the jellyroll is compressed, while the case is stretched from their original size because the volume of the jellyroll changes due to Li-ion intercalation. Hence, different forces are induced into each component. A compressive force acts on the jellyroll, whereas a tensile force acts on the case. The resultant force is zero at mechanical equilibrium. Thus, the compression force which acts on the jellyroll (F_a in Figure 17 (a)) is the same as the compressive force which acts on the case (F_c in Figure 17 (a)). The superscript c denotes constrained swelling conditions. The deformation of the case is s_c^f and the deformation of the jellyroll is $s_a^f - s_c^f$ in a direction perpendicular to electrodes at the balanced position. Using Eq. (14), the balance of forces gives

$$k_c s_c^f = k_{a_1}(s_a^f - s_c^f) + k_{a_2}(s_a^f - s_c^f)^3. \tag{12}$$

Figure 17 (b) describes the initial assembly of the force experimental setup where the Li-ion battery cell is assembled with a spacer. Therefore, one more stiffness element which depicts the equivalent stiffness of the spacer (k_s) in a direction perpendicular to electrodes is added in series. An external load (F_0) is applied to the battery in the experiment by tightening the bolts of the fixture. This external load results in initial displacements for the spacer and the case (s_0 and s_{0_c} in Figure 17 (b)). Thus, the total deformation of the spacer is $s_0 - s_{0_c}$. At equilibrium, a compression force acts upon all elements due to the external load. The compression force which acts on the spacer is the external load. Thus, $F_0 = F_s$ as shown in Figure 17 (b). This load is also the same as the sum of forces which act on the case and jellyroll. Thus, $F_0 = F_c + F_a$ as shown in Figure 17 (b). Equating the compression force acting on the spacer with the compression force acting on the case and the jellyroll, one obtains

$$k_s(s_0 - s_{0_c}) = k_c s_{0_c} + k_{a_1} s_{0_c} + k_{a_2} s_{0_c}^3. \tag{13}$$

Figure 17 (c) illustrates the force measurement during Li-ion intercalation at constrained conditions. In this figure, the battery cell and spacer are fixed on both sides by two rigid end plates with a preload. Then, the charge state of the battery cell is changed and the reaction force is measured by the load cells. The unconstrained swelling of the jellyroll s_a^f shown in Figure 17 (a) and 2 (c) is the same because it is the swelling of the jellyroll without any constraints. However, the swelling of the jellyroll and case (s_c^c) is different than the swelling of the jellyroll at free conditions (s_c^f) because of the stiffness of the spacer and because of

the fixed conditions. During operation in constrained conditions, the case is stretched (similar to the free swelling conditions) while the jellyroll and spacer are compressed. The stretching of the case is s_c^c, whereas the compression of the jellyroll and spacer are $s_a^f - s_c^c$ and $s_c^c + s_0$ respectively. Note that the initial displacement of the spacer due to the preload should be considered because the charge/discharge process is conducted with preload. Therefore, a tensile force acts on the case, whereas a compressive force acts on the jellyroll and spacer. The force acting on the jellyroll equals the sum of the forces acting on the case and spacer, as shown in Figure 17 (c): $F_s + F_c = F_a$. This force equilibrium results in

$$k_s(s_c^c + s_0) + k_c s_c^c = k_{a_1}(s_a^f - s_c^c) + k_{a_2}(s_a^f - s_c^c)^3 . \tag{14}$$

The measurement location for the force is the side wall (shown as a filled square in Figure 17 (c)). The load cells are placed between the rigid end plate and the heads of the bolts. Hence, the measured force is the same to the compression force acting on the spacer. One obtains

$$\begin{aligned} F_m &= k_{a_1}(s_a^f - s_c^c) + k_{a_2}(s_a^f - s_c^c)^3 - k_c s_c^c \\ &= k_s(s_c^c + s_0) \end{aligned} \tag{15}$$

Equation (12) defines the relationship between the unconstrained swelling of the jellyroll (s_a^f) and the swelling measured at the center of the case (s_c^f) without any constraints. Using this equation, the swelling of the jellyroll can be obtained in terms of the measured swelling of the case at free conditions as $s_a^f = f(s_c^f)$ (where f is a known function).

Equation (13) defines the relationship between the initial displacement of the spacer (s_0) and that of the battery cell (s_{0_c}) due to the external load. Using this equation, the initial displacement of the spacer can be expressed in terms of that of the case (battery cell) as $s_0 = g(s_{0_c})$ (where g is a known function).

Equation (14) defines the relationship among the unconstrained swelling of the jellyroll (s_a^f), the swelling of the case at constrained conditions (s_c^c), and the initial displacement of the spacer (s_0). Using this equation, the swelling of the case at constrained conditions can be derived in terms of the unconstrained swelling of the jellyroll and the initial displacement of the spacer as $s_a^f = f(s_c^f, s_0)$ (where h is a known function).

Finally, Eq. (15) can be expressed in terms of the measured swelling of the case at free conditions (s_c^f) and the initial displacement of the case due to the preload (s_{0_c}) by using f , g , and h into Eq. (15) to obtain

$$F_m = k_s \cdot h(f(s_c^f), g(s_{0_c})) + (k_s + k_c + k_{a_1}) s_{0_c} + k_{a_2} s_{0_c}^3 . \quad (16)$$

The full expression of Eq. (16) is omitted here for the sake of brevity. The inputs are the free swelling of the case at free conditions and the initial displacement of the case, suggesting that the force due to Li-ion intercalation at actual pack conditions can be estimated if the free swelling in terms of SOC and initial displacement are available.

4.3.2 Parameterization and validation

Figure 18 illustrates the measured force and swelling over SOC due to Li-ion intercalation during discharge at 25℃. The solid line, dotted line, and dash-dotted line are the quasi-static force, quasi-static swelling, and dynamic (transient) swelling at the center point on the battery cell (labeled as 13 in Figure 16). The overall trends for the force and swelling are similar, suggesting that these trends have the same physical origin. The volumetric changes in each electrode cannot be distinguished from the available measured force and swelling. However, the volumetric changes are due mainly to the volume change of the negative electrode (made of graphite intercalation material) because the volume change of the positive electrode (made of nickel/manganese/cobalt-oxide) is less than 1% [19]. Moreover, the overall shape of the measured swelling and force is similar to the average interlayer spacing of graphite within the negative electrode [20]. These observations support the hypothesis that the measured force and swelling can be attributed mainly to volumetric changes within the negative electrode due to Li-ion intercalation. Note that the measured force is around 600N at 0.0 SOC because of the preload.

The difference between the quasi-static swelling and the transient swelling measured at 0.2C is almost the same in high and low SOC regions. In contrast, the difference around 0.5 SOC is larger than other regions even though it is not significant; the maximum difference is 4.5μm in the middle range of SOC. This observation coincides well with the dependency of phase volume fraction on the C-rate [24] and the surface structural disordering during transient states [80]. Especially, the volume fraction of Li_xC_{12} depends significantly on the C-rate [24]. Thus, the swelling in the middle range of SOC might depend on the C-rate. In

contrast, negative electrodes have single phase in high and low SOC regions, suggesting that the swelling might be constant regardless of the C-rate in these regions.

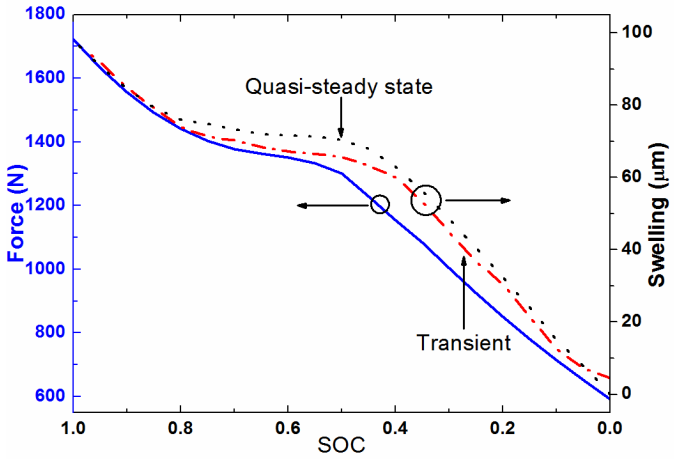

Figure 18. The quasi-static compression force, quasi-static swelling, and dynamic (transient) swelling over SOC during discharge.

The effects of phase transition are more clearly observed in the measured force in terms of swelling at steady-state (shown as symbols in Figure 19). The force increases nonlinearly over the SOC and displays a parabolic shape in regions I and III. Moreover, a sharp change in the relationship between force and swelling is observed in the middle range of SOC, region II. This suggests that the different phases are present in high and low SOC regions [51], and that multiple phases exist around 0.5 SOC [24,81]. Therefore, the hypothesis adopted in this paper is that single phases exist in high and low SOC regions, whereas multiple phases exist in the middle range of SOC. From a structural perspective, this hypothesis suggests two consequences. First, the difference of swelling between transient and steady state at high and low SOC regions may be caused by viscoelastic mechanical relaxation, whereas the difference around 0.5 SOC may originate from both the phase transition and the viscoelastic mechanical relaxation. Second, the material properties in the middle range can be a combination of their values in low and high SOC regions.

The change in porosity in a separator might also contribute to nonlinearity in high and low SOC regions. A decrease in porosity can result in a higher stiffness of the jellyroll because more material is bearing the load [81], manifesting itself as an upward slope in Figure 19.

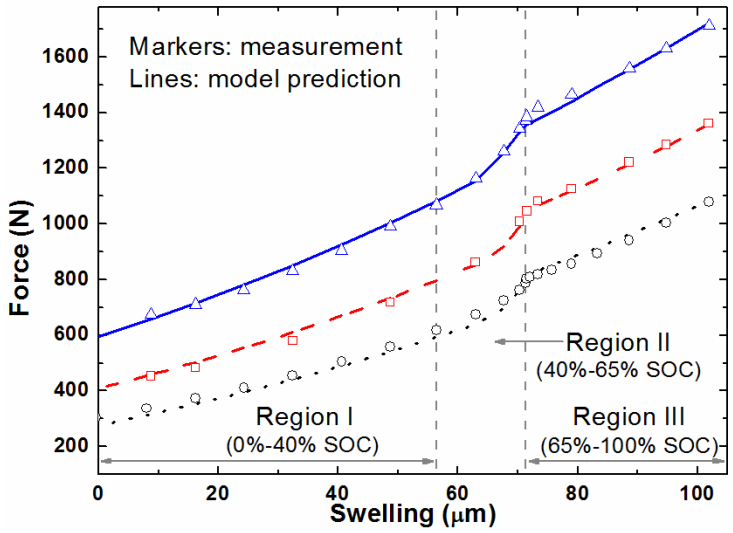

Figure 19. Quasi-static force versus swelling during discharge.

Considering phase transitions, the entire SOC region is separated into three regions to identify parameters of the model proposed in section 3.1: low SOC region (0% - 40%, region I), middle SOC region (40% - 65%, region II), and high SOC region (65% - 100%, region III). It is assumed that (i) the equivalent stiffness of a jellyroll is constant for regions I and separately III, (ii) regions I and III have a different equivalent stiffness for the jellyroll because of the phase difference, and (iii) the equivalent stiffness of the jellyroll for region II is a combination of that for regions I and III because of the multiple phases. Denote as "stage-n" a single Li intercalated layer for every n graphite sheets; see Ref. [51] for the details about the phase transition of the graphite intercalation. Thus, stage-3 is dominant in region I, stage-1 is dominant in region III, and stage-2 is dominant in region II. Also, from a micro-structure perspective the equivalent stiffness of stage-2 is a combination of that of stage-1 and stage-3. Therefore, k_{a_1} and k_{a_2} for region II were estimated by using

$$k_{a(R-II)} = \alpha k_{a(R-I)} + \beta k_{a(R-III)} \text{ (where } \alpha + \beta = 1), \tag{17}$$

where α and β denote contribution factors for each phase respectively, and $R-\bullet$ in the subscript brackets denotes the region. The stiffness of the spacer k_s, that of the case k_c as well as the initial displacement of the battery cell s_{0_c} (due to preload) are the same for all regions because the phase transition does not affect these parameters.

In summary, seven parameters, namely k_s, k_c, $k_{a_1(R-I)}$, $k_{a_2(R-I)}$, $k_{a_1(R-III)}$, $k_{a_2(R-III)}$, and s_{0_c}, were estimated from the measured force and swelling with a nonlinear least squares

method. Then, α and β were explicitly calculated with estimated parameters and the force to estimate the equivalent stiffness of the jellyroll for region II.

The solid line in Figure 19 shows the fitting results with identified parameters based on measurements (triangle symbols). The coefficient of determination (R^2) is over 0.996 for all fitted regions, suggesting that the fitted curves are consistent with measured data. The identified parameters are listed in Table 1. The equivalent stiffness for the case is much smaller than that of the jellyroll because the case is very thin. However, the equivalent stiffness of the jellyroll is much smaller than that of the spacer. This may be due to the voids between in the rolled jellyroll and/or due to the electrolyte inside of the battery cell [6].

Table 1. Estimates of the equivalent stiffness in the model which relates force and swelling over SOC measured by displacement sensors and load cells.

Parameter	Value	Unit
k_s	3.30×10^{8}	N/m
k_c	1.42×10^{5}	N/m
$k_{a_1(R-I)}$	3.31×10^{6}	N/m
$k_{a_2(R-I)}$	6.80×10^{13}	N/m^3
$k_{a_1(R-III)}$	4.45×10^{6}	N/m
$k_{a_2(R-III)}$	5.40×10^{13}	N/m^3

For validation, the model predictions were compared to measurements at different preloads. The initial displacement (s_{0_c}) was the only value adjusted to match the initial force at 0.0 SOC with the same equivalent stiffness of each component as listed in Table 1. The dashed line and the dotted line show model predictions in Figure 19, whereas the square symbols and the circle symbols show measured data at different preloads. The model predictions are in excellent agreement with the measured data, suggesting that the estimated parameters are reliable and accurate and thereby the proposed model can predict the electro-chemical induced force at any preload during the operation conditions, i.e. actual pack conditions.

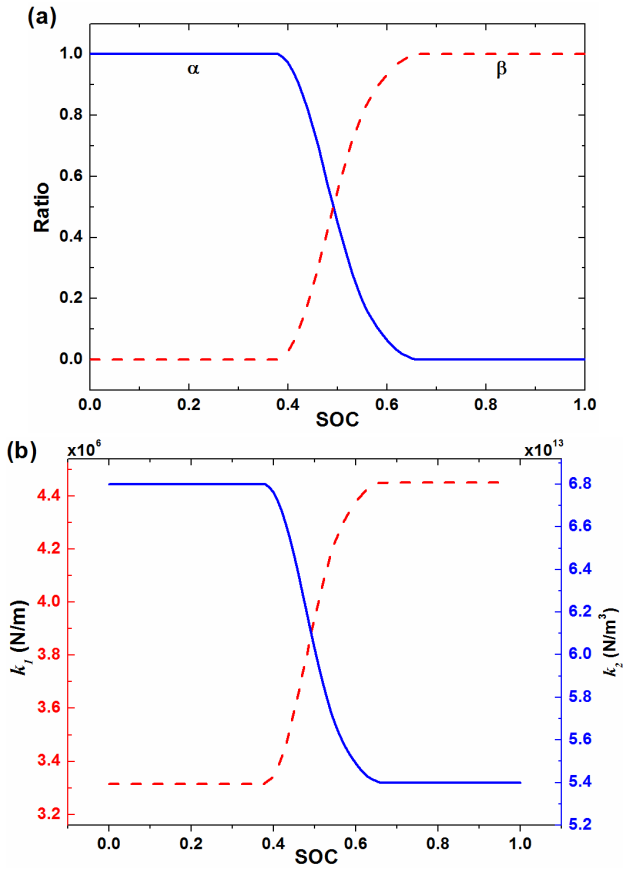

Figure 20. (a) Variation of α and β over SOC. (b) Variation of equivalent stiffness values over SOC.

Figure 20 (a) illustrates the variation of the contribution factors α and β over SOC. A solid line shows values of α, while a dashed line shows values of β. Constant values of α and β are shown in regions I and III because no phase transitions are assumed to occur in these regions. In contrast, the value of α decreases and the value of β increases over SOC in region II. This can be explained by the phase transition of the negative electrode. A transition from stage-3 to stage-1 occurs in this region at the negative electrode over SOC. Thus, the phase volume fraction of stage-3 decreases, whereas the phase volume fraction of stage-1 increases in the negative electrode over SOC. Figure 20 (b) shows the variation of the equivalent stiffness over SOC. Similar to the contribution factors, each equivalent stiffness is constant in regions I and III, whereas they vary in terms of SOC in region II.

4.4. Phenomenological relaxation model

The key idea for a relaxation model is that the force due to the volume change of a cell has two main origins: elasticity and 1st order viscoelastic mechanical relaxation. However, no viscous force occurs at steady state where all velocities are zero. One obtains

$$\begin{aligned} F_{E_D} &= F_{E_S} + F_{V_D} \\ &= F_{E_S} + c\dot{s}_{c_D}^{f}, \end{aligned} \tag{18}$$

where F_{E_S}, F_{E_D}, and F_{V_D} represent the elastic force at steady state, the elastic force at a dynamic state, and the viscous force (at a dynamic state). Thus, the swelling difference between the steady and dynamic states in high and low SOC regions may originate from the 1st order viscoelastic mechanical relaxation as aforementioned in section 3. Note that the difference in the middle range of SOC is due to the dependency of phase volume fraction on the C-rate as well as the mechanical relaxation.

Consider the relaxation of the battery cell following a full discharge. Since phase transitions have concluded before this relaxation period starts, the temporal variation of the force and swelling can be modeled with two 1st order relaxations (two time constants); one for the thermal relaxation and the other for the viscoelastic mechanical relaxation [42].

The elastic force in a battery cell due to Li-ion intercalation is the sum of the force due to two spring elements in Figure 17 (a) at free swelling conditions (because these two springs are connected in parallel), namely $F_E = (k_s + k_{a_1})s_c^f + k_{a_2}\left(s_c^f\right)^3$. Therefore, the elastic force at steady and also at dynamic states can be estimated with the measured swelling at steady $s_{c_S}^f$ and dynamic states $s_{c_D}^f$. Using Eq. (8), the balance of forces can be expressed as

$$c_0\dot{s}_{c_D}^{f}(t) = \left((k_s + k_{a_1})s_{c_S}^{f}(t) + k_{a_2}s_{c_S}^{f\,3}(t)\right) - \left((k_s + k_{a_1})s_{c_D}^{f}(t) + k_{a_2}s_{c_D}^{f\,3}(t)\right), \tag{19}$$

where c_0 is an equivalent coefficient of the 1st order viscoelastic relaxation. The coefficient c_0 can be estimated by using measurements at one SOC value (e.g., at 0.0 SOC) to obtain

$$c_0 = \frac{1}{\dot{s}_{c_D}^{f}(t)}\left[\left((k_s + k_{a_1})s_{c_S}^{f}(t) + k_{a_2}s_{c_S}^{f\,3}(t)\right) - \left((k_s + k_{a_1})s_{c_D}^{f}(t) + k_{a_2}s_{c_D}^{f\,3}(t)\right)\right], \tag{20}$$

The results in Figure 18 show that there is a difference between the measured quasi-static swelling and dynamic swelling (at 0.2C). In particular, this difference can be observed at 0.0 SOC. In addition, the value of $\dot{s}_{c_D}^{f}$ can be obtained by using finite differences in time. Next, the value of $\dot{s}_{c_D}^{f}$ together with the values of the quasi-static and the dynamic swelling at the moment when the SOC is 0.0 can be plugged into Eq. (20) to obtain c_0.

Note that the stiffness coefficients and the coefficient of the 1st order viscoelastic relaxation in Eqs. (19) and (20) depend on the SOC. Hence, we use Eqs. (19) and (20) only for a fixed value of SOC, namely 0.0. That is possible because the SOC is constant during relaxation periods and no phase transitions occur during relaxation periods either.

The proposed approach was applied to the relaxation period at the end of a full discharge. The initial swelling for the relaxation period was the swelling measured at the end of a 0.2C discharge. The equivalent stiffness values used were those obtained for region I (see Table 1) because the SOC is 0.0 during this relaxation.

Figure 21 compares the measured dynamic swelling (shown by the symbols) and the model prediction (shown by the solid line) during a three hour relaxation period. The model prediction is in great agreement with the measured dynamic swelling considering the accuracy of the displacement sensor (1μm). The maximum difference between the model and measure swelling is 0.75μm, and the root-mean-square (RMS) difference is 0.70μm. This suggests that the estimated parameters are accurate and reliable.

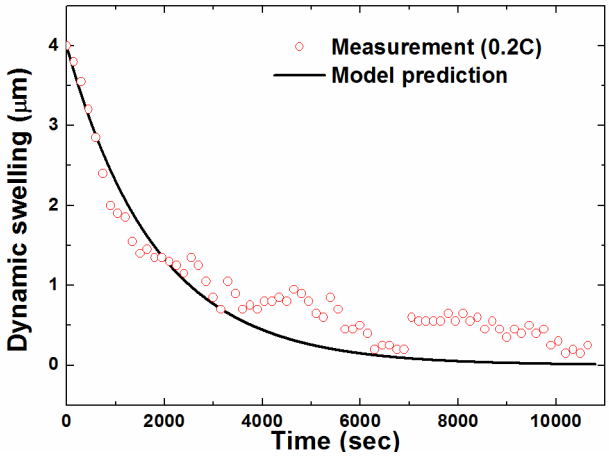

Figure 21. Measured dynamic swelling and simulation results with the phenomenological model during a relaxation period.

Please note the assumptions employed for this model. These require careful consideration when applying this model. Also, the proposed method is an empirical approach whose use requires verification at more SOC values. Moreover, the model requires extensions and modifications for using it in the multi-phase region, i.e. around 0.5 SOC.

4.5. Phenomenological 3-D swelling model

4.5.1 Model description

To predict the swelling shape on the surface during various operational conditions, a 3-D numerical and phenomenological swelling model is proposed in this section. The size and location of the jellyroll inside a battery cell was estimated from the X-ray tomography (shown as a yellow domain in Figure 22) [56]. Information from the dissection showed that the active material region is only slightly larger than the overall contact region between the jellyroll and the battery case. Hence, the contact region was approximated as the active material region (shown as a purple domain in Figure 22). To distinguish the contact region (the center region of the jellyroll) from the noncontact region (top and bottom of the jellyroll), a 100μm gap is modeled between the case and the jellyroll at the top and bottom sides of the jellyroll in the finite element model. Also, only the active material which contacts the case can contribute to the swelling of the case.

The models for other components such as the Aluminum battery case (shown as a semi-transparent gray domain in Figure 22) and the plastic spacer (shown as a semi-transparent blue domain in Figure 22), which was made from polybutylene terephthalate by using injection mold, were also created with measured dimensions. The modulus of elasticity for the Aluminum case is 68GPa. The modulus of elasticity for the spacer is 3.6GPa, a value measured by nanoindentation. This value for the spacer is consistent with previously reported values for polybutylene terephthalate.

These models were created to simulate two conditions. First, the free swelling of the battery cell was simulated to depict the measured swelling shape on the surface of the battery cell; two components, namely the case and the jellyroll, were used for this analysis. Second, the constrained swelling was simulated to illustrate actual pack conditions [79]; four components, namely one case, one jellyroll, and two half spacers, were used. All components were modeled as a homogeneous solid media.

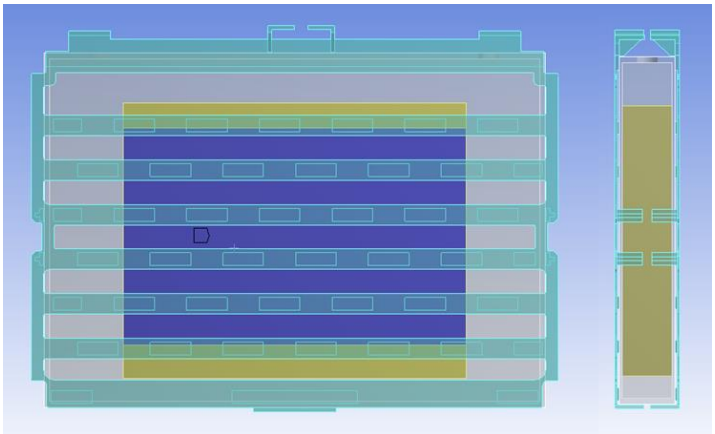

Figure 22. 3-D model of the battery cell. The yellow, semi-transparent white, and semi-transparent blue domains represent the jellyroll, the Aluminum case, and half of the spacer respectively. The purple domain represents the contact region between the jellyroll and the case.

The jellyroll was modeled as a cuboid similar to Ref. [85]. The wound shape of jellyroll was not considered in that this part does not contact the case, and thereby it does not contribute to the swelling of the case. Only half of the plastic spacer was modeled on each side of the battery cell to reduce computational time. The spacer model was assembled with the battery cell model by using appropriate boundary conditions. For example, no separation with slip was assigned between the jellyroll and the battery case, between the battery case and the spacer, and between the spacer and the exterior walls. The resulting overall model simulates one of the three cells and the corresponding spacers used in the force experiments. Other components such as bus bars and terminals were not modeled for simplicity. It is assumed that the effects of these un-modeled components are relatively small and local, and thereby negligible.

4.5.2 Estimation of equivalent material properties

Simulations were carried out with a structural analysis package of ANSYS. An orthotropic thermal expansion was induced in the jellyroll to illustrate the Li-ion intercalation swelling because the swelling due to diffusion is not directly available in the analysis package of ANSYS. The constitutive equation of the mechanical (elastic) strain with thermal strain and diffusion induced strain can be expressed as follows [14]

$$\varepsilon_{ij} = \frac{1}{E}\left((1+\upsilon)\sigma_{ij} - \upsilon\sigma_{kk}\delta_{ij}\right) + \frac{1}{3}\Omega\Delta c\delta_{ij}, \tag{21}$$

$$\varepsilon_{ij} = \frac{1}{E}\left((1+\upsilon)\sigma_{ij} - \upsilon\sigma_{kk}\delta_{ij}\right) + \alpha_{ij}\Delta T\delta_{ij}\,, \tag{22}$$

where ε, E, υ, σ, and δ denote the strain, the modulus of elasticity, Poisson's ratio, the stress, and the Kronecker delta respectively. The coefficient of thermal expansion and the temperature variation from the reference value are denoted by α and ΔT. Ω and Δc are partial molar volume representing volume expansion caused by concentration of solute atoms, and the concentration variation of diffusion species from the reference value.

Equations (11) and (12) show that the intercalation-induced strain/stress has an analogy to an anisotropic thermal strain/stress. Stresses caused by diffusion of solute atoms lead to a stress-strain relation similar to that due to temperature gradients. Also, the coefficient $\Omega/3$ in Eq. (11) plays a role similar to the coefficient of thermal expansion in the analysis of thermal stress [86,87]. This analogy suggests that computational solvers designed for modeling thermal expansion can be used for analyzing Li-ion intercalation expansion. This approach was used already to estimate the stress and strain due to Li-ion intercalation in graphite electrodes [77,88]. Consider a Li-ion intercalation swelling in the *z* direction. An equivalent thermal expansion can be defined in the *z* direction while a small value of 0.01 of Poisson's ratio can be used to minimize the relative expansion in the *x* and *y* directions due to the swelling in the *z* direction. This approach accounts for the orthotropic expansion of Li-ion intercalation in a direction perpendicular to the electrodes.

Estimating an equivalent modulus of elasticity to be used in the 3-D model for the jellyroll is more complex. Consider a battery cell constrained with no preload between two rigid walls (plates) via spacers (as shown in Figure 7). A force *F* is generated on the constraining walls when the active material inside the battery cell swells. For a large stiffness of the spacer and of the case, the deformations of the spacer and the case are negligible because they are contacting the fixed walls. Hence, the case and the spacer do not contribute significantly to the force *F*. The active material is the component which contributes to *F*.

Now consider the swelling of the active material when it is completely free, unconstrained by the case, spacers or walls. For the same electrochemical and thermal states, the swelling of the active material is s_a^f (as depicted in Figure 2). The ratio between *F* and *h* is an equivalent stiffness of the active material $k_{a_{eq}}$. This value is proportional to the modulus of elasticity $E_{a_{eq}}$ of the active material. This modulus of elasticity depends on the SOC because $k_{a_{eq}}$ depends on the SOC.

The coefficient of proportionality between the modulus and the equivalent stiffness in the 3-D model has to be the same as in the 1-D model. Thus, when one can use an arbitrary (non-zero, non-infinite) modulus of elasticity E_{ANSYS} in the 3-D model in ANSYS, consider a swelling of the material and calculate an equivalent stiffness k_{ANSYS}. Then, the ration $r = \frac{E_{ANSYS}}{k_{ANSYS}}$ does not depend on the arbitrary selection of E_{ANSYS}. The value *r* is a constant characteristic of the 3-D shape of the battery cell. It does not depend on the SOC and is easily determined by a single ANSYS static calculation of constrained swelling modeled as orthotropic thermal expansion and a small value of Poisson's ratio as discussed above.

Since the ratio *r* is the same in the 3-D and 1-D models, one obtains

$$\frac{E_{a_{eq}}(SOC)}{k_{a_{eq}}(SOC)} = \frac{E_{ANSYS}}{k_{ANSYS}} = r\,. \tag{23}$$

The value of $k_{a_{eq}}$ in Eq. (13) is available from the 1-D model obtained through measurements. Specifically, Eq. (5) from the 1-D model provides the value of *F* for a constrained swelling with zero pre-stress (and hence an approximately zero deformation of the case and spacer, $s_c^c = 0$) as

$$F = k_{a_1} s_a^f + k_{a_2}\left(s_a^f\right)^3, \text{ and hence } \; k_{a_{eq}} = \frac{F}{s_a^f} = k_{a_1} + k_{a_2}\left(s_a^f\right)^2, \tag{14}$$

where k_{a_1} and k_{a_2} depend on the SOC as discussed in section 3. Next, one obtains the equivalent modulus of elasticity of the active material using Eq. (14) into Eq. (13) as follows

$$E_{a_{eq}}(SOC) = r\; k_{a_{eq}}(SOC) = r\left[k_{a_1}(SOC) + k_{a_2}\left(s_a^f(SOC)\right)^2\right]. \tag{24}$$

Figure 23 illustrates the evolution of equivalent modulus of elasticity over SOC. The solid, dashed, and dotted lines denote the equivalent modulus of elasticity for the jellyroll $E_{a_{eq}}$, its linear part (due to k_{a_1}), and its nonlinear part (due to k_{a_2}). These results show that the linear term is constant in the low and high SOC regions. As expected, the linear term changes around 0.5 SOC due to phase transition, and the nonlinear term monotonically increases over SOC. These observations are a direct consequence of the results in Figure 5 (b). The nonlinear term contributes over 20% of the total modulus of elasticity at the fully charged state, suggesting that it is not negligible. The equivalent modulus of elasticity for the jellyroll $E_{a_{eq}}$ also varies nonlinearly over SOC and shows a sudden change due to phase transition. However, the estimated equivalent modulus of elasticity for the jellyroll is much smaller than that of other battery components such as a cathode, an anode, and even a separator [90],[91]. These results could be explained by the combined effect of the separator and electrolyte.

Hundreds of ultra-thin film electrodes are stacked in the jellyroll. The lowest stiffness of all these layers influences the most the equivalent stiffness of the entire system (like in a series connection of springs). Hence, the stiffness of the separator might be dominant. Moreover, electrolyte fills the pores of the separator. Hence, the stiffness (and hence the equivalent modulus) of the separator can be represented as a combination of two spring elements (separator, electrolyte) connected in series for some regions and in parallel for other regions. Consequently, the equivalent modulus of elasticity for the cell can be of the order of one MPa because the modulus of the electrolyte is around 1 MPa [14],[60], while that of the separator is of the order of hundreds of MPa [89]. However, the exact physical origin of the measured values is still not completely clear and further investigations are needed to elucidate the physical basis for the observed values.

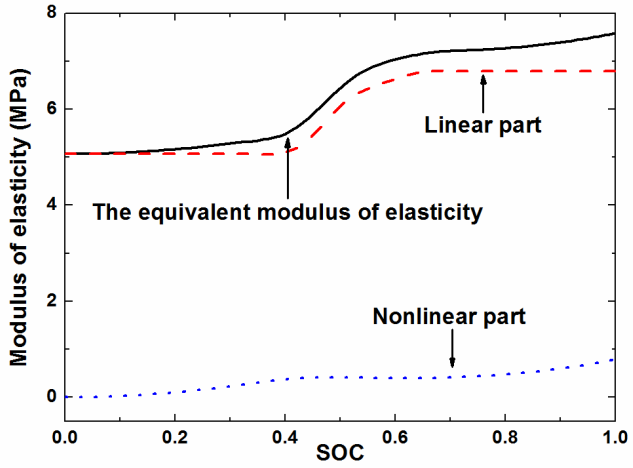

Figure 23. (Color online) The evolution of the equivalent modulus of elasticity for the jellyroll over SOC.

4.5.3 Model validation

The measured 2-D swelling shape on the surface of the battery cell at the fully charged state (the third experiment in section 2) is shown in Figure 24 (a). The swelling is almost flat in the central area because of the flat wound jellyroll in that area and because Li-ion intercalation is uniform in the *xy* plane (the plane of the surface of the battery). In contrast, the swelling near the sides varies and is relatively small due to constraints from the case and due to the empty space inside the case, as shown in the X-ray tomography [56]. Relatively large expansion is observed at the bottom right side on the surface. That can be caused by the bus bars and the clamps which are inside the case and bind the jellyroll at its left side (also

visible in the X-ray tomography). As described in detail in Ref. [42], the complex shape of the jellyroll and the empty space inside the case result in asymmetric swelling at the edges. However, the effects of these complex components are not extending in the center of the cell where swelling is uniform. Therefore, the best locations for monitoring free swelling with just few sensors are in the center region.

Figure 24 (b) shows the free swelling shape on the surface of the battery case from the 3-D phenomenological model at the fully charged state (1.0 SOC). The contour plot uses the same contour line values as those in Figure 24 (a) for easy comparison. In simulation, the orthogonal expansion in a direction perpendicular to the electrode is induced to match the magnitude of the swelling at the center of the surface (labeled as point 13 in Figure 16). Then, the model predictions are compared with measurements of swelling at other locations. The overall swelling shape and the magnitude of swelling are similar to experiments, except for the effect of the unmodeled clamps and bus bars.

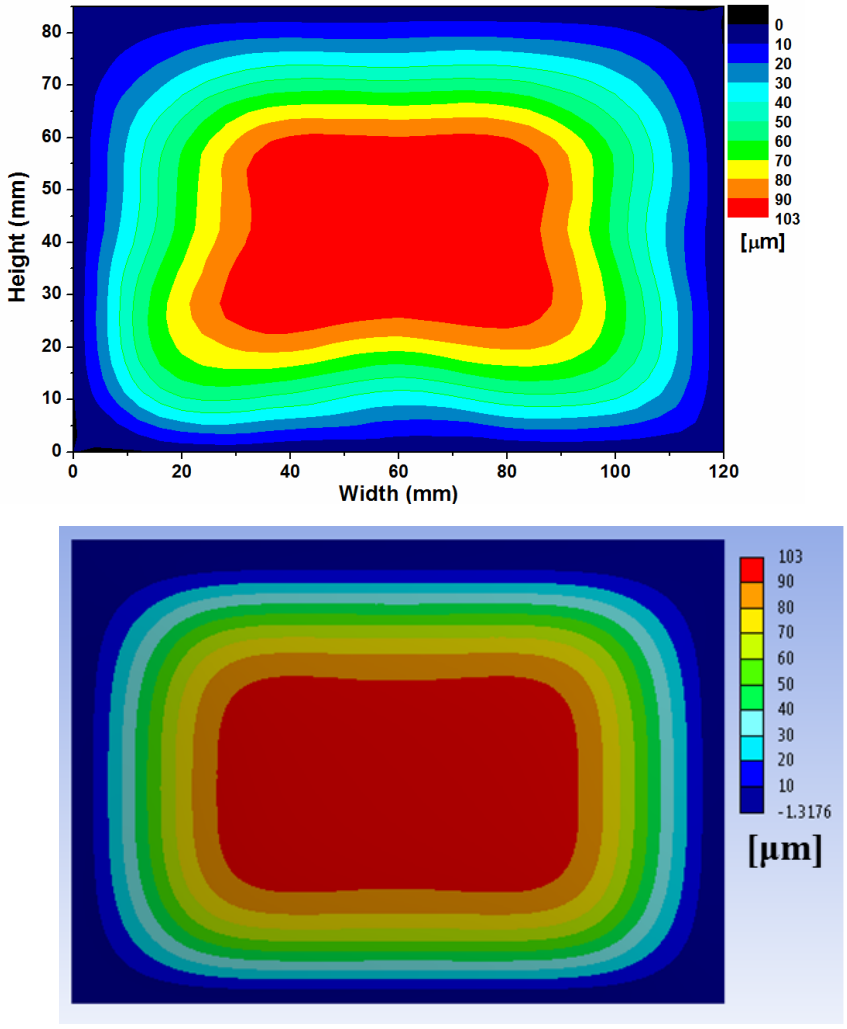

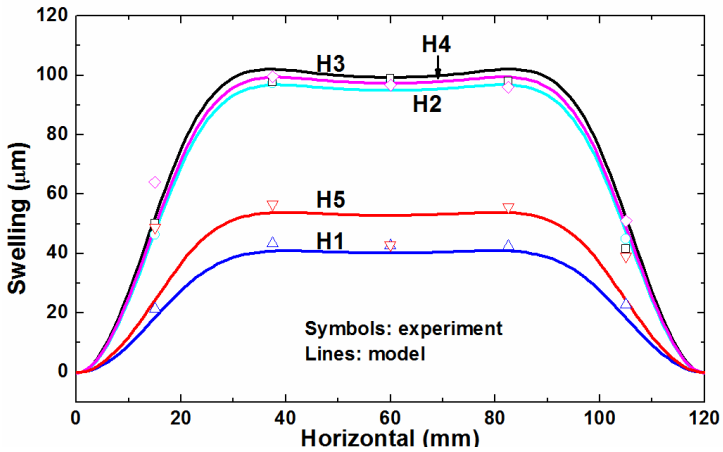

Figure 24. (Color online) Swelling shape on the surface of the battery cell due to Li-ion intercalation at fully charge state (1.0 SOC); (a) measurements; (b) model predictions, and (c) comparison between the 3-D phenomenological model (solid lines) and measurement (symbols) along the horizontal lines H1to H5 (locations of the horizontal lines are provided in Figure 1).

Figure 24 (c) shows the swelling along horizontal lines H1 to H5 labeled in Figure 16. Solid lines show estimated swelling from the 3-D model, while symbols show measured swelling at the fully charged state. The model prediction at the center region (H2 to H4) is in great agreement with measured data because the effects of the complex components around the edges of the active material are relatively small in the center region as aforementioned. The swelling at the top side (H1) is also consistent with the experiments. However, the bottom side (H5) shows differences between the model and the measured data. This might be the effect of the asymmetrically located clamps and bus bars as aforementioned. The comparison between model prediction and experiments suggests that the assumptions made in constructing the model are reasonable, namely the wound shape of the jellyroll does not contribute significantly to the swelling shape of the case (due to empty spaces), and the bus bars and clamps do not need to be modeled for evaluating the shape of swelling, especially in the center regions.

Figure 25 illustrates the quasi-static free swelling at a variety of SOC (the second experiment). Three horizontal lines (labeled as H2, H3, and H4 in Figure 16) show the model predictions, whereas symbols show measured data. Solid, dashed, and dotted lines denote free swelling at 0.9, 0.5, and 0.3 SOC respectively. The swelling shape predicted by the 3-D model is consistent with the measurements, suggesting that the orthotropic expansion model of the Li-ion intercalation swelling and the identified modulus of elasticity of the jellyroll are accurate. The free swelling predictions at other SOCs also are consistent with the measurements. Those results are omitted here for the sake of brevity. Simulations with the 3-

D swelling model demonstrate that the proposed model is able to accurately predict the overall swelling shape on the surface of the cell.

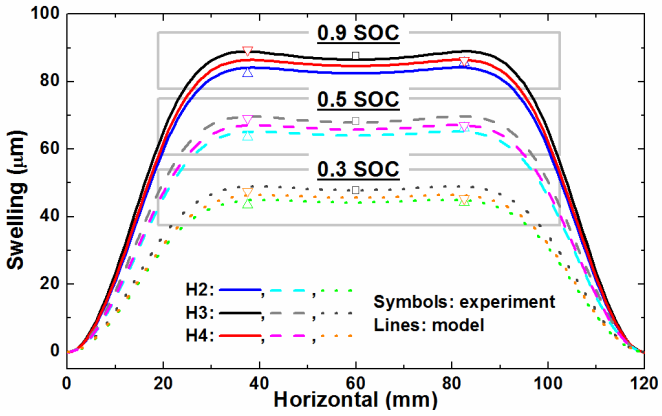

Figure 25. (Color online) The comparison of free swelling at a variety of SOC between the 3-D model (solid, dashed, and dotted lines) and measured data (symbols).

4.5.4 Simulation at pack conditions

The proposed 3-D model for one battery cell is useful in several ways. For example, this model can be used to construct the model of a battery pack. Then, the force created in the pack by Li-ion intercalation can be estimated while also accounting for preload effects. Based on the battery cell or pack model, optimal sensor locations and the optimal number of sensors needed can be determined during design.

Another related example is related to predicting the constrained swelling shape on the surface of the battery cells in pack conditions at the fully charged state. This shape is shown in Figure 26. Relatively large swelling can be observed in the center region between the areas of contact with the spacer. This result suggests that geometric constraints on the cell swelling due to spacers are important in pack conditions. Moreover, the pattern of swelling is repetitive and the amount of swelling (especially in the areas where there is no contact with the spacers) is the same in the center region, which is the area of contact between the jellyroll and the casing. Therefore, an appropriate location for placing the displacement or strain sensor in pack condition is the center region, in an area without contact with the spacer.

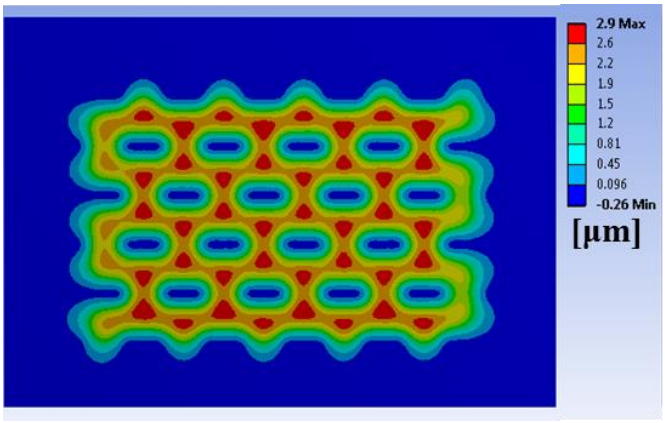

Figure 26. (Color online) Constrained swelling on the surface at the fully charged state (1.0 SOC).

Figure 27 shows the swelling predicted by the model over SOC in the center region, at a location where there is no contact with the spacer. The overall shape of expansion versus SOC is similar to the shape of the free swelling, indicating that innate characteristics of Li-ion intercalation swelling are observable also in constrained conditions. However, this swelling is an order of magnitude smaller, suggesting that high precision displacement or strain sensors are needed to use this information for estimating the SOC or the state of health (SOH).

The force due to Li-ion intercalation swelling in pack conditions was simulated (Figure 28). The main purpose of this simulation is to estimate the reaction force as a function of SOC between the spacer and the exterior walls, and comparing the estimated force from the 3-D model to that from the 1-D force model. The force from the 1-D model was estimated from Eq. (16) assuming that the initial displacement is zero. Hence, these simulation conditions correspond to the force due to Li-ion intercalation swelling without preload. This force also can be estimated from the finite element 3-D model. The variation of the jellyroll swelling due to the Li-ion intercalation (Figure 25) and its equivalent modulus of elasticity (Figure 23) over SOC were used as input parameters ranging from 0% to 100% SOC, with 10% increments. The reaction force between the spacers and the exterior walls was calculated with the 3-D model (Figure 22). Two half spacers as well as the case and the jellyroll are used in these simulations.

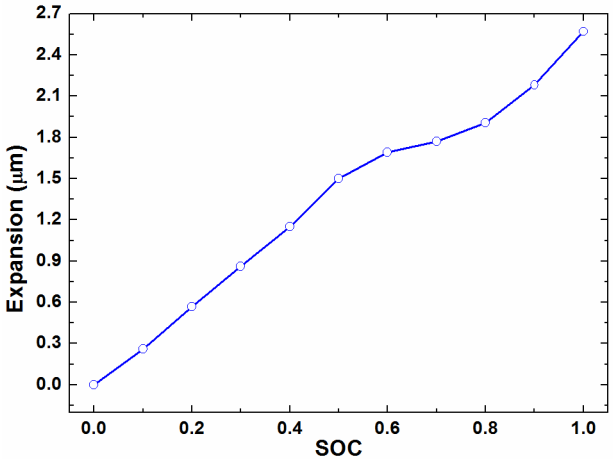

Figure 27. (Color online) Constrained swelling over SOC in the center region, at a location where there is no contact with the spacer.

Figure 28 shows the reaction forces calculated from the 1-D force model and the 3-D model. The solid line is the force from the 1-D model, whereas the circle symbols are the force from the 3-D model. The forces from the 1-D model are consistent with the forces from the 3-D model. The maximum difference is 13N and the root-mean-square (RMS) difference is 8N. These results corroborate the hypothesis that the force can be modeled with the nonlinear spring element reflecting the dependency on the magnitude of swelling (Eq. (16)), and the equivalent stiffness can be converted to an equivalent modulus of elasticity (Eq. (18)).

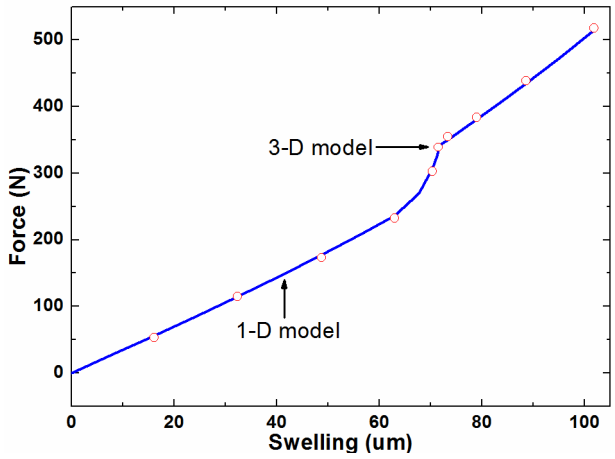

Figure 28. (Color online) Comparison of force between the 1-D and the 3-D phenomenological models for a single battery cell without preload.

4.6. Conclusions

The mechanical properties, of either stack stress, strain, or a combination thereof, can provide real-time estimation of SOH or SOC and ultimately prolong the lifespan of the battery, not only of the cells but also of the packs. For these purposes, three phenomenological models are proposed based on the measured force and free swelling to depict the Li-ion intercalation behaviors. The 1-D models addresses the equivalent 1^{st} order relaxation or the nonlinear stiffness representing the force dependency on the magnitude of swelling, and thereby enables the proposed models to capture the transient swelling during the rest periods or steady-state force. The 3-D finite element model introduces the orthotropic expansion of the jellyroll and the equivalent modulus of elasticity to predict the swelling shape of the battery cell over SOC.

CHAPTER V
Characterization and modeling of the thermal mechanics of lithium-ion battery cells

5.1. Motivation and background

Modern societies and industries consume huge amounts of energy obtained from the chemical energy stored in fossil fuels. Fossil fuels can still be extracted over the world and used as main power sources for a variety of applications from (relatively) small-scale internal combustion engines for transportations to massive-scale gas turbines for energy conversion systems. For instant, transportation typically covers 30-35% of the total fuel consumption of most industrialized countries [93]. Moreover, 95% of private transport depends on oil, which accounts for over 50% of the oil consumed worldwide [94].

The high consumption of fossil fuel resources causes serious problems. The combustion of fossil fuels emits large amounts of greenhouse gases, pollutants, and thereby is responsible for global warming. Therefore, a consumption of fossil fuels creates other environmental costs and this societal cost can no longer be negligible. To shift towards a low-carbon world, mitigation efforts must occur across all countries from developing countries to industrialized countries; decarbonizing the energy supplies of industrialized countries, and shifting developing countries onto a low-carbon development path.

There are two promising solutions to mitigate the effect of environmental pollutions and additional environmental costs from fossil fuel consumptions: 1) the electrification of vehicles to enhance the efficiency of energy consumption in transportation and 2) cultivating renewable farms such as wind farms and solar farms to provide clean and eco-friend energy without the emission of greenhouse gases and pollutants. However, several technological

bottlenecks limit the viability and commercialization of two promising solutions. Vehicle electrification such as electric vehicles (EVs) and hybrid electric vehicles (HEVs) needs alternative energy sources, which feature high energy/power capability, high efficiency, and a long lifetime. Energy produced from renewable farms has stochastic characteristics due to the inherent intermittency of wind and solar energy sources and thereby it makes overall power systems and grids unstable.

Energy storage systems are an excellent way to break through barriers both solutions face. Especially, electrochemical energy storage systems are a convenient and efficient way to store the electrical energy in the form of chemical energy. These advantages have led many researchers to devote themselves to focus on developing new and innovative electrochemical energy storage systems. Among various types of electrochemical energy storage systems on the market, lithium-ion batteries (LIBs) are the most promising in the sense that LIBs feature no memory effect, low self-discharge rate, broad temperature range of operation, high power/energy density, and long cycle life [26-28].

However, high and extra cost for energy storage systems still limits its applications. Especially, the cost of battery packs is a key barrier to the commercial viability of vehicle electrification, even though vehicle electrification with the advent of LIBs improves fuel efficiency. Therefore, the power improvement of battery packs with high charge/discharge levels is needed for practical uses such as quick acceleration, although the total capacity of battery cells and packs should be minimized and lifetime of battery packs should be prolonged to reduce the cost. These harsh operational conditions play a critical role to generate a large amount of heat, and thereby increase the temperature of battery cells and packs while in use. Such excessive heat generation and uneven temperature distribution not only reduce the efficiency of battery packs but also accelerate the degradation of battery life [95]. Moreover, overheating, combustion, or even explosion can occur with the increase of thermal energy contained in the battery cells and packs [96].

A wide operational range that battery packs encounter and unpredictable pattern of thermal loads imposed also further complicate thermal issues. For example, a restricted range between 20 ℃ and 40 ℃ has been reported for optimal performance and lifespan of LIBs [97], even though the tolerable operational range should be between -10 ℃ to 50 ℃ considering the stressful and harsh environmental conditions of transportation [98].

To sum up, battery thermal management is of great importance. Therefore, considerable efforts have been devoted not only to obtain a fundamental understanding of dynamic thermal mechanics but also to seek innovative and practical solutions [1,99]. Numerical simulations with computational fluid dynamics (CFD) methods and finite element methods (FEM) have been conducted to predict thermal dynamics of Li-ion battery cells and packs [2,31,85]. A variety of heat transfer models have been created and validated through experiments [32-35]. Several lumped parametric thermal models have also been proposed for the control purposes with the advanced power management schemes in next-generation battery management systems (BMS) [43,44,62].

In particular, recent research pays attention to thermal expansion of host materials and cells in the sense that the volume change of cells from temperature variation is similar in order of magnitude with the volume change of cells from Li-ion intercalation [40,42]. Therefore, periodic thermal stress and strain significantly affect not only the performance of individually battery cells but also the efficiency of whole battery packs, and the eventual fatigue life of cells and packs. However, the investigation of thermal expansion on the cell-level is still few, making it difficult to estimate the thermal stress and strain originated from temperature variation. Moreover, the modeling of the thermal expansion has not been investigated in great detail, although characterizing the thermal expansion has become important to prolong the lifespan of LIBs.

In this paper, we report experimental characterizations and a numerical three-dimensional thermal swelling model of Li-ion cells. High-precision displacement sensors were used to measure the cell-level swelling on the surface arising from temperature elevation of an unconstrained graphite/nickel-manganese-cobalt-oxide (NMC) cell whose temperature was regulated in a thermal chamber. The swelling shape from temperature variation was found to be different than that from Li-ion intercalation. This difference might be due to non-uniform temperature distribution of the jellyroll and the generation of gaps and voids between electrodes. To capture this thermal mechanics of Li-ion cells, several important and critical parameters are estimated from experiments. The proposed model was verified by comparisons with experiments at different heat generations. The comparison shows that the proposed model accurately predicts dynamic behavior of Li-ion cells due to thermal loads. The solutions at a constrained condition showed that non-uniform temperature distribution of the jellyroll still played a critical role for the thermal swelling shape at the pack condition, even though the gaps and voids did not occur because of the constraint from the spacer.

Further, high core temperature was found to increase the magnitude of thermal swelling, suggesting that the prediction of the core temperature is important to predict dynamic thermal mechanics for the use in power management schemes. The reaction force easily captures this thermal dynamic behavior, whereas the amount of swelling is so small that it is hard to measure, suggesting that the force originated from the volume change of cell can become a sensitive gauge for characterizing operational state. Such an accurate model, able to estimate cell thermal behavior, may be beneficial to the design of LIBs, development of stress or strain sensor, optimum sensor placement, and thermal management of not only single cells but also battery packs.

5.2. Experiments

This study used a flat-wound type prismatic 5Ah Li-ion cell obtained from a Ford Fusion HEV battery pack. Detailed information of the Li-ion cell is available in Ref. [42].

The free swelling of the cell was measured with high-precision contact-type displacement sensors with 1μm accuracy and 0.1μm resolution (Keyence GT2-H12KL, Japan). The sensor head creates a contact force on the battery surface of less than 0.3N. The sensor measured a variety of locations on the battery surface with a fixture (Figure 8). The fixture was made from aluminum opposite to our previous work [42,78]. In the previous work, measured data included the thermal hysteresis of the ABS plastic fixture and thereby measurement should be calibrated to eliminate the effect of thermal hysteresis when ambient temperature is changed. Hence, a new fixture made from the aluminum was prepared to mitigate the effect of thermal hysteresis of the fixture to enhance the accuracy of experiment in that aluminum is known as a non-thermal hysteresis material.

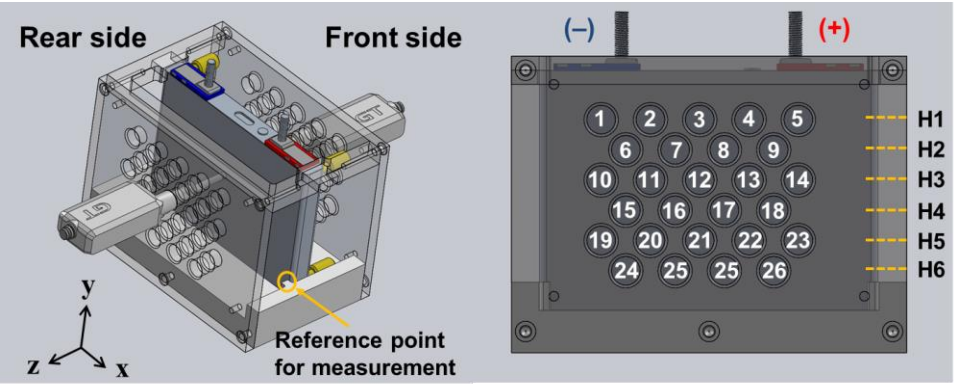

Figure 29. (Color online) Schematic diagram of the experimental setup showing the fixture, the cell, and the sensor locations 1-26.

The prismatic cell was constrained at its eight corners with dimples at the rear side, whereas it was constrained with an aluminum spring pusher at the front side in the fixture, but was otherwise unconstrained (Figure 8). The fixture was placed inside a thermal chamber (ESPEC BTZ-133, Japan) with a controlled desired temperature. Three thermocouples were also placed. One thermocouple was installed on the center of the cell to measure cell surface temperature in a location that avoided interference with the displacement sensors. Another thermocouple was installed on the fixture to measure the temperature variation of the fixture transferred from the battery through contacts. The third thermocouple was installed between the fixture and the cell to measure near-surface ambient temperature.

A preliminary test was conducted to check the repeatability and thermal hysteresis as well as the isotropic expansion of the aluminum fixture. An aluminum block, which has the same size as the battery cell, was installed instead of the cell because thermal expansion of aluminum is available. The temperature of the thermal chamber was regulated at 25℃ at first. Then, the temperature was changed to 5℃ and incrementally changed to 45℃ with 10℃ increments and then returned to 25℃. Each temperature variation was followed by 2 hours of rest time to ensure thermal equilibrium. Relative thermal expansion in the z direction was measured at three locations labeled 5, 12, and 23 in Figure 8 for each side.

Pulse excitation experiments were carried out to characterize the thermal swelling shape of the battery cell from temperature elevation. The battery was fully charged using standard CCCV protocol prior to discharge. Then, the battery was discharged with a 2A (0.4C) current for 1.25 hour to obtain a 50% SOC. Pulse current was induced to the battery cell with a two-second period (1 second charge and 1 second discharge) for two hours to obtain quasi-static pure thermal expansion. Note that the shorter charge/discharge period is better to obtain pure

thermal swelling in that a long charge/discharge period changes the state of charge (SOC) and thereby causes the volume change due to Li-ion intercalation. Three-hour relaxation periods were followed by pulse excitation. This procedure was repeated three times to check the repeatability. Two currents, 50A and 75A, were used for pulse excitations to identify the thermal swelling shape at different temperature elevations. The entire experiment was repeated with a changing sensor location labeled in 1 to 27 at the rear side in Figure 8. One sensor was installed the center of the other side labeled 16 in Figure 8 as a reference.

5.3. Description of thermal swelling model

A representation of the prismatic cell geometry used in Ford Fusion HEV was created to simulate the thermal mechanics of the battery cell by using detailed information of the casing and jellyroll configurations, which were obtained from the X-ray tomography and dissection. Basic configuration and geometry are the same to Li-ion intercalation swelling model proposed in chapter IV.

Briefly, the jellyroll (the yellow domain in Figure 30) was modelled as a cuboid because the noncontact wound shape of the jellyroll does not contribute to the expansion of the aluminum case. A 100μm micro-gap was generated in the top and bottom sides of the jellyroll to distinguish the contact region (the purple domain in Figure 30) from the noncontact region of the jellyroll with the case (inset figure in Figure 30). The aluminum case was modeled with measured dimensions. The half of plastic spacer made from polybutylene terephthalate (PBT) was also modeled with measured dimensions in that several battery cells and the spacers are connected in series in the battery pack of the Ford Fusion HEV, and thereby it is presumably equal to the combination of two half spacers and one battery cell. All components were modeled as a homogeneous solid medium.

The simulations were carried out with a structural analysis package of ANSYS. A model with the jellyroll and case can simulate the swelling of the battery cell at an unconstrained condition and compare with the measured swelling shape for model validation. A model with the jellyroll, case, and spacer can simulate the response of the battery cell at a constrained condition of the battery pack.

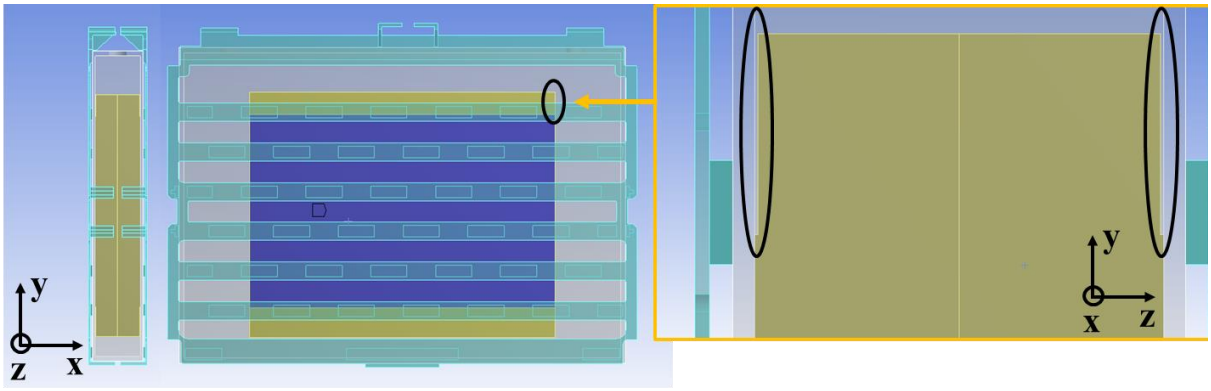

Figure 30. (Color online) The geometry of the prismatic battery cell used for the Ford Fusion HEV. The yellow, transparent white, and transparent blue domain represent the jellyroll, the aluminum case, and the half of the spacer respectively. The purple domain represents the contact region between the jellyroll and the case. The inset figure shows the micro-gap in the top and bottom sides of the jellyroll.

This model has two key differences than the model of Li-ion intercalation swelling in that experiments show that the swelling shape from temperature elevation is different than that from electrochemical reaction, i.e. Li-ion intercalation (details for experimental results are showed in the section of results and discussion). The swelling shape from temperature elevation is convex and elliptical, whereas Li-ion intercalation swelling is more flat in the central area. This different shape might be caused from two reasons: non-uniform temperature distribution of the jellyroll [85], and the generation of micro gaps and voids between electrodes [6]. These hypotheses suggest implementing these two phenomena into the thermal swelling model.

To account for two features under the thermal swelling, the coupled thermal-structural analysis was carried out. Thermal analysis was carried out first with a constant heat generation of the jellyroll to estimate non-uniform temperature distribution and thermal gradient on the cell. This result was fed into the structural analysis to estimate thermal swelling.

The jellyroll generates the heat energy during operation due to entropy change and Joule heat [38]. Entropy compensates the residual energy in the energy conversion process between the enthalpy and the Gibbs free energy, while Joule heat is due to the internal resistance of the cell components. The exact amount of heat generated in the jellyroll was estimated from the coupled electro-thermal model [61]. The estimated heat generations were 5.8e4 Wm^{-3} and 12.5e4 Wm^{-3} for 50A (10C) and 75A (15C) pulse excitation cases. This estimated heat was imposed to the jellyroll in the simulation. The heat convention was also imposed to the

surface of the outer case to illustrate the air cooling in the thermal chamber. The heat transfer coefficient (or film coefficient) *h* was estimated to match the measured temperature on the center of the case. The estimated values were 58 $Wm^{-2}K^{-1}$ and 60.5 $Wm^{-2}K^{-1}$ for each case. Note that the thermal chamber regulates not heat flow but temperature; higher heat flow is needed for larger heat generation to maintain constant temperature.

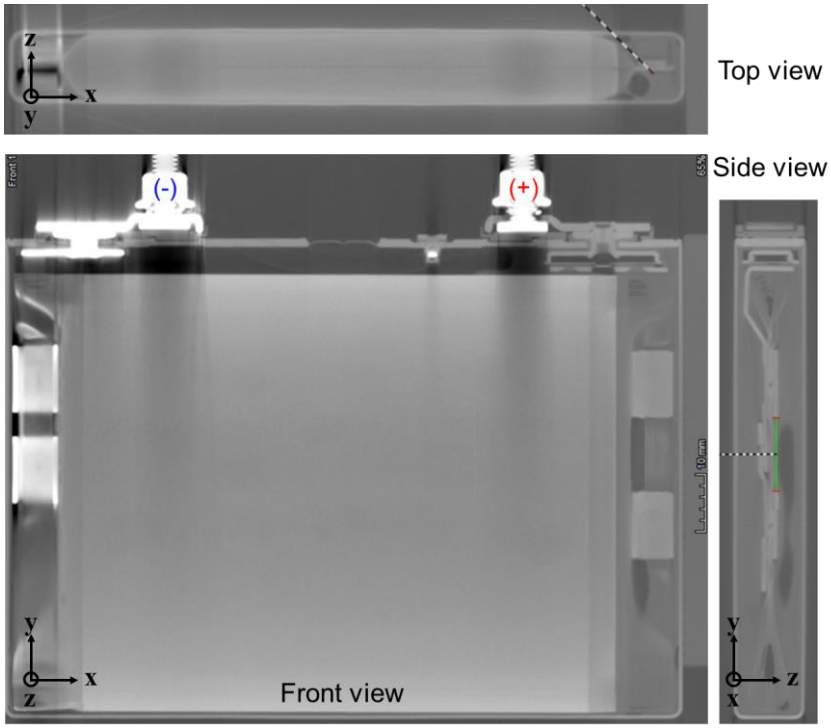

Figure 31. (Color online) X-ray tomography of the battery cell. The white domain inside of aluminum case is wound prismatic jellyroll. The jellyroll is connected with positive and negative current collectors at the left and right sides.

To account for the creation of micro gaps and voids, the jellyroll is separated into two pieces (Figure 30). The generation of micro gaps and voids might be due to combined effect of mechanical constraints and the isotropic expansion of each material. The jellyroll cannot create any void and gap at the edge because the top and bottom sides are wound and left and right sides are clamped with current collect and bus bars (Figure 31). In contrast, there is no glue or bonding materials between the electrode surfaces and thereby gaps and voids occur easily in the central region. To account for these features, appropriate contact conditions were imposed to the two pieces of the jellyroll. Bonded contact was assigned to the four edges (top, bottom, left, and right edge) because the wound shape at the top and bottom sides and clamping with current collectors and bus bars at the left and right sides did not allow the separation between electrodes at the edges. In contrast, separation between the separated

jellyroll was allowed on the contacted surface in that no constraint is actually imposed between the stacked electrode layers in the central area.

No separation with the slip was assigned between the jellyroll and the case, between the case and the plastic spacer, and between the spacer and the exterior walls for realistic simulation considering the assembled conditions of the battery cells and packs. Since relatively large deflections were applied, geometric non-linearity was considered, i.e. the coordinates of the element nodes were updated during the loading steps with respect to the current deformations.

5.4. Estimation of parameters

5.4.1 Structural properties

Microstructure transformation of electrodes leads to the evolution of material properties due to the phase transition [52,53]. Especially, the layered structure such as graphite intercalation compounds shows significant change of material properties, whereas the spinel and olivine structures such as $LiMn_2O_4$ and $LiFePO_4$ minimally vary upon lithiation [101]. Our previous work also shows the lithiation induced stiffening of the equivalent stiffness (and the modulus of elasticity) of the jellyroll over SOC. The estimated modulus of elasticity for 0.5SOC, 6.5MPa, from chapter IV was imposed to the jellyroll in that pulse excitation was carried out at 0.5 SOC. The Poisson's ratio (ν) for the jellyroll was selected to 0.3 in that the averaged Poisson's ratio is around 0.3 for all of the electrode materials, and this does not significantly change with Li concentration [101]. Moreover, Poisson's ratio for a separator and electrolyte is 0.35 and 0.25 [102], suggesting that the equivalent Poisson's ratio of the jellyroll is presumably similar to 0.3. The modulus of elasticity and Poisson's ratio imposed on the aluminum case were 68GPa and 0.33; the ANSYS material database provided property values for a variety of materials such as steel and aluminum taken from a variety of sources [103,104]. The modulus of elasticity and Poisson's ratio imposed on the PBT spacer was 3.6GPa and 0.44; the modulus of elasticity was measured from a nanoindentation testing; Poisson's ratio was available in [105]. Limited by the availability of the data and understanding on the thermal characteristics of structural properties for electrode materials, structural properties were assumed to be constant in terms of temperature in the operational range of battery cells and packs at this stage of the work.

5.4.2 The equivalent coefficient of thermal expansion

There are two issues in the estimation of the equivalent coefficient of the thermal expansion for the jellyroll: (1) isotropic or orthotropic and (2) temperature dependency.

Thermal expansion in a through-plane direction (*z* direction in Figure 31) is different than that in an in-plane direction even if each component of the jellyroll has isotropic thermal expansion characteristics. Cathodes, anodes, and separators are stacked in series for the through-plane direction, denoting that total expansion is the sum of expansion of each electrode. On the other hand, electrodes and separators are connected in parallel for the in-plane direction and thereby the electrode, which has the largest coefficient of thermal expansion, plays a critical role in the total thermal expansion. Anisotropic thermal expansion of polyethylene and polypropylene, which is the main material for separators, further complicates estimating the equivalent coefficient of thermal expansion [50,106].

To estimate the equivalent coefficient of thermal expansion of the jellyroll for the through-plane direction (α_{thro}), quasi-static thermal swelling measured on the center of the battery cell (labeled 3 in Figure 1 of Ref. [78]) ranging from 25℃ to 45℃ was compared with simulation results. To impose the exact experimental condition on the simulation, uniform temperature elevation was imposed to the jellyroll and case from 25℃ to 45℃ with a 5℃ increment. Based on this uniform temperature elevation, static structural analysis was carried out with the jellyroll and case. The equivalent coefficient of thermal expansion of the jellyroll for the through-plane (α_{thro}) was calibrated to match the experiment (Figure 32). The estimated equivalent coefficient of thermal expansion for the through-plane direction not only is similar in order of magnitude with that for polyethylene and polypropylene, but also shows temperature dependency, which is also the characteristic of polymer materials [54]. This observation suggests that separators play a critical role in thermal mechanics of the battery cell.

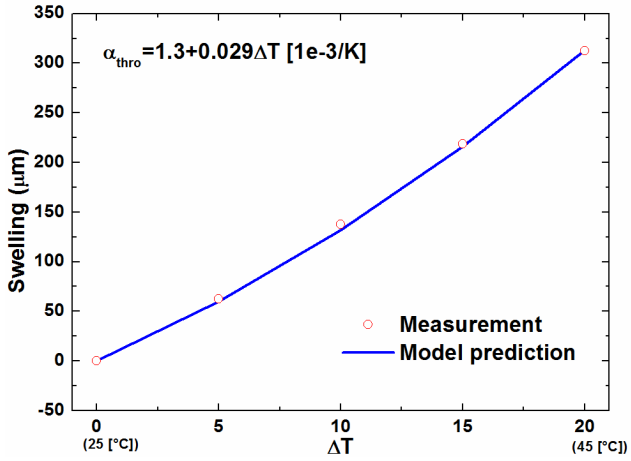

Figure 32. (Color online) Quasi-static thermal swelling on the center of the battery cell; the symbol is measurement, while line is ANSYS result.

To estimate the equivalent coefficient of thermal expansion for the in-plane (α_{in}) and evaluate the effect of through-plane thermal expansion from in-plane thermal expansion, four cases were tested in this study: (0, 0, 1.3), (0, 1.3, 1.3), (1.3, 0, 1.3), and (1.3, 1.3, 1.3) where (α_x, α_y, α_z) [1e-3K^{-1}] in Figure 8. Simulation shows that swelling shape is almost the same for all cases; maximum difference for *z* direction is below the 2μm, which is below the repeatability of measurement (details for repeatability are shown in the next section). This small difference suggests that the effect of in-plane thermal expansion for through-plane thermal expansion is negligible because no constraint is imposed on the jellyroll in *x* and *y* directions for the proposed thermal swelling model. In summary, the equivalent coefficient of thermal expansion for the through-plane is only important in the configuration of the proposed thermal swelling model and it was calibrated from the experiment.

The coefficient of thermal expansion for aluminum and PBT was set to 2.3e-5K^{-1} and 4.1e-5K^{-1}. The coefficient of thermal expansion for aluminum was provided by the ANSYS database and that for PBT was obtained from the datasheet, which was provided by the manufacturer. The case and spacer were assumed to isotopically expand.

5.4.3 Thermal conductivity

Similar to the equivalent coefficient of thermal expansion, thermal conductivity depends on the direction of heat flow [107]. In other words, the heat transfer is anisotropic because the current-collector layers within the jellyroll have much higher thermal diffusivity than the separator. Therefore, the equivalent thermal conductivity for the in-plane direction ($k_{eq_{in}}$) is

higher than that for the through-plane direction ($k_{eq_{thro}}$). Theoretically, the equivalent thermal conductivity for the in-plane direction is calculated by using Eq. (12) because cathodes, anodes, and separators are stacked in parallels.

$$k_{eq_{in}} \sum t_i = \sum k_i t_i, \tag{25}$$

where k_i, and t_i denote the thermal conductivity of each material, and the thickness of each material. The equivalent thermal conductivity for the through-plane direction is expressed as Eq. (26) in that electrodes and separators are stacked in series.

$$\frac{\sum t_i}{k_{eq_{thro}}} = \sum \frac{t_i}{k_i}, \tag{26}$$

These equations clearly show how anisotropic thermal conductivity should be taken into account in a macro-homogeneous thermal model of the jellyroll. It can be inferred from these equations that the material, which features the lowest thermal conductivity, governs the overall thermal characteristics, especially for the through-plane direction. Therefore, separators and electrolytes play a critical role for heat flow in the through-plane direction because the thermal conductivity for separators and electrolytes is much smaller than that for other materials [102].

The equivalent thermal conductivity for the in-plane direction, which is taken from Ref. [61], is used for that of the jellyroll; the value is 22 $Wm^{-1}k^{-1}$. The estimation of the equivalent thermal conductivity for the through-plane direction is more complicated. The jellyroll is connected in series with the case. Moreover, current collectors only exist at the left and right sides of the jellyroll, whereas all components are connected in series in the jellyroll (Figure 31), suggesting that the equivalent thermal conductivity in the left and right sides of the jellyroll is different than that in the central area.

To calculate the thermal conductivity for the each region, three stepwise calculations were conducted. First, the equivalent thermal conductivity of the jellyroll for the through-plane direction was estimated using Eq. (26) with the equivalent thermal conductivity of the cell (0.73 $Wm^{-1}K^{-1}$), which is estimated from Ref. [78]; the case and jellyroll are connected in series for *z* direction. The estimated equivalent thermal conductivity of the jellyroll for the through-plane direction is 0.65 $Wm^{-1}K^{-1}$. Second, the equivalent thermal conductivity for the central region was calibrated to match the magnitude of thermal swelling for 10C pulse experiment; it results in 0.43 $Wm^{-1}K^{-1}$. Third, the equivalent thermal conductivity for the edge region was calculated with the equivalent thermal conductivity for the jellyroll (0.65

$Wm^{-1}K^{-1}$) and the center region of jellyroll (0.43 $Wm^{-1}K^{-1}$) using Eq. (12) based on the area in *xy* plane for each region because the edge region and central region can be considered as a parallel connection in *z* direction. The estimate for the equivalent thermal conductivity for the edge region was 9.5 $Wm^{-1}K^{-1}$. The equivalent thermal conductivity for the edge region shows much higher value because separators do not exist in the edge region. Temperature dependency of the thermal conductivity is assumed to be negligible in the operational range in that measured thermal conductivities of the separator at 25℃ and 45℃ show a small difference [108]. Note again that thermal conductivity of a separator is dominant and governs the overall heat flow, especially for the through-plane direction, because it has the lowest value.

The thermal conductivity for the case and spacer was set to 149 $Wm^{-1}K^{-1}$and 0.24 $Wm^{-1}K^{-1}$. The thermal conductivity for aluminum was provided by the ANSYS database and that for PBT was available in Ref. [105]. It was assumed that temperature dependency of thermal conductivity is negligible for both materials.

5.5. Results and Discussion

5.5.1 Characterize the thermal behavior of a fixture

Figure 33 shows the measured displacement for the preliminary test with the aluminum block. Lines are measurement from the front side, while dashed lines are measurement from the rear side in Figure 8. The initial displacement at 25℃ was set to zero (the sensor measures relative displacements). Measured data from all sensors converge to zero when temperature was change to 25℃ from other temperature. Maximum difference at 25℃ is below the 1μm, which is the accuracy of the displacement sensor. Measured displacement is decreased when temperature increases. The fixture holds the sensor used to measure swelling, and hence the sensor indicates a lower value when the fixture expands. Measurement at the same face shows the same displacement, suggesting that the fixture isotopically expand for all directions.

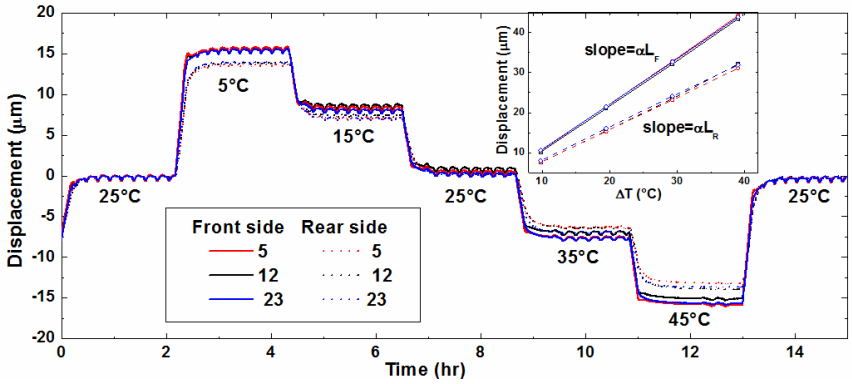

Figure 33. (Color online) Thermal expansion of the fixture due to temperature variation. Lines are measured thermal expansion labeled in 5, 12, and 23 at the front side in Figure 8, whereas dashed lines are measured thermal expansion of the fixture labeled in 5, 12, and 23 at the rear side in Figure 8.

Measurement from the front side is slightly different than that from the rear side in the fact that the measured data from the front side include the expansion of aluminum block and the length of fixture is different with respect to the reference location (Figure 8). In other words, measurement in the rear side includes two components: the expansion of the fixture and thermal characteristics of the sensor (Eq. (27)). In contrast, measurement in the front side includes three components (Eq. (28)): the expansion of the fixture, thermal characteristics of the sensor, and expansion of aluminum block because the aluminum block only thermally expands to the direction of a spring pusher.

$$\Delta L_{meaured} = -\Delta L_{fixture} + \Delta L_{sensor}, \tag{27}$$

where $\Delta L_{\text{meaured}}$, $\Delta L_{\text{fixture}}$, and ΔL_{sensor} is the measured expansion, fixture expansion, and sensor expansion. The thermal characteristic of the sensor is available in Ref. [78].

$$\Delta L_{meaured} = -\Delta L_{fixture} + \Delta L_{sensor} + \Delta L_{Al}, \tag{28}$$

where ΔL_{Al} is the thermal expansion of the aluminum block. The pure thermal expansion of the fixture for both sides was calculated by using Eqs. (27) and (28) (inset figure of Figure 33). The thermal expansion is in a linear fashion in terms of temperature same to the aluminum in the temperature range. In this inset figure, the slope is αL considering the conventional equation of thermal expansion; $\Delta L = \alpha L \Delta T$. To verify the equations and measured length of the fixture, the coefficient of thermal expansion for six locations was calculated and the estimated α was compared to that of the aluminum. The average and standard deviation are 23.8e-6K^{-1} and 0.5e-6K^{-1}, whereas the coefficient of thermal expansion for aluminum alloy used is 23.6e-6K^{-1}. The maximum and minimum calculated coefficient of

thermal expansion is 24.4e-6K^{-1} and 22.9e-6/K, suggesting that the difference is negligible.

5.5.2 Thermal swelling in the free condition

The temperature of the fixture was also increased during the pulse excitation because heat flows from the battery cell to the fixture through contacts, denoting that fixture was also thermally expanded. Hence, measured data should be calibrated to accurately estimate the thermal swelling of the battery cell. Eq. (29) is the modified equation from Eq. (28) when experiments were conducted with the battery cell. The pure thermal swelling of the battery cell was calibrated with this equation from the measurement.

$$\Delta L_{meaured} = -\Delta L_{fixture} + \Delta L_{sensor} + \Delta L_{cell}, \quad (29)$$

where ΔL_{cell} is the expansion of the battery cell.

Figure 34 (a) illustrates the 2-D thermal swelling shape obtained from usage-induced elevated temperature, i.e. experiment for 50A (10C) pulse excitation. The swelling shape does not have flat regions, which is shown in Li-ion intercalation swelling. This difference might be due to two physics behind the cell as aforementioned.

First, Li-ion intercalation swelling is caused by orthotropic expansion and uniform across the jellyroll. Hence, that swelling occurs mainly in a direction perpendicular to electrodes, which lead to a flat shape in the central region. In contrast, usage-induced temperature fluctuations are not uniform. For example, the center region is the hottest, whereas the edge region is the coolest in the *xy* plane due to the cooling effect (Figure 35 (a)), even though the variation is not significant. Thermal gradient is more significant through the battery cell, i.e. *z* direction in Figure 8. The core temperature of the jellyroll is increased up to 5℃ from 25℃ although the surface temperature of the case is increased up to 3℃ (Figure 35 (c)).

Second, the different constraints for the edge and central regions create the gap. The model prediction clearly shows the creation of the gaps and voids and therefore is in good agreement with measurement as shown in Figure 34 (b). The same legend is used in Figure 34 (b) with Figure 34 (a) for easy comparison. The maximum gap is 15μm on the center (30% with respect to the maximum swelling in measurement) and the same shape with the swelling of the case (not shown here for the sake of brevity), suggesting that gaps and voids play a critical role for thermal swelling at an unconstrained condition.

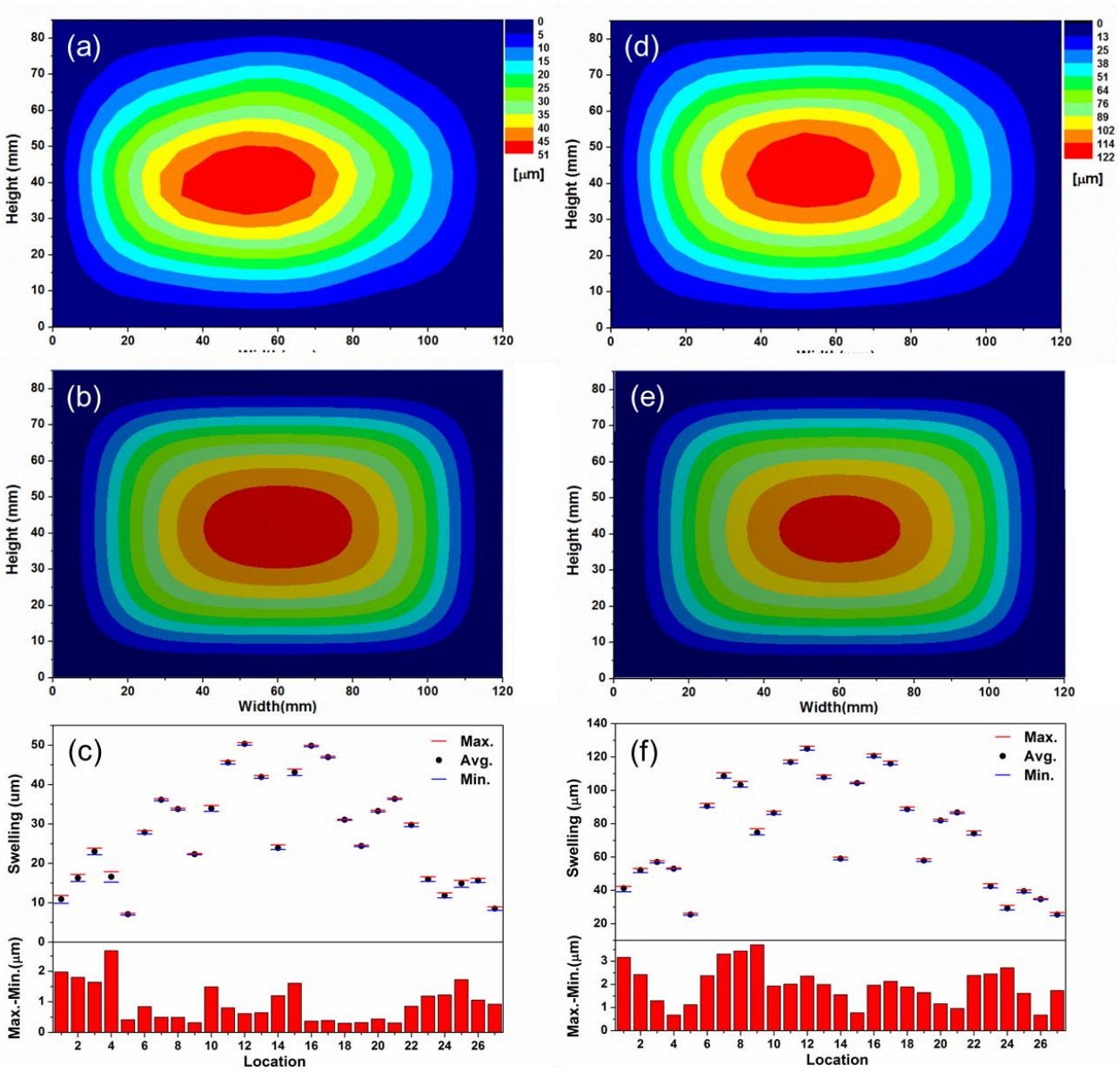

Figure 34. (Color online) Thermal swelling shape on the surface at 50A (10C) pulse excitation from (a) measurement, (b) model prediction; (c) the top shows the maximum, average, and minimum measured swelling at each location, the bottom shows the difference between maximum and minimum measured swelling at each location for 50A pulse excitation; thermal swelling shape on the surface at 75A (15C) pulse excitation for (d) measurement, (e) model prediction; (f) the top shows the maximum, average, and minimum measured swelling at each location, the bottom shows the difference between maximum and minimum measured swelling at each location for 75A pulse excitation

Figure 34 (c) shows the uncertainty and repeatability of 10C pulse experiments for all locations. The variability in the swelling measurements at the rear face is generally below 2μm (the bottom of Figure 34 (c)). The difference between the maximum and minimum measurement and the standard deviation of swelling at a reference location (on the front face

of the cell labeled 16 in Figure 8) is 3.2μm and 1.1μm, which was always measured during the experiment to check the variability in measuring the thermal swelling. These results confirm that the experiments are reliable and repeatable considering the accuracy of the displacement sensor and the noise of the thermal couples used to control the environmental temperature.

For a validation of the proposed model, the model prediction (Figure 34 (e)) was compared to experiments (Figure 34 (d)) for 15C pulse excitation because the equivalent thermal conductivity for the through-plane direction was calibrated with the data of 10C pulse excitation. In this simulation, the heat transfer coefficient was tuned to 60.5 $Wm^{-2}/℃$ to match the center temperature to the experiment at first; measured temperature on the center of the case was 31℃ as shown in Figure 35 (b). The model prediction is in excellent agreement with measurement. The thermal swelling at 15C pulse excitation is more rounded in the edge regions in comparison to thermal swelling at 10C pulse excitation. It can be explain by the fact that a large amount of swelling fills and eliminates more gaps and voids in the edge sides and thereby the shape is more smooth and rounded. However, this shape is still convex and elliptical opposite to Li-ion intercalation swelling, suggesting that nonuniform temperature distribution and gap effect still contributes to the shape of thermal swelling. The maximum gap is 38μm in the center, which is the 30% of swelling measured at the center same to 10C pulse excitation.

Figure 34 (f) shows the uncertainty and repeatability of 15C pulse experiments for all locations. The variability in the swelling measurements at the rear face is generally below 3μm (the bottom of Figure 34 (f)). The difference between the maximum and minimum measurement and the standard deviation of swelling at a reference location (on the front face of the cell labeled 16 in Figure 8) is 4.3μm and 1.4μm. These results confirm again that the experiments are reliable and repeatable.

One more interesting phenomenon is shown in the temperature measurement and thermal analysis. The surface temperature is increased 3℃ and 6℃ in two experiments, while the temperature on the center of the battery cell increases over 45℃ in Ref. [61] with similar pulse profiles. This comparison clearly demonstrates the importance of cooling the battery cell. The estimated heat transfer coefficient in this study is around 60 $Wm-^{2}/℃$, whereas that in Ref. [61] is to 6 $Wm^{-2}/℃$, which is similar to a natural convection situation. The cooling capacity for the chamber used in this study was ten times stronger than that used in Ref. [61].

Therefore, it can be inferred that the heat dissipation from the appropriate thermal management mitigates the thermal stress and strain. However, this strong forced convection and the lower thermal conductivity of the jellyroll result in greater temperature gradients through the battery cell (bottom of Figure 35 (c) and (d)). The core temperature is 4℃ higher than the maximum surface temperature in this study, while the core temperature is just 0.5℃ higher than the maximum surface temperature in Ref. [61]. In other words, forced convection results in a lower but more non-uniform temperature distribution through the battery cell due to the lower Biot number [85]. Non-uniform degradation might be induced by this non-uniform temperature distribution with the jellyroll. However, average temperature is a stronger determinant of cell aging than temperature uniformity [109]. Hence, a thermal management system with forced convection is expected to improve battery lifetime.

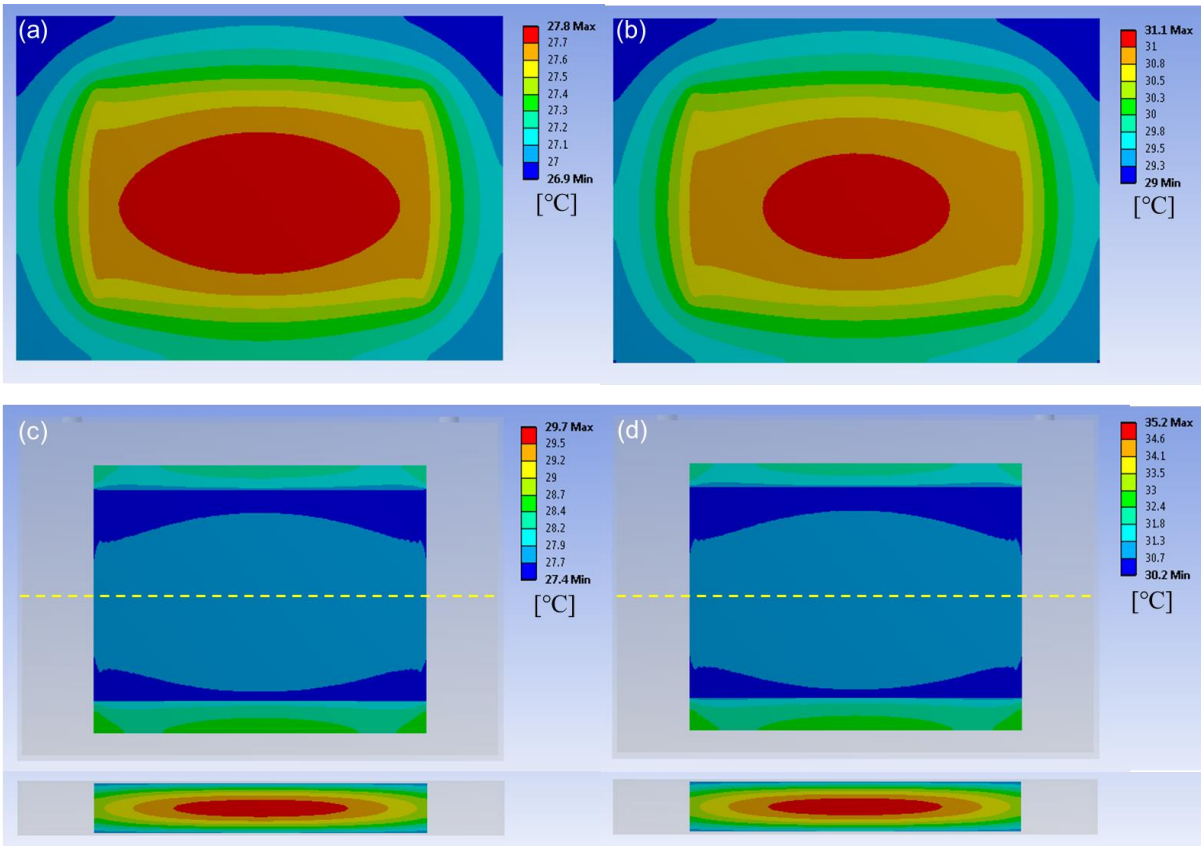

Figure 35. (Color online) Temperature distribution on the surface of the case at (a) 50A and (b) 75A pulse excitation; front view and cross-section view along the centerline of local temperature distribution for the jellyroll at (a) 50A and (b) 75A pulse excitation.

5.5.3 Thermal swelling in the pack condition

Figure 36 (a) compares the swelling from the temperature variation with the swelling from Li-ion intercalation in the center regions, i.e. in a region without contact with the spacer, at the pack condition. The diamond symbol denotes Li-ion intercalation swelling, while the circle symbol denotes thermal swelling. Three components, the jellyroll, case, and spacer, are used. To quantitatively compare the swelling from two different sources, uniform temperature change at 0.5SOC is assumed to the jellyroll in this simulation. Thermal swelling is in a linear fashion in terms of temperature, whereas Li-ion intercalation swelling is in a nonlinear fashion due to the phase transition. Moreover, swelling due to temperature elevation is similar in the order of magnitude with Li-ion intercalation, suggesting that thermal stress and strain is also very important for the battery safety and cycle life similar to the experimental result at an unconstrained condition in Ref. [42].

Figure 36 (b) shows the swelling shape on the surface of the case at elevated temperature in the pack condition. The swelling shape is exactly the same as that from Li-ion intercalation swelling. This similarity can be explained by the fact that large gaps and voids cannot be created between electrodes in the center due to the plastic spacer at the pack condition. Moreover, (relatively) large and uniform swelling can be observed in the center region in between the areas of contact with the spacer. This result suggests that geometric constraints on the cell swelling due to spacers are important in the pack conditions. Moreover, the pattern of swelling is repetitive and the amount of swelling (especially in the areas where there is no contact with the spacers) is the same in the center region, which is the area of contact between the jellyroll and the casing. Therefore, an appropriate location for placing the displacement or strain sensor in the pack condition is the center region, in a region without contact with the spacer. However, the quantitative swelling is so small that it can be measured with a high precise displacement or strain sensor. This small amount of swelling at the constrained condition suggests that the force due to the volume change of the cell can be a great alternative to characterizing the dynamic operational states.

To characterize the thermal mechanics and identify the discrepancy from a uniform thermal swelling at the batter pack during operation, 15C pulse excitation at pack condition was carried out (Figure 37). The boundary condition of the open surfaces for the case and spacer was set to the same forced convection to free swelling condition.

Figure 37 (a) and (b) shows the temperature distribution of the surface on the cell and the spacer in *xy* plane. Figure 37 (a) uses the same legend with Figure 35 (b) for quantitative

comparison. The overall trend is the same. However, slight low temperature distribution around 0.1℃ to 0.2℃ is observed even though the contact surface of the case was reduced due to the contact surface with the spacer. In addition, the contact surface of the spacer is the same temperature to the surface of the case, while the contact surfaces with air have the same temperature to ambient temperature (Figure 37 (b)). These results can be explained by the fact that the spacer also emits heat energy transferred from the case to environment, suggesting that the spacer is well designed and has carried out its duty in a series connection of the battery cell.

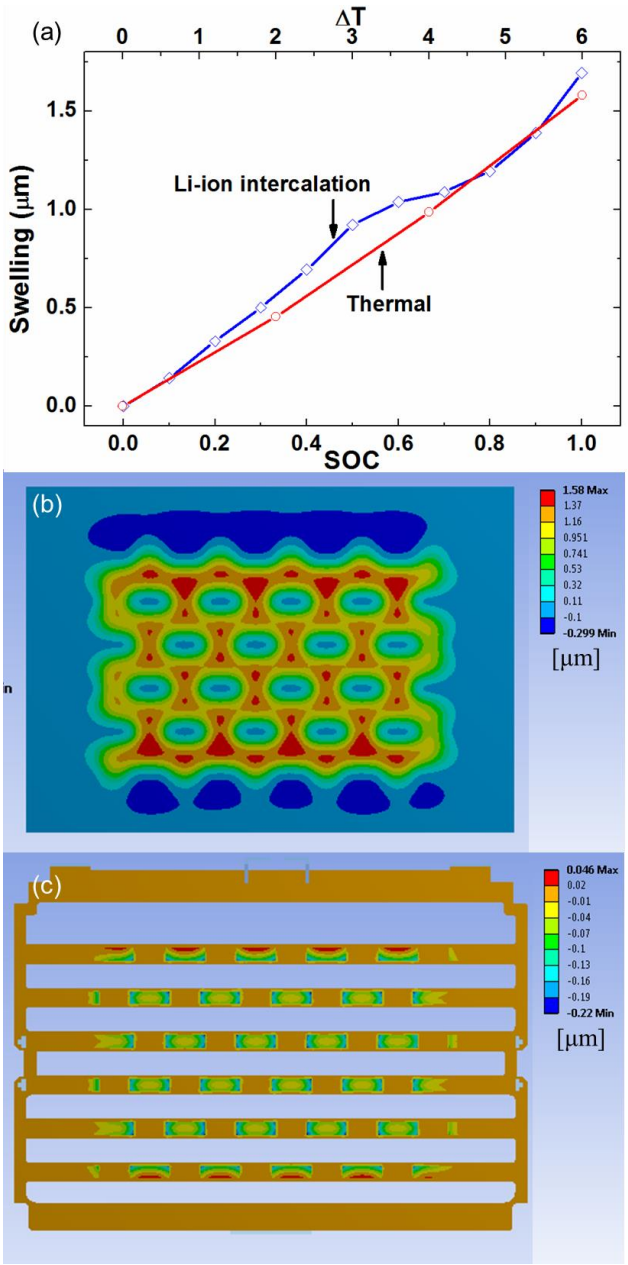

Figure 36. (Color online) (a) Swelling in the center between the dimples from two different sources at the pack condition; Li-ion intercalation (diamond symbol) and temperature

elevation (circle symbol). Swelling on the surface of (b) the case and (c) the spacer from the elevated temperature (ΔT: 6℃) in *xy* plane at the pack condition.

Figure 37 (c) demonstrates the thermal swelling shape on the case. As expected from the thermal swelling shape at free swelling condition, the largest and nonuniform swelling is observed opposite to uniform and the same thermal swelling in the central regions at constrained condition (Figure 36 (c)). Remarkably, the order of magnitude for swelling at pulse excitation is much larger than that for swelling at uniform temperature change, even though the surface temperature of the case is the same. This observation supports the hypothesis that the thermal swelling shape of the surface can be mainly attributed to the non-uniform temperature distribution of the jellyroll as well as the creation of the gaps and voids between electrodes. However, the gaps and voids are not created in a constrained condition because of the stiffness of the spacer opposite to a constrained condition, suggesting that non-uniform temperature is only important at the constrained condition. Further, the ratio between non-uniform swelling and uniform swelling at the center is similar to the ratio of the core temperature for two cases, suggesting that the core temperature plays a critical role in a thermal swelling perspective. The reaction force shows more significant difference than swelling; 193N for uniform temperature and 747N for non-uniform temperature of the jellyroll. This large difference suggests again that measured force can become a sensitive metric for identifying the state of the battery cells and packs.

The thermal behavior of the spacer is also different. The spacer thermally expands at the pulse excitation case (Figure 37 (d)), while the spacer is compressed in the simulation of uniform temperature change (Figure 36 (c)). This might be due to the reason that the temperature of the spacer in increased at the pulse excitation case, while the spacer keeps constant temperature with ambient temperature as assumed in the simulation. To sum up, the coupled thermal-structural analysis should be carried out with a novel model, which can account for non-uniform temperature distribution of the jellyroll and the creation of gaps and voids between electrodes, for the accuracy prediction of thermal swelling during operation at the pack condition.

A variety of simulations will be carried out with the proposed thermal swelling model for future work. It includes the dynamic thermal mechanics at different cooling conditions, thermal runaway, and nonuniform degradation induced by the temperature distribution with the jellyroll.

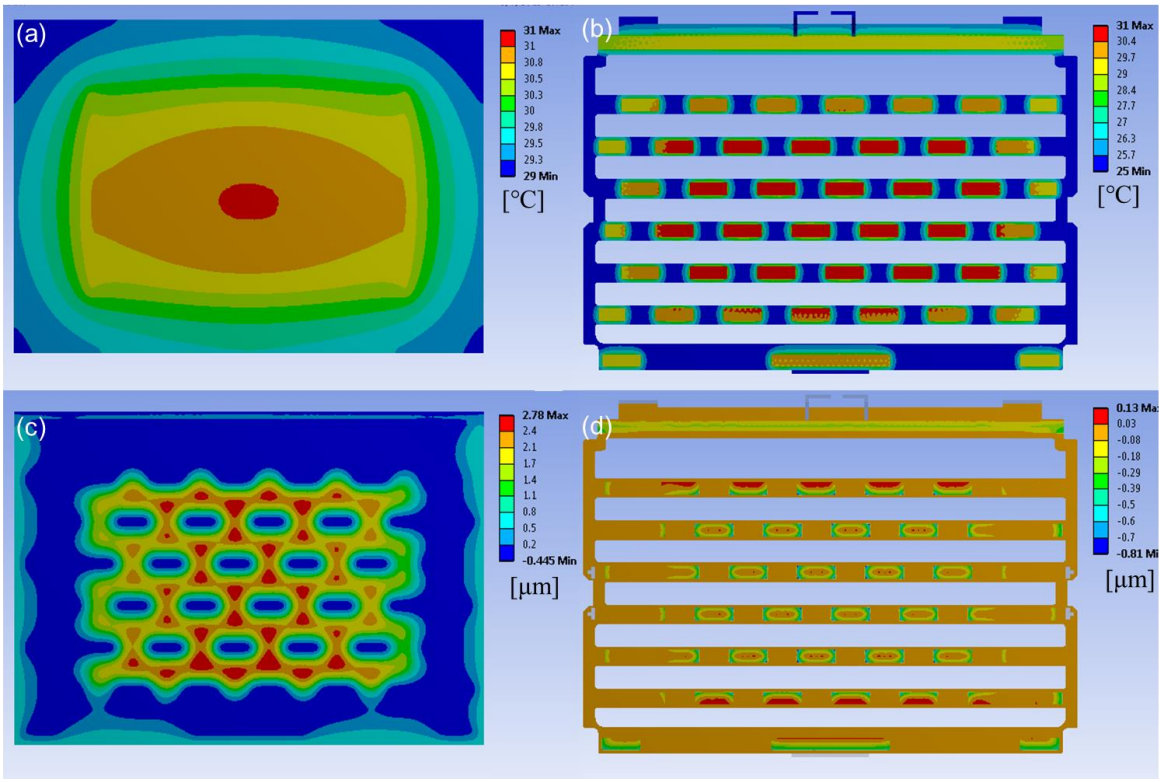

Figure 37. (Color online) Temperature distribution of the surface on (a) the cell and (b) the spacer in *xy* plane during 15C pulse excitation at the battery pack. Swelling of the surface on (a) the cell and (b) the spacer in *xy* plane during 15C pulse excitation at the battery pack.

5.6. Conclusions

The thermal mechanics of a prismatic battery cell used in the Ford Fusion HEV were investigated via simulation and experiment. To characterize the critical parameters of thermal swelling, pulse excitation experiments with constant SOC were carried out. Different shapes from thermal variation were found to have occurred from electrochemical reaction, i.e. Li-ion intercalation. Non-uniform temperature distribution and the creation of gaps and voids resulted in this difference. Based on the experimental characterization, a macroscopic model featuring two characteristics was proposed. The comparison between the experiment and the model prediction successfully demonstrated that the model accurately predicted thermal swelling at the unconstrained condition. Simulation of thermal swelling at the pack condition showed that the core temperature and nonuniform temperature played a critical role, whereas the gaps and voids disappeared at the pack condition due to the constraints from the spacer,

suggesting that the coupled thermal-structural analysis is indispensable to accurately predict the thermal swelling during operation at the pack condition.

CHAPTER VI
A novel phenomenological multi-physics model of lithium-ion battery cells

6.1. Motivation and background

Rechargeable lithium-ion batteries (LIBs) have various advantages compared to alternative batteries such as lead-acid and Nickel-metal hydride batteries. LIBs not only provide high power/energy density over a broad temperature range of operation, but also exhibit no memory effect, low self-discharge ratio, and long cycle life. [26-28]. These advantages make LIBs an ideal candidate for a wide variety of applications from small-scale portable electronics to massive-scale energy storage systems.

However, problems that persist in existing LIBs limit their application in transportation, military, and aerospace due to the stringent safety standards. The limitations of current battery technology include underutilization, capacity fade, thermal runaway, and stress-induced material damage. In order to overcome these challenges, understanding the complex multi-physics beyond the LIBs is indispensable. The flow of electrons is proportional to current and driven by difference in electrochemical potential between the electrodes. The high-rate charge and discharge generate a large amount of heat mainly due to the resistivity of the materials consisting of electrodes, separator, and current collectors in thermal perspective. Moreover, the variations of temperature and the interlayer spacing of carbon atoms in the particles contained within the negative electrode during electrochemical reaction generate the electrochemical- and thermal-induced stress and strain [42]. In other words, multiple phenomena occur concurrently in the LIBs during charge/discharge process.

The significant efforts have been devoted to understand and identify the complex physics behind the LIBs. The porous electrode theory, which solves lithium diffusion dynamics and charge transfer kinetics in a paired intercalation electrode system, has been proposed to predict the electrical response of a cell [111]. This physical-based model can predict microscopic level behavior and performance, whereas it requires a large computational power to solve the differential equations. An equivalent circuit model, which represents a cell as one serial resistance and double RC pairs in general, has also been proposed for control-oriented purposes to estimate the electrical response and the amount of heat generation [112-114]. A variety of heat transfer models have been created and validated through experiments [32-35]. Several lumped parametric thermal models have also been proposed for control-oriented purposes with the advanced power management schemes, which can be embedded to next-generation battery management systems (BMSs) [43,44,62]. Numerical simulations on the cell-level and pack-level with computational fluid dynamics and finite element methods have been conducted to predict the thermal dynamics of Li-ion battery cells and packs with experimental validation [2,31,100,115]. Coupled models between electrochemistry and heat transfer have also been suggested to elucidate the coupled effect of the current, potential, and temperature on the state of charge (SOC) and state of health (SOH) for large-scale LIBs [116-118].

Recent research focuses more on the structural response ranging from micro-scale to macro-scale. The volume change of electrode materials in LIBs under charge process has been intensively investigated to elucidate the electrochemical-induced stress and strain [4-11]. The effects of prestress and stress-evolution on capacity fade over time or cycling have also been studied [12,76]. This research promotes theoretical and experimental understanding of the structural response of the LIBS, especially in microscopic perspective. Moreover, the macroscopic stress and strain response from two sources, i.e. Li-ion intercalation and temperature variation, is observable and measureable with the advancement of sensor technology, suggesting that the structural response can become a sensitive gauge for characterizing the battery state [42,56]. However, studies related to stress and strain on the cell-level are still few, especially in modeling perspective. Moreover, the coupled model of stress and strain with electrochemical reaction and thermal dynamics of the LIBs has not been investigated in great detail, even though this fully-coupled multi-physics model can improve the safety and reliability of batteries, enhance the capability of cells and packs, and eventually prolong the lifetime of the LIBs.

This paper proposes a fully coupled phenomenological multi-physics model of the LIBs for the first time. The proposed multi-physics model couples the electric, thermal, and swelling effect on the force in a pack condition. The main purpose of this phenomenological model is to predict the temperature and force induced from the volume change of battery cells in health monitoring and control perspectives. Experimental validation at a variety of operational conditions confirms that the proposed multi-physics model accurately predicts the temperature and the compression force during operation at the overall SOC regions and the broad temperature range of operations. The multi-physics model, which is capable of predicting all physics behind the LIBs, can improve BMSs with novel power and thermal management schemes, and offer distinct advantages to enhance the capability of battery cells.

6.2. Experiments

This study used a flat-wound type prismatic 5Ah Li-ion cell obtained from a Ford Fusion HEV battery pack. Detailed information of the Li-ion cell is available in Ref. [42].

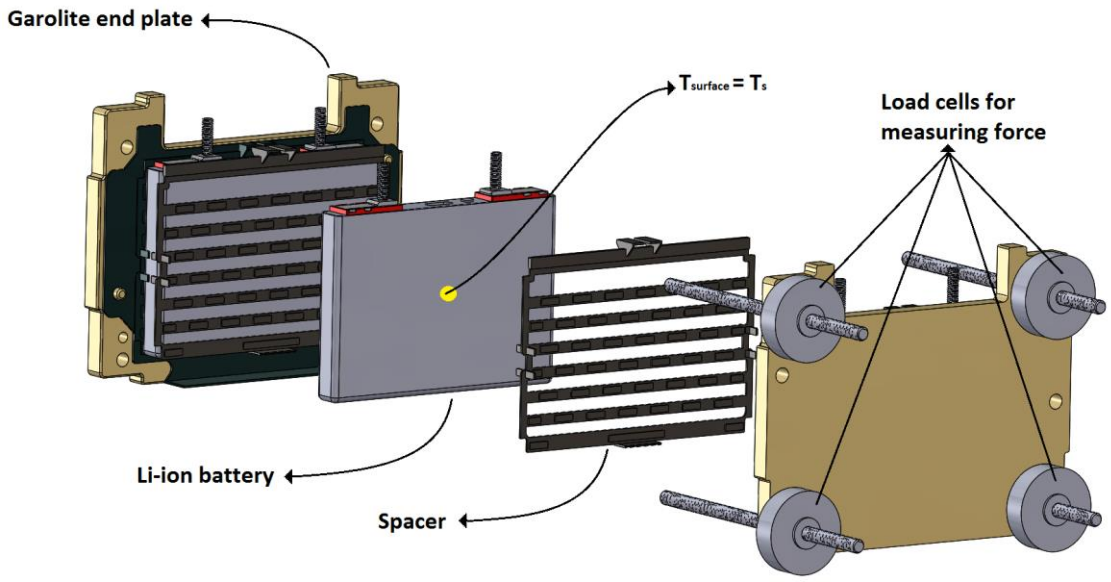

Figure 38. Schematic diagram of the experimental setup showing the fixture, the cell, the spacer, and the sensor location.

Three LIBs were sandwiched together between two Garolite end-plates and bolted to maintain a constant compression length in order to replicate conditions experienced in a battery pack. The battery cells were separated by spacers that maintain compression between the cells while allowing for airflow between them for cooling purposes as shown in Figure 8.

Battery temperature was measured on the surface of the cell by using resistance temperature detector sensors (RTDs). Battery force was measured by using four load cells, Omega LC8150-250-100 sensors with a 450N full-scale range and an accuracy of 2N, placed on the corners of the fixture. The fixture was placed in a thermal chamber for ambient temperature control, and the force and temperature data were collected via an 18-bit data acquisition card and a National Instruments module. Bitrode model FTV was used for battery cycling.

For characterizing the multi-physics model, different sets of experiments were performed, and are outlined below.

In the first experimental sets, the quasi-static force was measured at several different ambient temperature and two different preload conditions. Prior to discharge, the battery was fully charged using a CCCV protocol at 5A (1.0C) and rested three hours at a fixed ambient temperature of 25℃ as regulated by the thermal chamber; the voltage was clamped after reaching 4.1V, at which time it was held until the current tapered to C/100 (50mA). Then, the temperature of the thermal chamber was changed to the desired temperature (-5℃, 10℃, 45℃). Each temperature variation was followed by three hours of rest time to ensure thermal equilibrium. Note that this procedure was omitted to measure the quasi-static force at the ambient temperature of 25℃. In order to obtain the desired SOC ranging from 0% to 100% with 5% interval, the battery was discharged with a 0.4C current of actual capacity with an appropriate time (7.5 minutes). The actual capacity was calculated by using coulomb counting method during discharge with 0.4C rate from 4.1V to 3.0V herein. Each discharge was followed by three hours of rest time to ensure the quasi-static equilibrium. This procedure was repeated four times with the identical preload, 670N at 0.05 SOC, but different four ambient temperature (-5℃, 10℃, 25℃, 45℃) during discharge. These four experiments were also repeated with different preload, i.e. 450N at 0.05 SOC.

In the second experimental sets, three pulse excitation experiments were performed for validating the estimated coefficient of thermal expansion at an ambient temperature of 25℃ and the wide range of preload conditions. The battery was fully charged using standard CCCV protocol prior to discharge. Then, the battery was discharged with a 2A (0.4C) current for appropriate time to obtain three desired SOC. In the first experiment, a 50A charge sustaining pulse with a 1 second period (0.5 second charge and 0.5 second discharge) was applied for 2.5 hours at 0.48 SOC. The initial preload was set to 1276N. In the second experiment, a 50A charge sustaining pulse with a 100-second period (50 second charge and

50 second discharge) was applied for 2.5 hours at 0.22 SOC with an initial preload of 145N. The final experiment consisted of a 50A charge sustaining pulse with a 100-second period (50 second charge and 50 second discharge). The pulse was applied at 0.74 SOC with an initial preload of 330N.

Finally, for the validation of the multi-physics model, different sets of experiments were performed. These experiments consisted of applying a current profile measured from a Ford Fusion hybrid over US06 driving cycle. The US06 experiments were conducted at different initial SOCs, preloads and ambient temperatures as listed in Table 2.

Table 2. Conditions for the set of US06 experiments used for the validation of the multi-physics model.

Experiment	Initial SOC (%)	Ambient Temperature (℃)	Initial Preload (N)
1	50	25	935
2	50	11	950
3	33	11	550
4	50	11	600
5	66	11	680

6.3. Model description

The multi-physics model consists of three major components (Figure 39): a coupled Electro-Thermal Model (ETM), swelling models, and a force estimator. The ETM estimates the state of charge (SOC) and the surface/core temperature of the battery cell with the measured current and ambient temperature. The swelling models calculate the total amount of swelling for the battery cell at an unconstrained condition with SOC and the surface/core/ambient temperatures provided by the ETM. The force estimator calculates the reaction force caused by the volume change of the battery cell from Li-ion intercalation, temperature variation, and preload.

When creating the multi-physics model, the following assumptions are made:

1) The hysteresis of swelling and force during Li-ion intercalation and deintercalation is negligible.

2) The Li-ion intercalation swelling of battery cells in terms of SOC is not affected by temperature in the range of experiment (-5℃ to 50℃).

3) The equivalent coefficient of thermal expansion for a battery cell at a constrained condition can be different to that at an unconstrained condition. Gaps and voids easily generate and mechanical magnification of ruffling occurs at an unconstrained condition [6,57].

4) The material properties for battery cells can change with respect to SOC because of the phase transition.

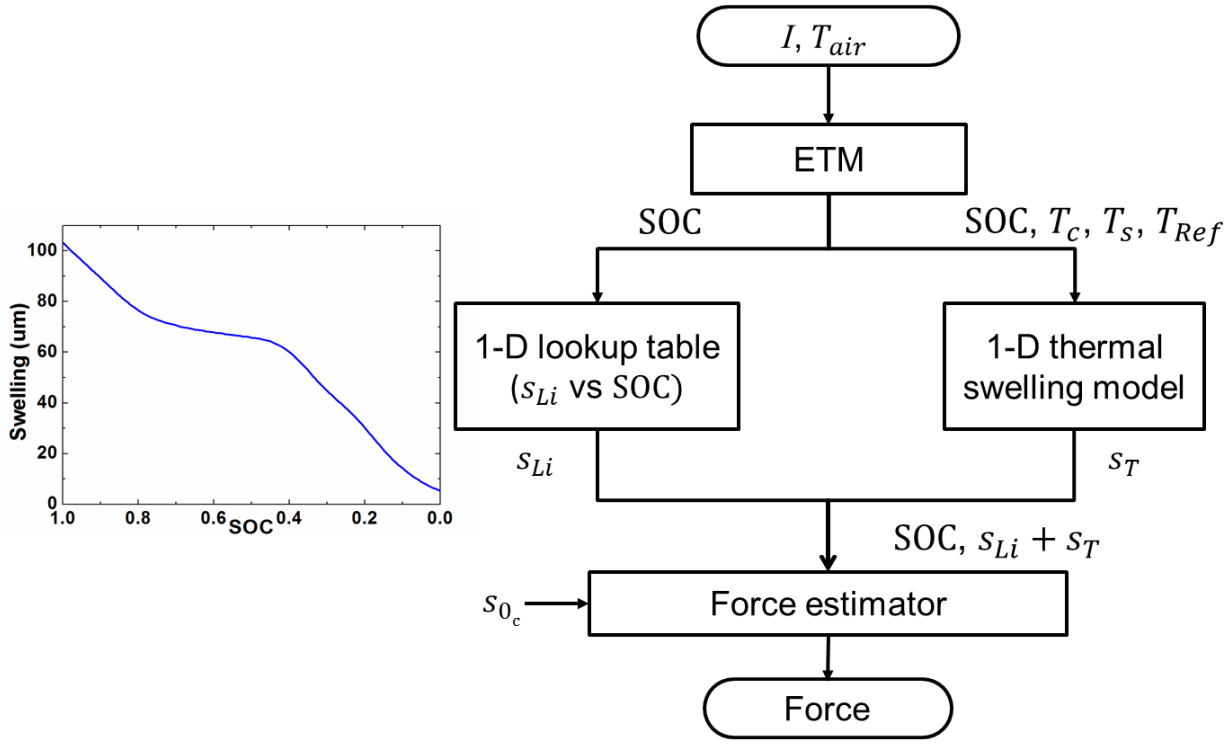

Figure 39. Overall structure of the multi-physics model for LIBs.

6.3.1 Coupled Electro-Thermal Model (ETM)

A coupled ETM was used for the prediction of temperature and SOC of the battery cell. The ETM is comprised of a two-state thermal model and a three-state electrical model per battery cell in the pack [119].

Heat transfer of the battery cell is captured by a lumped thermal capacitance approach. The battery cell is assumed to have interior and surface nodes with thermal capacitances, and the

two nodes are connected through a thermal resistance. The thermal capacitance is determined from density ρ, specific heat capacity c, and volume V; the thermal resistance is determined from thermal conductivity K, thickness L, and area A. Eq. (30) describes the heat transfer in the core of the cell.

$$(\rho cV)_c \dot{T}_c = \frac{KA}{L}(T_s - T_c) + I^2 R_s + \frac{V_1^2}{R_1} + \frac{V_2^2}{R_2} + IT_c \frac{dU}{dT}. \quad (30)$$

The first term of the right hand side of Eq. (30) is the heat conduction between the core and surface nodes of the cell, whereas the rest of the terms represent the heat generation. The terms $I^2 R_s + \frac{V_1^2}{R_1} + \frac{V_2^2}{R_2}$ represent Ohmic heat generation, while the term $IT_c \frac{dU}{dT}$ denotes the entropic heat generation. Eq. (31) determines the heat transfer on the surface of the cell.

$$(\rho cV)_s \dot{T}_s = \frac{KA}{L}(T_c - T_s) + hA(T_{amb} - T_s), \quad (31)$$

where the first term of the right hand side of Eq. (31) is the heat conduction between the core and surfaces node of the cell, and the second term is the heat convection to the ambient air. Note that thermal capacitance for the surface and the core is different in that the core represents jellyrolls whereas the surface represents aluminum casing.

Electrical dynamics of the battery cell, state-of-charge, polarization voltage, and terminal voltage, are predicted by Eqs. (32) and (33).

$$\begin{bmatrix} \dot{z} \\ \dot{V}_1 \\ \dot{V}_2 \end{bmatrix} = \begin{bmatrix} 0 & 0 & 0 \\ 0 & \frac{-1}{R_1 C_1} & 0 \\ 0 & 0 & \frac{-1}{R_2 C_2} \end{bmatrix} \begin{bmatrix} z \\ V_1 \\ V_2 \end{bmatrix} + \begin{bmatrix} -\frac{1}{Q} \\ \frac{1}{C_1} \\ \frac{1}{C_2} \end{bmatrix} [I], \quad (32)$$

$$\mathrm{V}_T = V_{OCV}(z) - V_1 - V_2 - IR_s, \quad (33)$$

where z is the battery SOC, Q is the capacity of the cell, and I is the current; V_1 and V_2 are the voltages across resistors R_1 and R_2 (or across capacitors C_1 and C_2) respectively, and R_s is the series resistance. The terminal voltage and open-circuit voltage are denoted by V_T and V_{OCV} respectively.

6.3.2 Swelling models

The volume of the LIBs is changed from two sources: Li-ion intercalation and temperature variation, suggesting that the total swelling from two sources should be considered to accurately predict the corresponsive reaction force during operation.

The interlayer spacing of atoms in the active material particles which make up the electrodes is affected by Li-ion concentration because the amount of Li-ion in each electrode is varied upon lithiation when lithiation and delithiation are occur concurrently in the cathode and anode. Especially, the layered structure such as graphite intercalation compounds shows significant volume change, whereas the spinel and olivine structures such as $LiMn_2O_4$ and $LiFePO_4$ minimally vary upon lithiation [19], suggesting that the volume change of graphite anode mainly contributes to the volume change of battery cells.

The swelling originated from Li-ion intercalation is calculated by using a lookup table. Measured swelling below 0.2C can be used to establish the lookup table to estimate pure Li-ion intercalation swelling. The temperature variation during discharge is below 0.1℃ when the battery cell was operated below 0.2C (Inset figure of Figure 39). Hence, data at 0.2C or lower C-rate below 0.2C allow direct correlation to be made between swelling and Li-ion intercalation in a cell sandwich, without significant convolution with thermal expansion. The lookup table was created through measurement at 0.2C herein.

Thermal swelling on the cell-level is similar in order of magnitude with Li-ion intercalation swelling, suggesting that thermal swelling is far from insignificant. Therefore, thermal swelling is estimated by using Eq. (34) [78] and added to Li-ion intercalation swelling to calculate the total volume change of the cell.

$$s_T(\mathrm{t}) = \alpha_{bat}(T, \mathrm{t}) \mathrm{L}_{bat} \left[\frac{2}{3}(T_c(t) - T_s(t)) - \left(T_s(t) - T_{Ref}\right)\right], \tag{34}$$

where s_T, α_{bat}, L_{bat}, T, t represent the thermal swelling of the cell, the equivalent coefficient of thermal expansion of the cell, the original thickness of the cell, temperature, and time. The subscript c, s, Ref denote the core, the surface, and the reference (ambient). This model accounts for the non-uniform temperature distribution throughout the battery cell to accurately predict the thermal swelling. Note that the equivalent coefficient of thermal expansion α varies in time because material properties of LIBs vary upon lithiation due to the phase transition similar to the modulus of elasticity [20,47]. Moreover, the equivalent coefficient of thermal expansion α_{bat} is assumed to depend on temperature. This assumption, which is different to Ref. [78], is addressed for the wide range of operational temperature of battery cells. In Ref. [78], the dependency of the equivalent coefficient of

thermal expansion on temperature is negligible because the temperature variation of battery cells is up to 3.5℃ in experiments. However, the coefficient of thermal expansion for many materials depends on temperature in the wide operational range of battery cells. Hence, the dependency of the coefficient of thermal expansion on temperature is additionally considered herein to create the high fidelity model.

6.3.3 Force estimator

Microstructure transformation of electrodes leads to the evolution of material properties due to the phase transition [52,53]. Especially, the material properties for the layered structure show significant change, whereas those for the spinel and olivine structures vary minimally upon lithiation [101]. Our previous work also showed the lithiation induced stiffening of the equivalent stiffness for a jellyroll over SOC. This study also suggested the phenomenological force model. The proposed force model can predict the force induced from the volume change of battery cells with free swelling measurement at constant ambient temperature in the wide range of preload condition.

In brief, the swelling over SOC was measured at an unconstrained condition, whereas the force over SOC was measured at a constrained condition with the preload and spacers. Both experiments were conducted at regulated temperature in a thermal chamber. The force was coupled with swelling with respect to SOC and governing equations were derived to identify the relationship between the force and the swelling. The model not only addressed the nonlinear elastic stiffness to capture the inherent nature of Li-ion intercalation swelling but also separated the overall SOC region into three regions considering the phase transition. This model also addressed the initial displacement to account for the preload effect; see chapter IV for the details about the governing equations and coupling procedures of two experiments.

The proposed force model in chapter IV assumed that the ambient temperature was constant and thereby the distance between two endplates was constant. However in reality, the ambient temperature of battery cells and packs varies upon weather, operation, and cooling conditions, suggesting that the distance between two endplates varies upon ambient temperature because of the thermal expansion/shrinkage of the frame of battery packs. Therefore, one more governing equation is derived herein to account for the variation of the

distance between two endplates due to the variation of ambient temperature [35]. This modeling is one of the key contributions in this chapter compared to chapter IV in the prediction of force in cells.

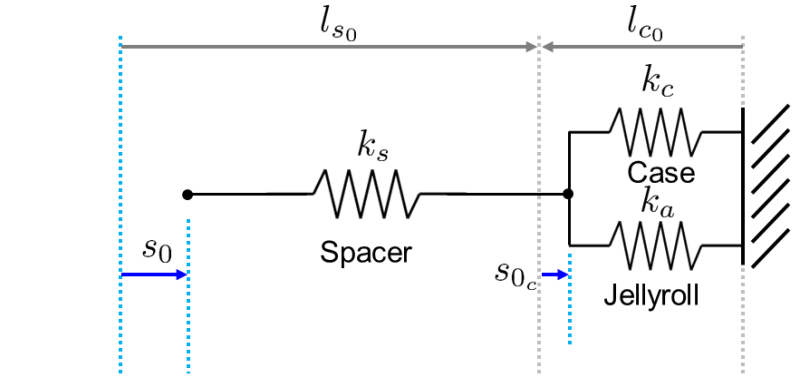

(a) Initial force equilibrium of the battery cell including the spacer with preload

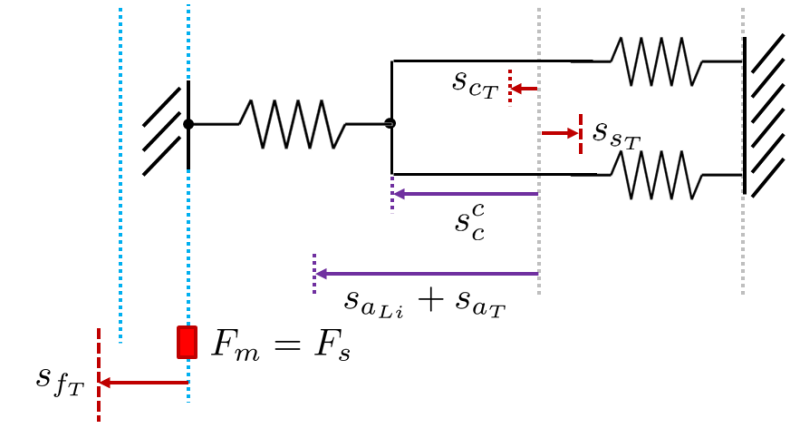

(b) Force equilibrium during operation at different ambient temperature

Figure 40. Force equilibrium for a constrained swelling of the battery cell with a plastic spacer account for the effects of the preload and temperature change; (a) initial force equilibrium at a certain ambient temperature and (b) force equilibrium at a different ambient temperature.

Figure 40 illustrates the two force equilibriums at a constrained condition. Figure 40 (a) depicts an initial assembled condition of experiment with preload at a certain constant ambient temperature (25℃ in experiments of chapter IV). The case and the jellyroll are connected in parallel in the sense that the case disturbs the expansion of the jellyroll. The spacer is added in series with the battery cell considering the serial connection of experiments. Then, the external load from tightening bolts causes the initial displacement for the spacer s_0 and battery cell s_{0_c}.

Figure 40 (b) illustrates the force induced from the volume change of the battery cell during lithiation/delithiation at a different ambient temperature (the first experimental sets). The ambient temperature was changed from one (25℃) to the desired temperature and then force

was measured during discharge. All components expand when ambient temperature increases (Figure 40 (b)). In Figure 40 (b), s_{f_T}, s_{s_T}, s_{c_T}, and s_{a_T} denote the thermal expansion of the bolt and Garolite endplate, the thermal expansion of the spacer, the thermal expansion of the case, and the thermal expansion of the jellyroll; $s_{a_{Li}}$ and s_c^c denote the swelling of the jellyroll due to Li-ion intercalation at an unconstrained condition and the swelling of the case (and the jellyroll) at a constrained condition.

The jellyroll and the spacer are compressed, whereas the case is stretched from the original length during Li-ion intercalation in the force equilibrium. Therefore, tensile forces act on the jellyroll and the spacer, whereas the compression force acts on the case in the force equilibrium. This force equilibrium results in Eq. (12).

$$F_s = -F_c + F_a, \tag{35}$$

where F_s, F_c, and F_a are the force induced from the spacer, the case, and the jellyroll respectively.

The variation of the length for the spacer is $s_c^c + s_0 + \mathrm{s}_{s_T} - \mathrm{s}_{f_T}$ in the force equilibrium at a certain elevated ambient temperature. The total compressed length is $s_c^c + s_0 + \mathrm{s}_{s_T}$, whereas the stretched length is s_{f_T} from an initial length. Note that the initial length of the spacer is not l_{s_0} but $l_{s_0} + \mathrm{s}_{s_T}$ at the certain elevated ambient temperature when unconstrained. Temperature increase changes the initial length of the spacer. Similar to the spacer, the variation of the length for the case and the jellyroll is $s_c^c - \mathrm{s}_{c_T}$ and $\mathrm{s}_{a_{Li}} + \mathrm{s}_{a_T} - s_c^c$ because the initial length of the case and the jellyroll is $l_{c_0} + \mathrm{s}_{c_T}$ and $l_{s_0} + \mathrm{s}_{a_{Li}} + \mathrm{s}_{a_T}$ considering the temperature variation at a certain charge state when unconstrained.

The force equilibrium results in Eq. (36), when Hook's Law is applied for the force equilibrium (Eq. (12)). The nonlinear elastic model ($F_a = k_{a_1} s + k_{a_2} s^3$) is addressed for the jellyroll to illustrate the force dependency on swelling. It is assumed that the stiffness of the spacer and the jellyroll has a softening at elevated temperature and this softening has a linear fashion in terms of temperature in the operation range of battery cells and packs. The polymer materials generally show the softening in the elasticity of modulus over temperature [55]. The spacer is made from polybutylene terephthalate (PBT), while the separator insider of the jellyroll is made from polyethylene (PE), polypropylene (PP), or combination thereof. Therefore, the stiffness of the spacer and the jellyroll can show the softening over temperature. The softening effect on the nonlinear stiffness for the jellyroll is assumed to be

negligible. The nonlinear stiffness is relatively smaller than the linear stiffness and thereby the effect of softening from nonlinear terms is small considering the higher order effect, i.e. the cubic term of swelling.

$$k_s(1-\mathrm{c}_s\Delta\mathrm{T})\left(s_c^c+s_0+\mathrm{s}_{s_T}-\mathrm{s}_{f_T}\right)= -k_c\left(s_c^c-\mathrm{s}_{c_T}\right)+k_{a_1}(1-\mathrm{c}_a\Delta\mathrm{T})\left(\mathrm{s}_{a_{Li}}+\mathrm{s}_{a_T}-s_c^c\right)+k_{a_2}\left(\mathrm{s}_{a_{Li}}+\mathrm{s}_{a_T}-s_c^c\right)^3, \quad (36)$$

where $\mathrm{c_s}$ and $\mathrm{c_a}$ denote the dependency of the equivalent stiffness on temperature in rate (percentage) for the spacer and the jellyroll. The dependency of the equivalent stiffness on temperature for the jellyroll is assumed to be identical for overall SOC regions.

The total thermal swelling of the fixture $\mathrm{s_{f_{Tot}}}$, which includes the thermal swelling of the bolt, the Garolite endplate, and the spacer, replaces the $\mathrm{s_{s_T}}-\mathrm{s_{f_T}}$. It is hard to distinguish the exact amount of thermal swelling from three components in the actual experiment. The equivalent length for each component is difficult to estimate because of the complex shape, especially for the spacer [56]. Mover, the coefficient of thermal expansion for each material is unavailable. The conventional equation for thermal expansion $(\alpha L)_{f_{Tot}}\Delta T$ replaces $s_{f_{Tot}}$ in Eq. (36) because $\Delta\mathrm{T}$ is the controllable parameter. The thermal expansion of the case can be calculated with the same formula because the coefficient of thermal expansion for aluminum, which is the material of the case, and the thickness of the case are available.

A more sophisticated approach is applied to the thermal expansion for the jellyroll. The coefficient of thermal expansion depends on SOC and temperature as aforementioned in section 3.2. Therefore, the thermal expansion of the jellyroll is expressed as $\alpha_a(\mathrm{SOC})(1+\beta\Delta T)L_a\Delta T$. The coefficient of thermal expansion for the jellyroll $\alpha_a(\mathrm{SOC})$ is separated into three values considering the phase transition: α_{a_L} for low SOC region (0-0.25 SOC), α_{a_M} for middle SOC region (0.5), α_{a_H} for high SOC region (0.75-1.0 SOC). This classification is followed by the trend of the equivalent coefficient of thermal expansion for the battery cell at an unconstrained condition [78]. The amplitude of thermal expansion at a constrained condition can be different than that at an unconstrained condition. However, the trend of variation over SOC is presumably similar because this trend is caused from the inherent nature of electrochemical reaction, i.e. Li-ion intercalation and phase transition. These replacements results in Eq. (37).

$$k_s(1-\mathrm{c}_s\Delta\mathrm{T})\left(s_c^c+s_0+(\alpha L)_{f_{Tot}}\Delta T\right)=-k_c\left(s_c^c-\mathrm{s}_{c_T}\right)+k_{a_1}(1-\mathrm{c}_a\Delta\mathrm{T})\left(\mathrm{s}_{a_{Li}}+\alpha_a(\mathrm{SOC})(1+\beta\Delta T)L_a\Delta T-s_c^c\right)+k_{a_2}\left(\mathrm{s}_{a_{Li}}+\alpha_a(\mathrm{SOC})(1+ \quad (37)$$

$$\beta\Delta T)L_a\Delta T - s_c^c\big)^3,$$

The measured force in load cells is the same as the compression force of the spacer in the force equilibrium because load cells are installed in the one side of Garolite endplate (red filled square in Figure 40 (b)) as shown in Eq. (38).

$$F_m = k_s(1 - \mathrm{c}_s\Delta\mathrm{T})\big(s_c^c + s_0 + (\alpha L)_{f_{Tot}}\Delta T\big), \tag{38}$$

The swelling of the case at a constrained condition can be derived in terms of the unconstrained swelling of the jellyroll, the initial displacement of the spacer, and the variation of temperature with respect to the reference temperature from Eq. (37); $s_c^c = h(\mathrm{s}_{a_{Li}}, s_0, \Delta T)$. The initial displacement of the spacer can be expressed in terms of that of the case (battery cell); $s_0 = g(s_{0_c})$. The swelling of the jellyroll can be derived in terms of the measured swelling of the case at a free condition; $\mathrm{s}_{a_{Li}} = f(\mathrm{s}_c^f)$, where s_c^f is the swelling of the case at an unconstrained condition. Finally, plugging three equations into (38) results in Eq. (39). The measured force at a construction condition is a function of the variation of temperature, the measured swelling of the case at an unconstrained condition, and the initial displacement of the case due to the preload. This equation suggests that the force at a constrained condition can be predictable if the variation of temperature, the swelling over SOC at an unconstrained condition, and initial displacement due to preload are available. The full equation is omitted herein for the sake of brevity.

$$F_m = k_s(1 - \mathrm{c}_s\Delta\mathrm{T})\big\{h\big(f\big(\mathrm{s}_c^f\big), g\big(s_{0_c}\big), \Delta T\big) + g(s_{0_c}) + (\alpha L)_{f_{Tot}}\Delta T\big\}, \tag{39}$$

To estimate the force induced from the volume change of the battery cell in the wide range of operational ambient temperature, seven parameters should be identified; c_a, c_s, $(\alpha L)_{f_{Tot}}$, α_{a_L}, α_{a_M}, α_{a_H}, and β. Other parameters used in the model were already identified in chapter IV. Therefore, the parameter estimation was conducted with measured forces at the identical preload and four different ambient temperatures by using the nonlinear least square method (Figure 41 (a)). The identical initial displacement (s_{0_c}), which was estimated from the triangle symbols of Figure 4 in chapter IV, was used in this parameter estimation. The coefficient of determination (R^2) is over 0.99 for all fitted regions, suggesting that the fitted curves are consistent with measured data in overall regions. The solid lines are model predictions, whereas the symbols are experiments in Figure 41 (a). The identified parameters are listed in Table 3.

Table 3. Estimates of the thermal characteristics of the model for battery cells that relates the force and swelling over SOC measured by displacement sensors and load cells.

Parameter	Value	Unit
c_a	0.01	%/ K
c_s	3.00	%/ K
$(\alpha L)_{f_{Tot}}$	1.63×10^{-6}	m/K
α_L	1.42	1e-4/K
α_M	1.20	1e-4/K
α_H	1.32	1e-4/K
β	2.5	%/ K

The estimated coefficient of thermal expansion for a jellyroll α_* for different SOCs is similar in order of magnitude. However, maximum difference is around 15%, suggesting that the difference from the phase transition is not negligible. Moreover, the temperature dependency of the coefficient of thermal expansion β is not small and is essential to predict the dynamic response of battery cells for the wide range of operational temperature. The equivalent coefficient of thermal expansion for the battery cell $\alpha_{bat}(T,\mathrm{t})$, which is used to estimate the thermal swelling of the battery cell in section 3.2, is calculated by using Eq. (40) with the coefficient of thermal expansion and the thickness of the jellyroll and the case (Figure 41 (c)).

$$\alpha_{bat}(T,\mathrm{t})L_{bat}\Delta\mathrm{T} = \alpha_c L_c \Delta\mathrm{T} + \alpha_a(T,\mathrm{t})L_a\Delta\mathrm{T}, \tag{40}$$

where α_c, L_c denote the coefficient of thermal expansion and the thickness of the case made from aluminum. The coefficient of thermal expansion for a battery cell is also linearly proportional to temperature, but the magnitude of the coefficient of thermal expansion for a battery cell is 9% smaller than that for a jellyroll because of the small coefficient of thermal expansion of the aluminum case.

The softening of the stiffness for the spacer is significant, while that for the jellyroll is negligible. One plausible explanation is that polymer material, the separator, in battery cells is small portion below 30%, whereas the whole spacer is made from PBT. The other explanation is that PBT shows more significant temperature dependency. However, the exact origin for these results is hard to explain before characterizing the thermal characteristics of individual materials. The material properties of polymer materials significantly depend on many things such as the atomic structure, the density of materials, and the manufacturing

process even for the same material. Therefore, polymers show a wide range of variation, which is why research has been intensively carried out to elucidate the material properties of individual polymer materials [55].

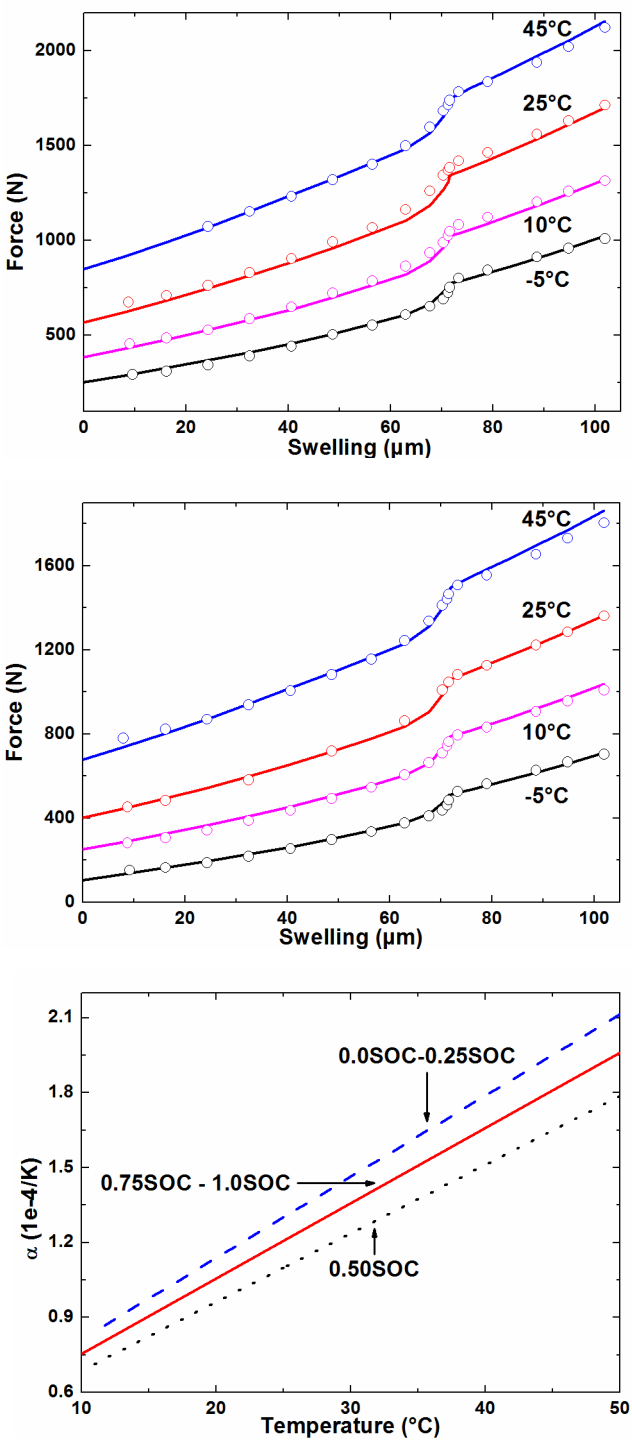

Figure 41. Force versus swelling at several ambient temperatures with the preload of (a) 670N and (b) 450N (at 0.05SOC and 25℃ temperature); (c) the coefficient of thermal expansion of the battery cell over temperature at different SOCs; the solid-lines are forces predicted from the model, whereas the circle symbols are forces measured in (a) and (b) of the figure.

Note that measuring all thermal characteristics of individual materials is very time and cost intensive. The purpose of this study is to create the phenomenological multi-physics model on the cell-level for control-oriented purpose, not to identify the thermal characteristics of individual components.

6.4. Validation

Intensive experimental validation was carried out to verify the force prediction. The ETM has already been validated at a variety of operational conditions in Ref [119]. Section 6.4.1 compares the predicted quasi-static force induced from the Li-ion intercalation to experiments at a variety of ambient temperature. Section 6.4.2 presents the model prediction of force due to the thermal expansion of battery cells and compares to pulse excitation experiments at three different internal charge states. Finally, the proposed model was validated through experiments where the power split from a fusion HEV traversing the US06 drive cycle was applied at different SOCs, preloads, and ambient temperatures in section 6.4.3.

6.4.1 Force induced from Li-ion intercalation in a steady state

The model predictions were compared to the force measured with a different preload than preload used for the parameter identification in section 3 at several ambient temperatures for the validation of identified parameters (Figure 41 (b)). The identical initial displacement s_{0_c}, which was estimated from the circle symbols of Figure 19, was applied for the force model in this verification with the same parameters listed in Table 1. In other words, the initial displacement is only a parameter changed from the data used in the parameter identification in this simulation to verify the parameters. The solid-lines are model predictions, whereas the symbols are experiments in Figure 41 (b). The surface temperature of battery cells is not shown herein because the temperature of battery cells is identical to ambient temperature in a steady state. The model prediction is in excellent agreement with measured data, suggesting that estimated parameters are accurate and reliable, and thereby the proposed model can predict the electrochemical-induced force at the wide range of preload and ambient temperature at the steady state. Moreover, this result justifies the hypothesis that the Li-ion

induced swelling of battery cells over SOC is constant regardless of temperature in the range of experiment.

6.4.2 The equivalent coefficient of thermal expansion

The surface temperature and force from the temperature elevation are compared to second experimental sets; pulse excitation experiments at three different internal charge states: 0.22 SOC, 0.48 SOC, and 0.74 SOC (Figure 42). The solid lines are measurements, whereas the dashed lines are model predictions in Figure 42.

The surface temperature of the battery cell is presented in Figure 42 (a). The heat convection coefficient was slightly tuned around 10 $Wm^{-1}K^{-1}$. Note that the heat convection coefficient depends on the location of experimental setup even in the same thermal chamber. The flow rate is different in the same chamber and depends on the location. The long period of pulse excitation results in the triangular fluctuation in the surface temperature at 0.22 SOC and 0.74 SOC, whereas the short period of pulse excitation causes the first order response. These phenomena can be explained by the fact that entropy change plays a role in the long period of pulse excitation, whereas this effect is negligible in the short period of pulse excitation. Entropy heat is endothermic, i.e. heat sink, during charge and exothermic, i.e. heat source, during discharge. Therefore, the short period of pulse excitation is better to obtain the pure thermal response. The root-mean-square errors (RMSE) in the surface temperature are 0.25℃, 0.20℃, and 0.21℃ at 0.22SOC, 0.48SOC, and 0.74SOC respectively. This difference is similar in order of magnitude with the results in Ref. [119].

The estimated force induced from thermal expansion is compared to experiments (Figure 42 (b)-(d)). Different SOCs and preloads were induced to the experimental setup to validate the model prediction in the wide range of preloads and SOCs. The initial displacements were estimated with initial measured forces and SOCs for each case by using Eq. (39). The measured force at 0.48 SOC (Figure 42 (c)) clearly shows the first-order response similar to surface temperature, suggesting that this reaction force is originated from the variation of temperature. This result confirms again that the short period of pulse excitation minimally changes the SOC and thereby results in pure thermal expansion and its induced force. On the other hand, the long period of pulse excitation accompanies the variation in SOC as clearly shown in the measured force at 0.22 SOC (Figure 42 (b)) and 0.74 SOC (Figure 42 (d)). The

wide fluctuation from Li-ion intercalation is shown together with the first-order response, which is caused from the temperature elevation. Moreover, this result not only justifies the hypothesis that the coefficient of thermal expansion for the jellyroll depends on SOC, but also validates that the estimated coefficient of thermal expansion is accurate and reliable. The model predictions are in good agreement with experiments in all SOC regions. The RMSE in the predicted force are 16.2N, 11.7N, and 13.9N at 0.22 SOC, 0.48 SOC, and 0.74 SOC respectively. The simulation results also show that the error is not affected by the amount of preload.

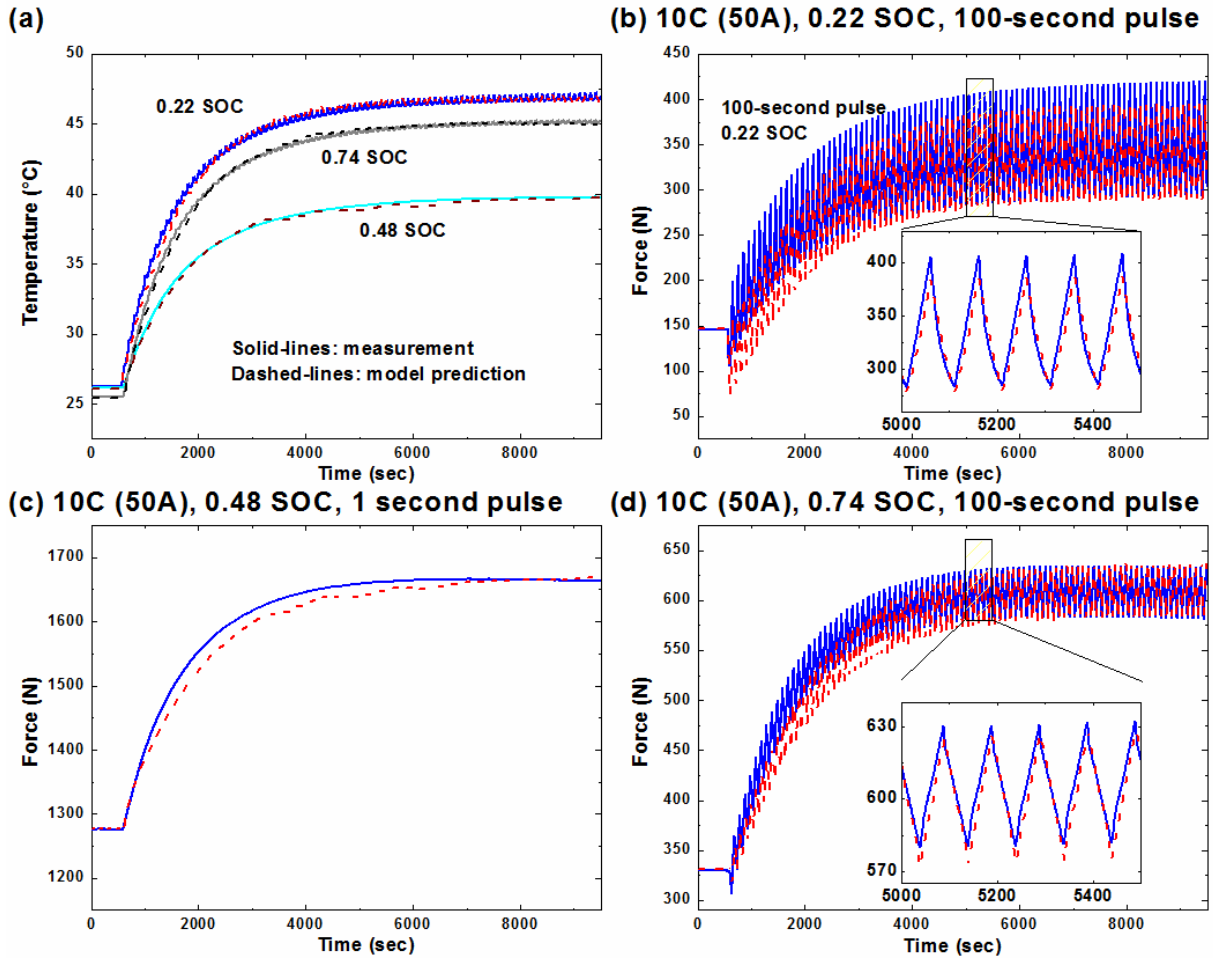

Figure 42. (a) Surface temperature and force of the battery cell during pulse excitation at (b) 0.22SOC, (c) 0.48SOC, and (d) 0.74SOC; the solid-lines are the surface temperature measured, whereas the dashed-lines are the surface temperature predicted in figure (a); the solid-lines are the force measured, whereas the dashed-lines are the force predicted in figure (c)-(d).

The wide fluctuation is shown at 0.22 SOC even though the preload induced is smaller; the magnitude in peak-to-peak due to Li-ion intercalation is over 100N at 0.22 SOC, whereas that is around 50N at 0.74 SOC. This observation can be explained by the amount of Li-ion intercalation swelling. The amount of swelling from Li-ion intercalation is 22μm when SOC

fluctuates in the range of 0.09 SOC to 0.22 SOC, while that from Li-ion intercalation is 4μm when SOC fluctuates in the range of 0.60 SOC to 0.74 SOC. The swelling due to Li-ion intercalation gently increases in the range of 0.45 SOC to 0.75 SOC (Figure 39). However, the magnitude of fluctuation should be less than 30N at 0.74 SOC when ignoring the nonlinear effect from preload, suggesting that high preload magnifies the fluctuation of force at 0.74 SOC. The nonlinear effect of preload will be described in details in the next section.

6.4.3 US06 duty cycle

Five operational conditions were tested with the US06 duty cycle for the validation of the dynamic response (Table 2). First, the battery cell was operated with a certain preload and the initial SOC of 0.50 at 25℃ ambient temperature. In the second case, the same configuration (the same preload and initial SOC) was used except ambient temperature. This case ran at 11℃ ambient temperature. Third, the initial SOC and preload were reduced, whereas ambient temperature was kept to 11℃ ambient temperature. In the fourth and fifth experiments, preload was more reduced; the preload induced was almost half of the first and second cases. Two different initial SOCs were tested at 11℃ ambient temperature. The temperature dependency of parameters was validated through the first and second experiments because these experiments used the identical preload and SOC. The dynamic force response in the wide range of force was verified through the second to fourth experiments. Finally, the dynamic force response in the wide range of SOC was validated through the third to fifth experiments.

Measured surface temperature and force with the initial 0.50 SOC at 25℃ ambient temperature (the first experiment in Table 2) are shown as the solid lines in Figure 43. The surface temperature estimated is in excellent agreement with the surface temperature measured. The RMSE in the prediction of surface temperature is 0.19℃. Two conditions were simulated in the estimation of force to elucidate the nonlinear effect from preload. The first set of results assumed that the initial displacement was zero and then added a certain amount of force to match the initial force (the symbols in the bottom of Figure 43). The second set of results estimated force by using the Eq. (39) with the initial displacement to accurately predict the force including nonlinear effect, which is originated from preload (the dashed line in the bottom of Figure 43). This comparison clearly demonstrates the importance of the nonlinear effect from preload. The RMSE of the force estimation for the first set is

97.6N, whereas the RMSE of the force estimation for the second set is 16.1N. These errors correspond to 7.5% and 1.2% with respect to the maximum force measured in this experiment. The error from the model prediction without the nonlinear effect from preload is over six times larger than the error from the accurate model prediction, suggesting that initial displacement from the preload plays a critical role in the estimation of the force and thereby the nonlinear effect from preload should be considered to accurately predict the force.

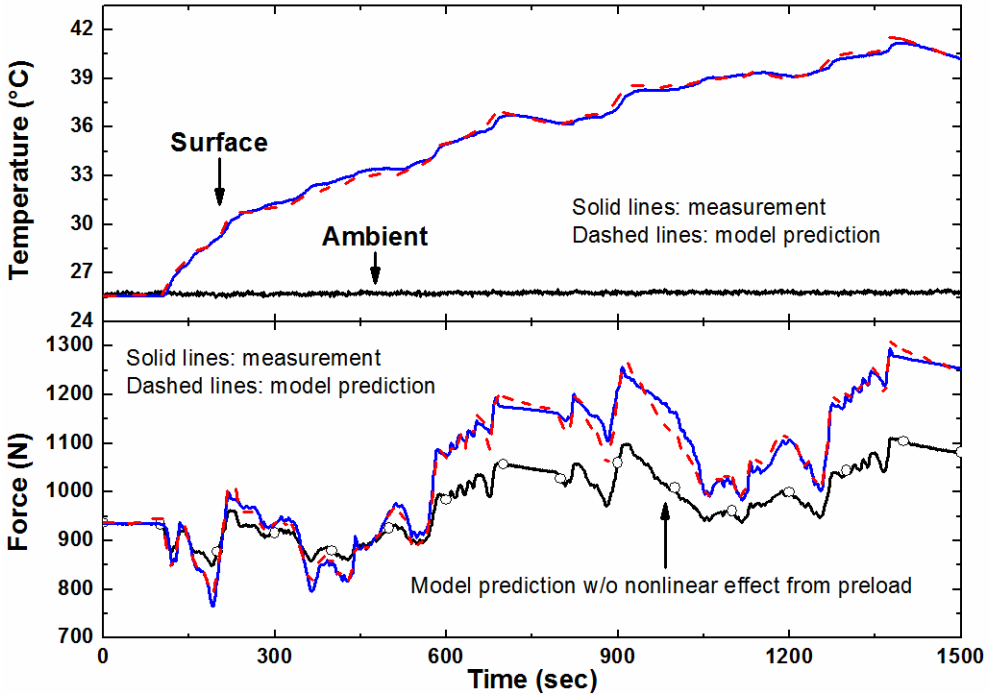

Figure 43. (Top) Temperature and (bottom) force of the battery cell with initial 0.50SOC during the US06 duty cycle at 25℃ ambient temperature; the solid-line is the surface temperature measured, whereas the dashed line is the surface temperature predicted in the top of the figure; the solid lines, the dashed line, and the symbols denote the force measured, the force predicted including the nonlinear effect from preload, and the force estimated without nonlinear effect from preload in the bottom of the figure.

Figure 44 shows the second and third experiments in Table 2 together with the estimation of the proposed model. These experiments were tested at 11℃ ambient temperature as aforementioned. However, the second used the identical SOC and preload with those of the first experiment, whereas the third used different SOC and preload. The solid lines show the surface temperature measured, while the dashed lines represent the surface temperature predicted in the top of Figure 44. The prediction of surface temperature is in excellent agreement similar to other cases. The RMSE in the prediction of surface temperature is 0.20℃ for the second case and 0.19℃ for the third case. The multi-physics model also accurately predicts the force for the overall period of experiments (the bottom of Figure 44).

The solid lines show the force measured, while the dashed lines represent the force predicted in the bottom of Figure 44. The RMSE in the prediction of force is 19.4N for the second case and 12.2N for the third case.

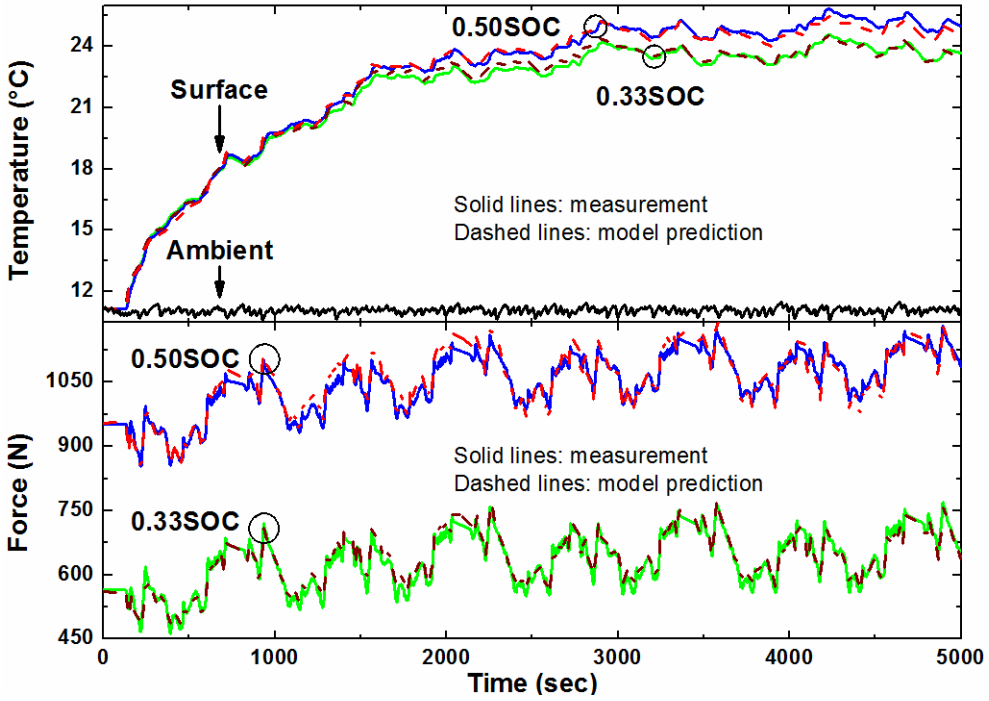

Figure 44. (Top) Temperature and (bottom) force of the battery cell during the US06 duty cycles with different preload and different SOC at 11℃ ambient temperature; the solid lines are the surface temperature measured, whereas the dashed lines are the surface temperature predicted in the top of the figure; the solid lines are the force measured, whereas the dashed lines are the force predicted in the bottom of the figure.

Figure 45 illustrates the fourth and fifth experiments in Table 2 with the prediction of force. These experiments were tested with the same preload at 11℃ ambient temperature. However, the fourth one was operated with the initial SOC of 0.50, whereas the fifth was operated with the initial SOC of 0.66. The temperature measured is shown as the solid lines, while the temperature predicted is represented as the dashed lines in the top of Figure 45. The surface temperature predicted corresponds well with the surface temperature predicted. The RMSE in the prediction of surface temperature is 0.18℃ for the fourth case and 0.22℃ for the fifth case. The dynamic response of force is shown in the bottom of Figure 45. The solid lines show measurement, whereas the dashed lines represent model prediction. In two simulations, the same initial displacement was used and other parameters used were identical. The force predicted is also in good agreement with the force measured. The RMSE in the prediction of force is 15.8N for the fourth case and 7.6N for the fifth case.

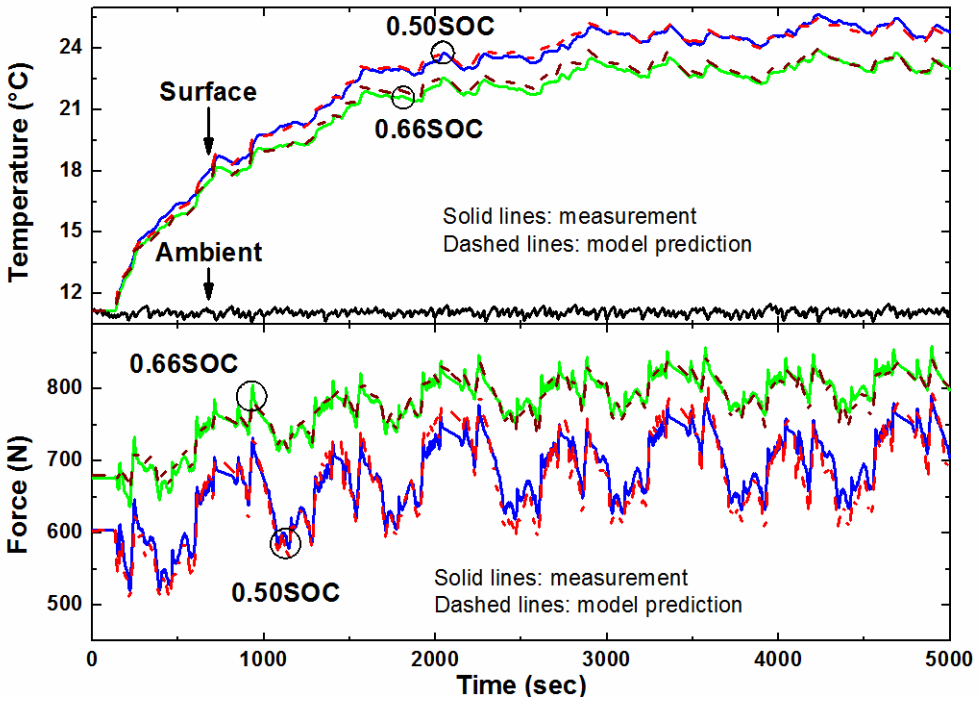

Figure 45. (Top) Temperature and (bottom) force of the battery cell during the US06 duty cycles with the same preload and different SOC at 11℃ ambient temperature; the solid lines are the surface temperature measured, whereas the dashed lines are the surface temperature predicted in the top of the figure; the solid lines are the force measured, whereas the dashed lines are the force predicted in the bottom of the figure.

The first experiment demonstrates the importance of nonlinear effect from preload. The first and second experiments show that the proposed model can operate regardless of ambient temperature. The experimental conditions for the first and the second experiments are identical except ambient temperature and thereby use the same parameters including the identical initial displacement to estimate the dynamic response of force in the model. These results suggest that the force model proposed is capable of the distance variation of two endplates with respect to temperature as well as the dependency of the stiffness and the coefficient of thermal expansion on temperature. The results of the fourth and the fifth experiments show that the model with appropriate initial displacement accurately predicts the dynamic response of force with the same parameters. Moreover, the capability of the force model in the wide range of SOC and preload were verified through the second to fifth experiments. In summary, the multi-physics model proposed herein accurately predicts surface temperature and force caused from two sources, i.e. electrochemical reaction and temperature variation, at the wide range of preload and ambient temperature. The validation of the estimated core temperature and SOC are not conducted herein. The conventional method, column counting method, is used to estimate SOC. Measuring the core temperature

of the battery cell is difficult, especially for prismatic cells. However, the validation of the force is an indirect way to validate the core temperature and SOC estimated. The estimated core temperature and SOC are used as input parameters in the force model.

6.5. Conclusions

Predicting sensitive metrics such as temperature and electrochemical- and thermal-induced strain and stress can provide useful information to estimate SOC in battery cells and packs. For these purposes, this study proposes the fully coupled phenomenological multi-physics model for innovative power and thermal management strategies in the next generation BMS. The intensive experimental validation at a variety of operational conditions demonstrates that the proposed model accurately predicts the surface temperature and the reaction force from the volume change of the battery cell at the wide range of preload and ambient temperature. Estimating SOC based on fusing information from voltage, temperature, or force measurements will be the subject of future work.

CHAPTER VII
Conclusions

7.1. Dissertation Contributions

The main contributions of this dissertation are summarized as follows.

- Quantitative swelling on the cell-level from two sources, namely Li-ion intercalation and temperature variation, was successfully identified through experiments. These measurements also showed that thermal swelling is similar in order of magnitude with Li-ion intercalation swelling and thereby far from insignificant. The swelling significantly varies upon C-rate due to thermal swelling, whereas the potential minimally with the C-rate, suggesting that measurements of mechanical response may provide a sensitive metric for characterizing dynamics operational states. As a demonstration, signatures of phase transitions in the negative electrode were identified by analyzing strain as a function of capacity; this response was also found to depend strongly on the C-rate. Moreover, swelling experiments with many locations on the surface showed that thermal swelling shape is different than Li-ion intercalation swelling shape, motivating to develop a 3-D numerical and phenomenological model.
- Important material properties such as the equivalent stiffness and the equivalent coefficient of thermal expansion were characterized through experiments. There parameters showed nonlinear characteristics over temperature and state of charge due to material transformation and complex geometry of battery cells (including hundreds of contact surfaces between electrodes) and mechanical constraints. Therefore, the importance of mechanical constraints and nonlinear dependence over temperature were demonstrated.

- Several 1-D models were developed based on experimental characterizations: a 1-D thermal swelling model, a 1-D force model, and a 1-D Li-ion relaxation model. The 1-D thermal swelling model incorporated an equivalent coefficient of thermal expansion on the cell-level. Moreover, the models addressed a 1-D heat transfer approximation to account for the temperature distribution throughout the battery cell. Experimental validation at a variety of C-rates demonstrated that the proposed model is simple yet very accurate in the prediction of thermal swelling during operation and relaxation. The 1-D force model can estimate the Li-ion intercalation induced force at actual pack conditions at the wide range of preload conditions. This force model not only addressed the nonlinear elastic stiffness to capture the inherent nature of Li-ion intercalation swelling but also separated the overall SOC region into three regions considering the phase transition. The 1-D Li-ion relaxation model predicts dynamic swelling due to Li-ion intercalation during the relaxation periods. This model addressed the 1^{st} order visco-elastic mechanical relaxation observed in experiments and estimated from dynamic swelling. The 1-D models proposed herein are computationally effective and easily implementable for BMS for efficient control of battery cells and packs. These novel models are useful for electrified vehicles where unexpected exposure of the battery pack to severe environments can have dire consequences. For example, fusing information from voltage, swelling, and force measurement enables BMS to estimate SOC more accurately and robustly, similar to Ref. [56]. The combination of the proposed models with electric-circuit models and thermal swelling models can predict the stresses due to Li-ion intercalation and that due to thermal swelling, and thereby facilitate more enhanced power strategies in BMS, similar to Ref. [79]. The framework can provide potential utility for the SOC or SOH estimation as a standalone algorithm or in hybrid forms with existing algorithms [76,83,84] because swelling and its induced force are related to battery states and degradation. This work opens the door for an enhanced battery management system through the incorporation of mechanical measurements.
- A 3-D numerical and phenomenological swelling model was developed. This model is cable of describing the swelling shape on the battery surface for all SOC regions from two different sources at an unconstrained condition and a constrained condition. This model incorporated the nonlinear equivalent modulus of elasticity over SOC to electrodes to account for the phase transition and the interlayer spacing of atoms in the active material particles which make up the electrodes is affected by Li-ion concentration. This

model also incorporated nonuniform temperature distribution of the jellyroll and the creation of gaps and voids between electrodes to account for thermal swelling. This model also took into account the anisotropic heat conduction and temperature dependency of the coefficient of thermal expansion of the jellyroll. The coupled thermal-structural analysis accurately reproduced two experimental swelling at different C-rates, indicating that our approach is reasonable and the estimated properties are accurate. The proposed 3-D model also enables the creation of parametric reduced-order models for the fatigue life prediction or optimization of the HEVs [92], and thereby reduces the calculation time. The swelling shape can be extracted from the proposed model and compared to measured swelling data for enhanced power management or to facilitate SOC estimation and diagnostic algorithms because the swelling shape due to Li-ion intercalation is constant over SOC [42]. Ultimately, implementing in-situ monitoring of strain inside individual Li-ion battery cells with the proposed model in BMS holds great promise in improving the safety of a pack by allowing earlier detection of the onset of fracture, which can lead to performance degradation of the cell.

- A fully coupled phenomenological multi-physics model of Li-ion cell was developed for control-oriented purposes. The model can predict three key features of battery cell at the pack condition: electric behaviors including the potential and SOC, thermal behaviors including surface and core temperatures, and structural behaviors such as swelling and force. The electric and thermal behaviors were estimated from a coupled electro-thermal model, which is comprised of two-state thermal model and a three-state electrical model per battery cell. The swelling from two sources were estimated from the 1-D Li-ion intercalation lookup table, swelling versus SOC, and the 1-D thermal swelling model developed in Chapter III. The force model developed in Chapter IV was modified to account for the distance variation of two endplates upon ambient temperature, the softening effect of stiffness over temperature, and the temperature dependency of the coefficient of thermal expansion. Intensive experimental verification confirmed that the model accurately predicts complex behaviors of Li-ion cells at the wide operational range of preload and ambient temperature. The 1-D high fidelity multi-physics model is useful for more accurate and robust SOC estimation considering the complex dynamic behaviors behind the battery cell as suggested in [120].

7.2. Future Research

Next, some suggestions for future research are proposed based on the work reported in this dissertation.

First, the multi-physic model used lookup table to estimate swelling induced from Li-ion intercalation assuming that the hysteresis during Li-ion intercalation and deintercalation was negligible. However, a hysteresis of the graphene interlayer spacing exists during lithiation and delithiation. It can therefore be inferred that a model for Li-ion intercalation based on first principles which is capable to predict the hysteresis and the dynamics of Li-ion intercalation swelling, can enhance the accuracy of the predictions of current models.

Second, experimental verification for the 3-D Li-ion intercalation swelling model was only carried out at an unconstrained condition. To enhance the reliability of the proposed 3-D model for the use in battery management strategies, experimental efforts should be concentrated on the validation of the 3-D Li-ion intercalation swelling model at a constrained condition, i.e. pack condition, with novel and high accuracy swelling sensing technologies.

Third, innovative power and thermal management strategies with a fully coupled multi-physics model should be developed based on fusing information from voltage, temperature, and/or force measurements. These efforts include calculating the SOC with enhanced accuracy, detecting SOC imbalances inside the cells of the battery pack, and improving prognostic algorithms for estimating the remaining battery lifetime through experimental and numerical approaches.

BIBLIOGRAPHY

[1] T. M. Bandhauer, S. Garimella, and T. F. Fuller, Journal of the Electrochemical Society. 158 (3) (2011) R1-R25.

[2] X. Hu, S. Lin, S. Stanton, and W. Lian, IEEE Transactions on Industry Applications. 47 (4) (2011) 1692-1699.

[3] J. Shim, R. Kostecki, T. Richardson, X. Song, and K. A. Striebel, Journal of Power Sources. 112 (2002) 222-230.

[4] J. B. Siegel, A.G. Stefanopoulou, P. Hagans, Y. Ding, and D. Gorsich, Journal of the Electrochemical Society. 160 (8) (2013) A1031-1038A.

[5] X. Wang, Y. Sone, G. Segami, H. Naito, C. Yamada, and K. Kibe, Journal of the Electrochemical Society. 154 (1) (2007) A14-A21.

[6] N. Zhang, and H. Tang, Journal of Power Sources. 218 (2012) 52-55.

[7] D. Liu, Y. Wang, Y. Xie, L. He, J. Chen, K. Wu, R. Xu, and Y. Gao, Journal of Power Sources. 232 (2013) 29-33.

[8] F. Kaasik, T. Tamm, M. M. Hantel, E. Perre, A. Aabloo, E. Lust, M. Z. Bazant, and V. Presser, Electrochemistry Communications. 34 (2013) 196-199.

[9] J. Christensen, Journal of the Electrochemical Society. 157 (2010) A366-A380.

[10] J. Christensen, and J. Newman, Journal of Solid State Electrochemistry. 10 (5) (2006) 293-319.

[11] J. Christensen, and J. Newman, Journal of the Electrochemical Society. 153 (2006) A1019-A1030.

[12] J. Cannarella, and C. B. Arnold, Journal of Power Sources. 245 (2014) 745-751.

[13] I. Bloom, A. N. Jansen, D. P. Abraham, J. Knuth, S. A. Jones, V. S. Battaglia, and G. L. Henriksen, Journal of Power Sources. 139 (2005) 295-303.

[14] D. Shi, X. Xiao, X. Huang, and H. Kiaa, Journal of Power Sources. 196 (2011) 8129-8139.

[15] A. Sheidaei, X. Xiao, X. Huang, and J. Hitt, Journal of Power Sources. 196 (2011) 8728-8734.

[16] K. Nansaka, and Y. Yamauchi, United States Patent US 8216715 (2012).

[17] T. Ohzuku, Y. Iwakoshi, and K. Sawai, Journal of the Electrochemical Society. 140 (9) (1993) 2490-2498.

[18] J. H. Lee, H. M. Lee, and S. Ahn, Journal of Power Sources. 119-121 (2003) 833-837.

[19] Y. Koyama, I. Tanaka, H. Adachi, Y. Makimura, and T. Ohzuku, Journal of Power Sources. 119-121 (2003) 644-648.

[20] R. Yazami, and Y. Reynier, Journal of Power Sources. 153 (2006) 312-318.

[21] Y. Kim, J. B. Siegel, and A. G. Stefanopoulou, 2013 American Control Conference. Washington, USA (2013).

[22] H. M. Dahn, A. J. Smith, J. C. Burns, D. A. Stevens, and J. R. Dahn, Journal of the Electrochemical Society. 159 (2012) A1405-A1409.

[23] I. Bloom, L. K. Walker, J. K. Basco, D. P. Abraham, J. P. Christophersen, and C. D. Ho, Journal of Power Sources. 195 (2010) 877-882.

[24] K. G. Gallagher, D. W. Dees, A. N. Jansen, D. P. Abraham, and S. H. Kang, Journal of the Electrochemical Society. 159 (2012) A2029-A2037.

[25] X. Wang, Y. Sone, and S. Kuwajima, Journal of the Electrochemical Society. 151 (2) (2004) A273-A280.

[26] M. Bryner, Chemical Engineering Progress. 109 (10) (2013) 36-39.

[27] A. N. Jansen, Chemical Engineering Progress. 109 (10) (2013) 57-64.

[28] B. Scrosati, and J. Garche, Journal of Power Sources. 195 (2010) 2419-2430.

[29] L. B. Lave, and H. L. MacLean, Transportation Research Part D. 7 (2) (2002) 155-162.

[30] F. V. Conte, Elektrotechnik & Informationstechnik. 123 (10) (2006) 424-431.

[31] M.-S. Wu, K. H. Liu, Y.-Y. Wang, and C.-C. Wan, Journal of Power Sources. 109 (2002) 160-166.

[32] S.-C. Chen, Y.-Y. Wang, and C.-C. Wan, Journal of the Electrochemical Society. 153 (4) (2006) A637-A648.

[33] S. Peck, T. Olszanski, S. Zanardelli, and M. Pierce, SAE Int. J. Passeng. Cars - Electron. Electr. Syst. 5 (1) (2012) 154-163.

[34] V. Srinivasan, and C. Y. Wang, Journal of the Electrochemical Society. 150 (1) (2003) A98-A106

[35] Y. Chen, and J. W. Evans. Journal of the Electrochemical Society. 143 (9) (1996) 2708-2712.

[36] S. A. Khateeb, S. Amiruddin, M. Farid, J. R. Selman, S. Al-Hallaj, Journal of Power Sources. 142 (2005) 345-353.

[37] A. Santucci, A. Sorniotti, and C. Lekakou, Journal of Power Sources. 258 (2014) 395-407.

[38] K. Onda, T. Ohshima, M. Nakayama, K. Fukuda, and T. Araki, Journal of Power Sources. 158 (2006) 535-542.

[39] C. Bindra, V. A. Nalimova, D. E. Sklovsky, W. A. Kamitakahara, and J. E. Fischer, Physical Review B. 57 (9) (1998) 5182-5190.

[40] K. Mukai, Y. Kishida, H. Nozaki, and K. Dohmae, Journal of Power Sources. 224 (2013) 230-235.

[41] S. Komaba, A. Ogata, T. shimizu, and S. Ikemoto, Solid State Ionics. 179 (2008) 1783-1787.

[42] K.-Y. Oh, J. B. Siegel, L. Secondo, S. U. Kim, N. A. Samad, J. Qin, D. Anderson, K. Garikipati, A. Knobloch, B. I. Epureanu, C. W. Monroe, and A. G. Stefanopoulou, Journal of Power Sources. 267 (2014) 197-202.

[43] X. Lin, H. E. Perez, J. B. Siegel, A. G. Stefanopoulou, Y. Li, R. D. Anderson, Y. Ding, and M. P. Castanier, IEEE Transactions on Control System Technology. 21 (5) 2013 1745-1755.

[44] X. Lin, H. E. Perez, S. Mohan, J. B. Siegel, A. G. Stefanopoulou, and Y. Ding, and M. P. Castanier, Journal of Power Sources. 257 (2014) 1-11.

[45] D. Bernardi, E. Pawlikowski, and J. Newman, Journal of the Electrochemical Society. 132 (1) (1985) 5-12.

[46] S. Chen, C. Wan, and Y. Wang, Journal of Power Sources. 140 (2005) 111-24.

[47] Y. Qi, H. Guo, L. G. Hector, Jr., and A. Timmons, Journal of the Electrochemical Society. 157 (5) (2010) A558-A566.

[48] K. Onda, H. Kameyama, T. Hanamoto, and K. Ito, Journal of the Electrochemical Society. 150 (3) (2003) A285-A291.

[49] P. Arora and Z. (J.) Zhang. Chem. Rev. 104 (2004) 4419-4462.

[50] D. J. Lacks, and G. C. Rutledge. J. Phys. Chem. 98 (1994) 1222-1231.

[51] J. R. Dahn, Physical Review B. 44 (17) (1991) 9170-9177.

[52] J. Sugiyama, T. Tamura, and H. Yamauchi, Journal of Physics: Condensed Matter. 7 (1995) 9755-9764.

[53] V. A. Sethuraman, M. J. Chon, M. Shimshak, N. Van Windle, and P. R. Fuduru, Electrochemistry Communications. 12 (2010) 1614-1617.

[54] Polymer data handbook, Oxford University Press, 1999.

[55] N. Lagakos, J. Jarzynski, J. H. Cole, and J. A. Bucaro. Journal of Applied Physics. 59 (1986) 4017-4031.

[56] S. Mohan, Y. Kim, J. B. Siegel, N. A. Samad, and A. G. Stefanopoulou, Journal of the Electrochemical Society. 161 (14) (2014) A2222-A2231.

[57] B. Sood, M. Osterman, and M. Pecht, 2013 IEEE Symposium on Product Compliance Engineering. Austin, USA (2013).

[58] H. L. Tuller, J. Schoonman, and I. Riess, Kluwer Academic Publishers, 2000.

[59] F. Tietz, Ionics. 5 (1999) 129-139.

[60] R. E. Garcia, Y. M. Chiang, W. C. Carter, P. Limthongkul, and C. M, Bishop, Journal of the Electrochemical Society. 152 (2005) A255–A263.

[61] N. A. Samad, J. B. Siegel, and A. G. Stefanopoulou, Proceedings of the ASME 2014 Dynamic Systems and Control Conference. San Antonio, USA (2014).

[62] Y. Kim, S. Mohan, J. B. Siegel, A. G. Stefanopoulou, and Y. Ding, IEEE transactions on control systems technology 22 (6) (2014) 2277- 2286.

[63] H. Khasawneh, J. Neal, M. Canova, Y. Guezennec, R. Wayne, J. Taylor, M. Smalc, and J. Norley, IMECE2011 Denver, USA (2011) 421-428.

[64] S.C. Chen, C.C. Wan, and Y. Y. Wang, JPS 140 (1) (2005) 111-124.

[65] R. Beger, H. Wenzl, H.P. Beck, M. Jiang, D. Ohms, G. Schaedlich, EVS24, Stavanger, Norway (2009) 342-351.

[66] G. Ning, B. Haran, and B. N. Popov, Journal of Power Sources. 117 (2003) 160-169.

[67] A. Knobloch, J. Siegel, A. Stefanopoulou, C. Monroe, B. Epureanu, K. Garipkipati, and D. Anderson, Proceeding of the Advanced Automotive Batteries Conference 2014. Atlanta, USA (2014).

[68] L. Lu, X. Han, J. Li, J. Hua, and M. Ouyang, Journal of Power Sources. 226 (2013) 272-288.

[69] M. Chen, and G. A. Rinc´on-Mora, IEEE Transactions on Energy Conversion. 21 (2) (2006) 504-511.

[70] Nassim, Jason B. Siegel, and Anna G. Stefanopoulou, Proceedings of the ASME 2014 Dynamic Systems and Control Conference. San Antonio, USA (2014).

[71] M. Park, X. Zhang, M. Chung, G. B. Lessa, and A. M. Sastry, Journal of Power Sources. 195 (2010) 7904-7929.

[72] V. A. Sethuraman, M. J. Chon, M. Shimshak, V. Srinivasana, and P. R. Guduru, Journal of Power Sources 195 (2010) 5062-5066.

[73] V. A. Sethuraman, N. V. Winkle, D.P. Abraham, A.F. Bower, and P.R. Guduru, Journal of Power Sources 206 (2012) 334-342.

[74] A. Mukhopadhyay, A. Tokranov, X. Xiaoc, and B. W. Sheldon, Electrochimica Acta. 66 (2012) 28-37.

[75] C. Peabody, and C. B. Arnold, Journal of Power Sources. 196 (2011) 8147-8153.

[76] J. Cannarella, and C. B. Arnold, Journal of Power Sources. 269 (2014) 7-14.

[77] Y. Qi and S. J. Harris, Journal of the Electrochemical Society. 157 (6) (2010) A741-A747.

[78] K.-Y. Oh, B. I. Epureanu, Journal of Power Source. 303 (2016) 86-96.

[79] Y. Kim, S. Mohan, N. A. Samad, J. B. Siegel, and A. G. Stefanopoulou, 2014 American Control Conference, USA (2014)

[80] V. A. Sethuraman, L. J. Hardwick, V. Srinivasan, R. Kostecki, Journal of Power Sources. 195 (2010) 3655-3660.

[81] J. Cannarella, X. Liu, C. Z. Leng, P. D. Sinko, G. Y. Gor, and C. B. Arnold, Journal of the Electrochemical Society. 161 (11) (2014) F3117-F3122.

[82] K. D'Souza, B. I. Epureanu, Journal of Sound and Vibration. 329 (2010) 2463-2476.

[83] G. K. Prasad, and C. D. Rahn, Journal of Power Sources. 232 (2013) 79-85.

[84] J. Schmalstieg, S. Käbitz, M. Ecker, and D. U. Sauer, Journal of Power Sources. 257 (2014) 325-334.

[85] S. U. Kim, P. Albertus, D. Cook, C. W. Monroe, and J. Christensen, Journal of Power Sources. 268 (2014) 625-633.

[86] F. Yang, Journal of Power Sources. 241 (2014) 146-149.

[87] X. Xiao, W. Wu, and X. Huang, Journal of Power Sources. 195 (2010) 7649-7660.

[88] M. Liu, Journal of Power Sources. 275 (2015) 760-768.

[89] I. C. Halalay, M. J. Lukitsch, M. P. Balogh, and C. A. Wong, Journal of Power Sources. 238 (2013) 469-477.

[90] X. Zhang, W. Shyy, and A. M. Sastry, Journal of the Electrochemical Society. 154 (10) A910-A916.

[91] K. R. Kganyago, and P. E. Ngoepe, Physical Review B 68 (2003) 205111.

[92] S.-K. Hong, B. I. Epureanu, M. P. Castanier, Journal of Power Sources. 261 (2014) 101-111.

[93] S. Campanari, G. Manzolini, and F. G. De la Iglesia, Journal of Power Sources. 186 (2) (2009) 464-477.

[94] P. H. Andersen, J. A. Mathews, and M. Rask, Energy Policy. 37 (7) (2009) 2481-2486.

[95] J. Wang, J. Purewal, P. Liu, J. Hicks-Garner, S. Soukazian, E. Sherman, A. Sorenson, L. Vu, H. Tataria, M. W. Verbrugge, Journal of Power Sources. 269 (2014) 937-948.

[96] D. Andrea, Battery Management Systems for Large Lithium-ion Battery Packs, Artech House, 2010.

[97] H. Teng, Y. Ma, K. Yeow, M. Thelliez, SAE International Journal of Passenger Cars - Mechanical Systems. 4 (3) (2011) 1343–1357.

[98] F. He, D. Ewing, J. Finn, J. Wagner, L. Ma, SAE International Journal of Alternative Powertrains. 2 (1) (2013) 174–203.

[99] Z. Rao, S. Wang, Renewable and Sustainable Energy Reviews. 15 (2011) 4554-4571.

[100] H. Park, Journal of Power Sources. 239 (2013) 30-36.

[101] Y. Qi, L. G. Hector, C. James, and K. J. Kim, Journal of the Electrochemical Society. 161 (11) (2014) F3010-F3018.

[102] D. Shia, X. Xiao, X. Huang, and Hamid Kia, Journal of Power Sources. 196 (2011) 8129-8139.

[103] J. W. Rose, J. R. Cooper, and H. M. Spiers, Technical Data on Fuel, Wiley, New York, 1977.

[104] W.C. Reynolds, Thermodynamic Properties in SI: Graphs, Tables, and Computational Equations for Forty Substances, Dept. Of Mechanical Engineering, Stanford University, Stanford, CA, 1979.

[105] MatWeb: http://www.matweb.com/

[106] C. L. Choy, F. C. Chen, and E. L. Ong, Polymer. 20 (1979) 1191-1198.

[107] S. J. Drake, D. A. Wetz, J. K. Ostanek, S. P. Miller, J. M. Heinzel, and A. Jain, Journal of Power Sources. 252 (2014) 298-304.

[108] V. Vishwakarma, and A. Jain, Journal of Power Sources. 272 (2014) 378-385.

[109] J. Christensen, P. Albertus, D. Cook, in: The Electrochemical Society Meeting 1622, 2011. Montreal, QC, Canada.

[110] V. Ramadesigan, P. W. C. Northrop, S. De, S. Santhanagopalan, R. D. Braatz, and V. R. Subramanian. Journal of the Electrochemical Society. 159 (3) (2012) R31-R45.

[111] M. Doyle, T. Fuller, and J. Newman, Journal of the Electrochemical Society. 140 (6) (1993) 1526-1533.

[112] K. Murashko, J. Pyrhonen, and L. Laurila, IEEE Transactions on Energy Conversion. 28 (2) (2013) 335-343.

[113] M. Einhorn, F. Conte, C. Kral, and J. Fleig, IEEE Transactions on Power Electronics. 28 (3) (2013) 1429-1437.

[114] Y. Hu, S. Yurkovich, Y. Guezennec, and B. Yurkovich, Journal of Power Souces. 196 (1) (2011) 449-457.

[115] F. He, H. Wang, and L. Ma, International Journal of Heat and Mass Transfer. 91 (2015) 630-639.

[116] G.-H. Kim, K. Smith, K.-J. Lee, S. Santhanagopalan, and A. Pesaran, Journal of Power Souces. 158 (8) (2011) A955-A969.

[117] Y. Xie, J. Li, and C. Yuan, Journal of Power Sources. 248 (2014) 172-179.

[118] S. Jung, D. Kang, Journal of Power Sources. 248 (2014) 498-509.

[119] N. A. Samad, B. Wang, J. B. Siegel, and A. G. Stefanopoulou, Journal of Dynamic Systems, Measurement, and Controls, under revision.

[120] Y. Kim, N. A. Samad, K.-Y. Oh, J. B. Siegel, B. Epureanu, A. G. Stefanopoulou, ACC 2016.